Seismic Thermometry of the North Pacific and Equatorial Indian Oceans

Thesis by
Shirui Peng

In Partial Fulfillment of the Requirements for the
Degree of
Doctor of Philosophy

Caltech

CALIFORNIA INSTITUTE OF TECHNOLOGY
Pasadena, California

2024
Defended May 21, 2024

© 2024

Shirui Peng
ORCID: 0000-0002-4616-4604

ACKNOWLEDGEMENTS

First and foremost, I would like to express my sincere gratitude to my Ph.D. advisor Jörn Callies. His guidance has deeply inspired my philosophy of doing research beyond scientific knowledge and techniques. Jörn is also more than a research advisor. He has offered tremendous support and encouragement during my life at Caltech, and I have always enjoyed our professional and casual conversations.

I would like to thank my committee members: Andrew F. Thompson, Konstantin Batygin, Tim Colonius, Zhongwen Zhan, and Michael J. Mcphaden. Andy provided me with considerably useful advice for designing my academic path and my future career. Konstantin helped me a lot as my advisor for one of my first-year projects, and his outstanding insights on science, music, and life continue to inspire me today. Tim and Zhongwen are really knowledgeable and passionate. I greatly benefit from discussions with them. Mike also gave me invaluable help and encouragement as my committee member and collaborator. I would also like to thank Wenbo Wu and Motoki Nagura as my collaborators. Without you, I could not have explored such interesting problems. The work presented in this thesis was supported by the Resnick Sustainability Institute and the National Science Foundation under Grant OCE-2023161.

I would especially like to thank the GPS division for the opportunities to pursue my Ph.D. at Caltech before, during, and after the pandemic. I have found a sense of belonging in this remarkable community thanks to the following colleagues and friends:

GPS Staff: Nora Oshima, Julie Lee, Leticia Calderon, Bronagh Glaser, Julia Zuckerman, Mark Garcia, Grecia Ames.

Faculty: Paul Wennberg, Christian Frankenberg, Tapio Schneider, Jess F. Adkins, Heather A. Knutson, Andrew P. Ingersoll.

The Fall 2019 student cohorts: Jordan Benjamin, Dave Bonan, Costa Christopoulos, Mudit Murarka, Henry Peterson, Polina Khapikova, Ryan Ward, James W. Atterholt, Holly Barnhart, Surjyendu Bhattacharjee, Maria Camarca, Ruolin Deng, Marguerite Epstein-Martin, Hannah Dion-Kirschner, Michael Greklek-McKeon, Yuan Kai Liu, Justin A. Nghiem, Rebecca L. Wipfler, Casey Yamamoto, Yan Yang.

Callies Lab: Albion Lawrence, Jack Skinner, Shane Zhang, Xihan Zhang, Henry Peterson, Scott Conn, Yue Bai, Haakon Ludvig Langeland Ervik, Shriya Fruitwala,

ABSTRACT

The ocean absorbs the majority of excess heat in the climate system. Ocean mixing is also critical in setting Earth's thermal inertia. Over the course of the past few decades, conventional observations like Argo floats have drastically improved the coverage of the global ocean. However, their temporal and spatial resolutions are still limited. Resolving trends and patterns of temperature variations in the ocean under climate change remains a challenging sampling problem. This dissertation seeks to reduce such sampling errors by developing seismic thermometry. It is an acoustic method that measures large-scale ocean temperature changes using sound waves generated by repeating earthquakes. The chapters in this thesis attempt to combine physical understanding with statistical analysis to improve and implement seismic thermometry in several ways. First, acoustic waves generated by earthquakes along the Japan Trench and received at Wake Island are used to constrain temperature variation in the Kuroshio Extension region. An inversion that combines these measurements for the time and azimuth dependence of the range-averaged deep temperatures reveals lateral and temporal variations due to Kuroshio Extension meanders, mesoscale eddies, and decadal water mass rearrangements. Second, a comprehensive covariance structure is proposed to represent variabilities due to stochastic mesoscale, regional trend, and large-scale seasonality. It demonstrates statistical consistency between conventional float data and seismic measurements, and shows quantitatively that seismic thermometry reduces basin-scale temperature uncertainty when combined with conventional measurements. Finally, seismic data are compared with ocean models in the equatorial Indian Ocean to study the vertical structure of biweekly Yanai waves. The comparison indicates qualitative agreements in biweekly variations, and regression analysis confirms their origin as west-propagating Yanai waves. Yet quantitative differences in the biweekly variance magnitude demand further calibrations in both models and the seismic inversion.

PUBLISHED CONTENT AND CONTRIBUTIONS

Peng, S., J. Callies, W. Wu, and Z. Zhan (2024). "Seismic Ocean Thermometry of the Kuroshio Extension Region". In: *Journal of Geophysical Research: Oceans* 129.2, e2023JC020636. DOI: 10.1029/2023JC020636.
S.P participated in the conception of the project, processed and analyzed the seismic data, prepared the first draft, and participated in the writing of the manuscript.

TABLE OF CONTENTS

LIST OF ILLUSTRATIONS

LIST OF TABLES

C h a p t e r   1

INTRODUCTION

The ocean, with its vast heat capacity, is the principal reservoir of excess energy on Earth caused by anthropogenic climate change (Levitus et al., 2000). Monitoring climate change more accurately urges complementary ways of measuring temperatures in the deep ocean (von Schuckmann et al., 2016). Seismic thermometry provides an opportunity to support a comprehensive observing system of deep-ocean temperature. Data gathered from this system can help mitigate sampling challenges faced by conventional in situ techniques. Insights on ocean dynamics can arise from calibrating dynamical models with the seismic data. By combining seismic with conventional data, a long-term large-scale ocean temperature sampling framework can obtain better resolved ocean warming patterns that have local impacts.

Ocean warming and its associated heat redistribution directly affect regional hydrological cycle and weather system, and cause more severe marine species and ecosystem damage. Precise monitoring of ocean temperature changes is essential for better quantifying its warming rate, distribution, and impacts in current and future scenarios. Seismic thermometry aims to improve deep-ocean temperature measurements using sound waves generated by natural earthquakes. The development of seismic thermometry is promising not only because it complements conventional data for deep-ocean thermometry, but also because it combines natural acoustic sources and existing seismological, oceanic, and more general infrastructures in a highly resource-efficient way. This method may initiate the next-level ocean warming observation network in the near future.

Over the past few decades, a multiplatform system has been developed to measure temperatures in mid-depth and deep oceans. Since the twentieth century, ships have been using onboard equipment to sample full-depth temperatures systematically in programs like the World Ocean Circulation Experiment (WOCE) and GO-SHIP (e.g., Purkey and Johnson, 2010; Desbruyères et al., 2017). These measurements cover specific sections across the global ocean in a decadal or shorter cycle. Starting in early 2000, the Argo program has been collecting ocean temperatures sampled from autonomous floats (e.g., Abraham et al., 2013; Riser et al., 2016). Covering the global ocean with nearly 4000 of them, these floats measure ocean temperature

every 10 d over the upper 2000 m depth, a few of them currently reach the bottom of the ocean between 4000 to 6000 m depth. These in situ techniques have contributed in a major way to our understanding of temperature changes in the deep ocean. For example, Argo data have helped constrain a 95% credible interval for the 2007–2021 globally integrated heat content to be 4.66 to 16.03 ZJ yr^{-1} over the upper 2000 m depth (Baugh and McKinnon, 2022). The greatest challenge to depending only on these measurements is perhaps their sparse resolutions in both space and time compared with intrinsic ocean variabilities. As an alternative, acoustic ocean thermometry with controlled sound sources measures path-integrated temperatures that accurately average out smaller variations along the way (Munk and Wunsch, 1979; The ATOC Consortium, 1998). However, it is neither well-developed nor combined systematically with in situ observations due to concerns about its potential damage to the marine ecosystem.

Seismic thermometry complements in situ measurements with an acoustic method that uses sound waves generated by natural repeating earthquakes (Wu et al., 2020; Callies et al., 2023; Wu et al., 2023). Earthquakes excite elastic *P/S* waves that can be converted to acoustic *T* waves at the ocean-land interface (Okal, 2008). These *T* waves propagate over long distances through the ocean and generate continuous wave packet signals in hydrophones or near-shore seismic stations as reconverted elastic waves. And their travel times are sensitive to deep ocean temperatures. Importantly, changes in ocean temperature induce changes in *T* wave travel time between repeating earthquakes that share the same source location. Because sound waves travel faster in warmer water, they arrive slightly earlier if warming over a day or longer has occurred along their path. The vertical structure of this sensitivity depends on local stratification and the wave frequency, which generally maximizes around 1500 m depth with a moderate amount below 2000 m. Therefore, travel time changes between repeaters serve as indirect measurements of range-averaged temperature anomalies.

The application of seismic thermometry in the East Indian Ocean has provided valuable temperature measurements that captured prominent seasonal cycles and long-term trends, qualitatively consistent with those derived from conventional data (Wu et al., 2020). Subsurface hydrophones have allowed the use of smaller earthquakes, further increasing time resolution to resolve subseasonal variations that could arise from equatorial waves (Wu et al., 2023). And Callies et al. (2023) has taken advantage of the frequency-dependent sensitivity of *T* waves to infer vertical

structures of ocean temperature changes. Nevertheless, several questions remain for a broader and more reliable coverage of seismic thermometry in the global ocean. The development requires the study of its applicability in other regions, as well as quantitative consistency with the conventional data. This is related to the possibility of combined measurements with seismic and conventional data. And those prominent variabilities in the seismic data also call for detailed scientific studies on their oceanic origins.

This thesis seeks to address relevant focused questions and ease the improvement of deep-ocean temperature measurements with seismic thermometry. Chapter 2 develops the method for the Kuroshio Extension region. This region is characterized by energetic mesoscale eddies and large decadal variability (e.g. Mizuno and White, 1983; Qiu and Chen, 2005), which presents a challenging sampling problem for conventional ocean observations. The seismic measurements are obtained from a hydrophone station off and a seismic station on Wake Island, with the seismic station's digital record reaching back to 1997. This chapter introduces an inversion that combines these measurements for the time and azimuth dependence of the range-averaged deep temperatures, revealing lateral and temporal variations due to Kuroshio Extension meanders, mesoscale eddies, and decadal water mass displacements.

Although Chapter 2 shows qualitative agreements between the seismic data and independent observations like Argo, Chapter 3 demonstrates statistical consistency between the seismic and Argo data and reduced uncertainty in basin-scale temperature measurements with the combined data. This chapter establishes a comprehensive covariance structure to represent correlations among observations from ships, Argo floats, and seismic thermometry. These correlations reflect intrinsic variations in the Kuroshio Extension region, qualitatively revealed by the data analyzed in Chapter 2. An updated inversion is then described that can estimate basin-scale temperature changes based on the data and prescribed covariances. This is, to my knowledge, the first systematic combination of in situ measurements of ocean temperature with an acoustic method, here the seismic thermometry.

Finally, Chapter 4 is devoted to the physical analysis of wave dynamics revealed by seismic data from the equatorial Indian Ocean. In this region, near-surface measurements of current velocity suggest that wind forcing excites waves in the biweekly band (Pujiana and McPhaden, 2021). However, the characteristics of these waves in the deep ocean are poorly constrained, and it is unclear how well models capture

the deep variability. This chapter uses T waves to infer temperature variations in the deep East Indian Ocean. These T waves are generated by earthquakes off Sumatra and received by a hydrophone station off Diego Garcia. The comparison between T wave data and model outputs shows good consistency in biweekly variations. Regression analysis indicates that these variations originate from west-propagating Yanai waves. However, there are quantitative differences in the comparison. Similar discrepancy appears in the comparison between the models and deep-mooring measurements. Investigations on using seismic thermometry to improve ocean models as intrinsic calibration, or vice versa, are left for future work.

Chapter 2

SEISMIC OCEAN THERMOMETRY OF THE KUROSHIO EXTENSION REGION

2.1 Abstract

Seismic ocean thermometry uses sound waves generated by repeating earthquakes to measure temperature change in the deep ocean. In this study, waves generated by earthquakes along the Japan Trench and received at Wake Island are used to constrain temperature variations in the Kuroshio Extension region. This region is characterized by energetic mesoscale eddies and large decadal variability, posing a challenging sampling problem for conventional ocean observations. The seismic measurements are obtained from a hydrophone station off and a seismic station on Wake Island, with the seismic station's digital record reaching back to 1997. These measurements are combined in an inversion for the time and azimuth dependence of the range-averaged deep temperatures, revealing lateral and temporal variations due to Kuroshio Extension meanders, mesoscale eddies, and decadal water mass displacements. These results highlight the potential of seismic ocean thermometry for better constraining the variability and trends in deep-ocean temperatures. By overcoming the aliasing problem of point measurements, these measurements complement existing ship- and float-based hydrographic measurements.

2.2 Introduction

Heat transfer from the surface to the deep ocean plays an important role in setting the rate at which the Earth warms in response to anthropogenic forcing (e.g., Hansen et al., 1985; Held et al., 2010). Because the Earth's energy imbalance is not well-constrained by radiation measurements at the top of the atmosphere, quantifying this heat transfer requires measurements of both the surface and deep ocean (e.g., Palmer et al., 2011; Trenberth et al., 2014; von Schuckmann et al., 2016; Meyssignac et al., 2019). While the Argo program has provided near-global in situ data from the top 2000 m of the water column since the mid-2000s (e.g., Riser et al., 2016), and repeat hydrography has provided full-depth measurements along a set of transects since the 1990s (e.g., Talley et al., 2016), the spatial and temporal sampling of the existing observing system is too sparse to resolve the mesoscale eddy field, and the associated variance must be treated effectively as a measurement error. This limits our ability
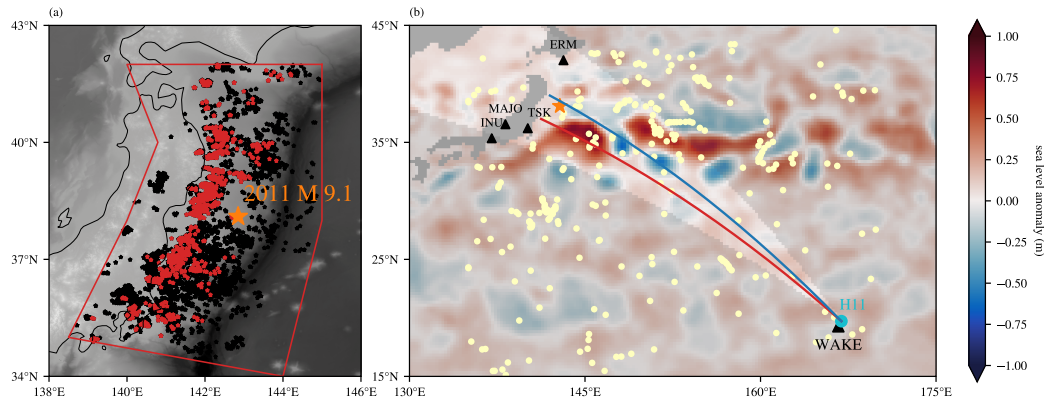
Figure 2.1: Study area in the Northeast Pacifc. (a) Bathymetry of the Japan Trench and earthquake locations. The red polygon shows the area used in the earthquake search. The black stars are the 7813 ISC catalog earthquakes detected by *P*-wave cross-correlation with a threshold of 0.9 in 1997 to 2021, and the red stars are the repeaters usable for seismic ocean thermometry. The orange star indicates the 2011 M 9.1 Tōhoku earthquake. (b) Sea level anomaly map of the region on 2012-01-01, with the locations of the hydrophone (cyan circle) and seismic stations (black triangles) also shown. The fan that is not grayed out highlights the azimuth range sampled by the *T*-wave paths used in this study. The red and blue curves show great circle paths to H11 at azimuths 315.0° and 317.5° relative to due north.

to constrain decadal-scale variability and long-term warming, especially in western boundary current regions and the Southern Ocean, where mesoscale eddies are vigorous and associated with mid-depth temperature anomalies of order 1 K.

To complement existing in situ data, Wu et al. (2020), Callies et al. (2023), and Wu et al. (2023) used sound waves generated by natural earthquakes to constrain temperature fluctuations averaged over travel paths that are a few thousand kilometers long, expanding on previous acoustic tomography that used controlled sources (Munk and Wunsch, 1979; Dushaw et al., 2009). These applications of seismic ocean thermometry to the East Indian Ocean revealed qualitative consistency with previous estimates and offered improved constraints on the large-scale temperature variations because local fluctuations are intrinsically averaged along the waves' path. In this paper, we make use of sound waves that are seismically generated off Japan and received at Wake Island, thus sampling the Kuroshio Extension region (cf., Lebedev et al., 2003). We consider a whole set of travel paths from earthquakes along the Japan Trench to Wake Island and invert for large-scale temperature anomaly as a function of the azimuth at which the travel path arrives at Wake Island (Fig. 2.1). Our approach allows for improved constraints of the large-scale temperature variations

in the region reaching back to the 1990s and promises to further insight into the dynamics of the region as well as its response to climate forcing.

The Kuroshio Current separates from the coast around 35°N to form the Kuroshio Extension, a narrow jet associated with a sharp surface and subsurface temperature front marking the boundary between warm subtropical and cold subpolar waters. The current meanders and produces energetic pinched-off mesoscale eddies that evolve on a time scale of a few tens of days (e.g., Mizuno and White, 1983; Yasuda et al., 1992; Lebedev et al., 2003; Nonaka et al., 2006; Na et al., 2016), and the current switches between straight and meandering paths on a decadal time scale (e.g., Qiu and Chen, 2005). Because of the sharp temperature contrast across the Kuroshio Extension, these dynamics produce large-amplitude temperature variations at a range of length and time scales that are difficult to capture with in situ observations. It is crucial to monitor these transient displacements of water masses in order to distinguish them from climate signals consisting of material warming as well as secular displacements arising from trends in the circulation.

Western boundary current regions like the Kuroshio Extension region have been suggested to be warming more rapidly than the rest of the global ocean. Wu et al. (2012) estimated from temperature reconstructions that the surface temperature in boundary current regions increased at two to three times the rate of the global mean over the course of the 20th century. Sugimoto et al. (2017) used in situ hydrographic data to estimate the warming of subtropical mode waters in both the North Pacific and North Atlantic, finding warming rates that were twice as large as at the surface. This accelerated warming of western boundary current regions may be due to a poleward shift or intensification of these currents (Wu et al., 2012; Saba et al., 2016), although the limited record of transport observations for the Gulf Stream since the 1990s shows no evidence of such a trend (Rossby et al., 2019). Considerable uncertainty therefore remains in our understanding of how western boundary current regions respond to the climate forcing, including how deep the warming and suggested transport trends reach.

Seismic ocean thermometry can contribute to better constraints of the large-scale deep-ocean temperature changes of the Kuroshio Extension region. Unlike traditional acoustic tomography methods that require controlled sound sources, this method uses repeating earthquakes as natural sources of sound waves, so-called T waves (Wu et al., 2020). Recent work has explored the use of smaller earthquakes and multi-frequency measurements to improve the time and vertical resolution of the

estimates (Wu et al., 2023; Callies et al., 2023). In this study, we use an abundance of repeating earthquakes along the Japan Trench (Igarashi, 2020) to sample the variability of the Kuroshio Extension region arising from current shifts, meanders, and mesoscale eddies. The T waves have been received at the CTBTO hydrophone station H11 near Wake Island since 2008. They can also be detected at the WAKE seismic station on the island itself, which provides a digital record reaching back to the 1990s and thus into the pre-Argo era.

The earthquakes used here are spread over a distance of a few hundred kilometers along the Japan Trench (Fig. 2.1a), a distance that is comparable to the size of the Kuroshio Extension's meanders and the eddies shed by it (Fig. 2.1b). The travel time of a T wave to Wake Island will therefore substantially depend on the back-azimuth. For example, a wave propagating through a string of cold-core eddies will have a very different longer travel time than a nearby one propagating through a warm anomaly (Fig. 2.1b). We develop an estimation framework that takes this azimuthal dependence into account. We use maximum likelihood estimation to infer covariance and uncertainty parameters, and we invert for the anomaly field as a function of azimuth and time. Although these estimates are still averages over the travel paths of T waves, they clearly exhibit mesoscale signals that are broadly consistent with sea surface elevation data from satellite altimetry, confirming the oceanic origin of the anomalies. We show quantitatively that these oceanic anomalies dominate over source positions and timing uncertainties.

2.3 Observing T waves from repeating earthquakes

We follow a process similar to that described in Wu et al. (2020, 2023) to find repeating earthquakes along the Japan Trench (Fig. 2.1a). To constrain the search, we restrict source properties in the interactive event catalogue search tool of the International Seismological Centre (ISC) Bulletin. We limit the horizontal location to the polygon shown in Fig. 2.1a. We limit the source depth to 0 to 100 km, for which the excitation of T waves tends to be most efficient. We only use earthquakes with magnitudes M 3.0 to 5.5 as candidates for arrivals at H11 and M 3.5 to 5.5 for arrivals at WAKE because smaller earthquakes generate noisy arrivals, especially at WAKE, and because the source complexity of bigger earthquakes makes repeating signals unlikely. We choose the Japan Meteorological Agency (JMA) as the magnitude author due to its high-quality record. The time coverage is 2007 to 2021 for H11 and 1997 to 2021 for WAKE. These choices result in 51,981 and 27,757 events for H11 and WAKE, respectively. Due to the extensive seismic network on and off

Japan, the catalogs are much more complete here than in the study area of Wu et al. (2020, 2023), so no additional earthquake detection needs to be employed.

To identify repeating earthquake pairs and measure the *P*-wave arrival time change to correct the cataloged origin times, we cross-correlate *P* waves at four reference stations MAJO, TSK, ERM, and INU (Fig. 2.1b). We use seismometers from two location codes at MAJO for better time coverage, yet we exclude duplicate pairs at this station. Similar to the procedure described in Wu et al. (2023), we filter *P* waves using a 1.0 to 3.0 Hz band-pass filter for TSK and a 1.5 to 2.5 Hz band-pass filter for MAJO, TSK, and INU to improve the signal-to-noise ratio (SNR). We set a waveform cross-correlation (CC) coefficient threshold of 0.9 for the detection of *P*-wave repeaters and measure the *P* wave arrival time change using the maximum of the CC function. For a more efficient detection, we only cross-correlate events whose cataloged locations are separated by less than 50 km in the horizontal and vertical and whose magnitude difference is less than 1.5. We further exclude repeating pairs with a *P*-wave arrival time change greater than 15 s, which prevents false detections especially at TSK, where waveforms occasionally show spurious spikes or dense sinusoidal oscillations. This procedure yields 18,632 and 15,836 potential pairs for H11 and WAKE, respectively.

To measure the corresponding *T*-wave arrival time changes, we use H11N3, one of six CTBTO hydrophones present near Wake Island, and seismometers from three location codes at WAKE with duplicate pairs excluded (Fig. 2.1b). We apply to the received waveforms a Gaussian filter centered on 2.5 Hz and with a width of 0.5 Hz. Compared to the *P*-wave pairs, the corresponding *T*-wave pairs show reduced waveform correlation. Wu et al. (2020, 2023) ascribed a similar reduction in the East Indian Ocean to source complexity and a changing ocean sound speed field between repeating events, both of which might be important for the Kuroshio measurements as well. The *T*-wave excitation is understood to be confined to a narrow section of the trench, maybe a few tens of kilometers wide (de Groot-Hedlin and Orcutt, 1999; Okal, 2008). Horizontal and vertical refraction by sound speed anomalies due to mesoscale eddies and other transients (e.g., Munk, 1980; Dushaw, 2014) could change the waveforms between repeating events. Interaction with bathymetry, especially the numerous tall seamounts in the region, can further induce mode coupling and reduce the SNR and CC. As in previous work, we set a CC threshold of 0.6 for the *T*-wave pairs and measure the *T* wave arrival time change using the maximum of the CC function as before.
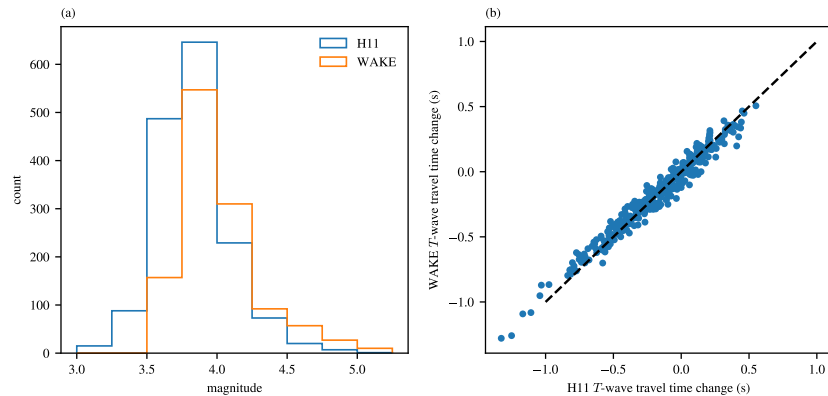
Figure 2.2: Usable repeating earthquakes and observed *T*-wave travel time changes. (a) Histogram of the magnitudes of repeaters detected at H11 (total of 1566 pairs) and WAKE (total of 1201 pairs). (b) Origin-time corrected *T*-wave travel time changes at WAKE vs. H11 for the 363 common repeaters (blue dots). The one-to-one line is shown in black dashed.

Because the energetic Kuroshio Current system produces large *T*-wave travel time anomalies, cycle skipping is common in the CC measurements. This occurs because surface-intensified temperature anomalies shift the *T*-wave group more than its phase, so adjacent peaks in the CC functions are taller than the peak characterizing the correct phase shift (Callies et al., 2023). We apply the correction described in the supplement of Callies et al. (2023), using measurements at 3.5 Hz with a CC threshold of 0.3 to calculate differential delays. We extend this correction approach by also allowing for double cycle skips. The correction procedure also depends on the Bayesian inversion framework to be introduced in the next section.

We additionally exclude a few spurious pairs manually. These pairs may be false detections, suffer from timing errors, or experience three or more cycle skip. We identify these spurious pairs by examining outliers in inversion residuals, cycle-skipping correction clusters, and scatter plots comparing data from H11, WAKE, and altimetry. We exclude a total of 16 and 40 pairs for H11 and WAKE, respectively. This results in a remaining 1566 and 1201 *T*-wave repeaters for H11 and WAKE, respectively, a great reduction in number from their detectable *P*-wave counterparts. As in the Indian Ocean application, compared with the land station, the hydrophone helps detect more repeaters by having a better SNR for small earthquakes (M < 4.0). For larger earthquakes, the detection rates are similar between H11 and WAKE (Fig. 2.2a).

2.4   Inferring anomalies in azimuth and time

Each repeating earthquake pair that passes our selection criteria supplies measurements of one T-wave arrival time change and one to four P-wave arrival time changes. We interpret the P-wave arrival time changes as arising from errors in the cataloged event times and refer to the difference between the T- and P-wave arrival time changes as "T-wave travel time changes". We ascribe all change in the T-wave travel time to changes in the ocean's sound speed between the repeating events and further assume that these sound speed changes are dominated by temperature changes, neglecting much smaller contributions from salinity anomalies and currents (Wu et al., 2020). The T-wave travel anomalies then correspond to kernel-weighted temperature anomalies along the travel path between the two events, i.e., the travel time anomaly τ as a function of azimuth α and time t is

$$\tau(\alpha, t) = \iint K(\alpha, r, z) \, T'(\alpha, r, z, t) \, \mathrm{d}r \, \mathrm{d}z, \qquad (2.1)$$

where K is the sensitivity kernel that can be calculated using SPECFEM2D (cf., Wu et al., 2020) and T is the temperature anomaly field. We assume the sensitivity is confined to the great-circle path, so the integration is in range r and depth z only.

Each usable repeater thus provides a constraint on the time- and azimuth-dependent kernel-weighted temperature anomaly that we would like to infer—but it constrains only its *change* between the event times. To invert for the anomalies themselves, we model the anomaly field as a stationary Gaussian process in time and azimuth, impose a set of prior and noise statistics, and calculate the Gaussian posterior mean and covariance (e.g., Kaipio and Somersalo, 2005; Wunsch, 2006; Sanz-Alonso et al., 2018). Here, a Gaussian process refers to a random function whose values at any finite set of time–azimuth points follow a multivariate Gaussian distribution. We assume a model covariance function in time and azimuth and an error covariance combining various noise terms. We initialize relevant parameters based on altimetry sea-level anomaly calculations and apply previous noise estimates. The initialized prior covariances are applied to the inversion to exclude extreme outliers until a clear clustering pattern emerge from a cycle-skipping correction scheme. We then iterate between the correction scheme and a maximum likelihood estimation to further remove less intense outliers and calibrate the covariance parameters. We stop the iteration once the estimation of parameters has converged.

Formulating the linear inverse problem

To formulate the linear inverse problem, we relate the measurements of T- and P-wave arrival time change δ_T and δ_P between repeating earthquakes to the T- and P-wave arrival time anomalies $\boldsymbol{a}_T$ and $\boldsymbol{a}_P$ at all event times and azimuths involved in a measurement:

$$\boldsymbol{\delta} = \mathbf{E}\boldsymbol{a} + \boldsymbol{n} \quad \text{with} \quad \boldsymbol{\delta} = \begin{pmatrix} \delta_T \\ \delta_P \end{pmatrix}, \quad \mathbf{E} = \begin{pmatrix} \mathbf{X}_T & \mathbf{0} & \mathbf{A} \\ \mathbf{0} & \mathbf{X}_P & \mathbf{0} \end{pmatrix}, \quad \boldsymbol{a} = \begin{pmatrix} \boldsymbol{a}_T \\ \boldsymbol{a}_P \\ \boldsymbol{a}_{\text{fit}} \end{pmatrix}, \quad \boldsymbol{n} = \begin{pmatrix} \boldsymbol{n}_T \\ \boldsymbol{n}_P \end{pmatrix}.$$

(2.2)

The solution vector $\boldsymbol{a}$ contains the T- and P-wave arrival time anomalies as well contributions to the T-wave travel time anomalies from a linear trend as well as annual and semi-annual cycles, represented by $\boldsymbol{a}_{\text{fit}}$. We ignore azimuthal dependencies in the linear trend and the seasonal cycle based on sea level anomaly calculation (details in the next subsection), in which their azimuthal gradients are negligible compared with large-scale averages. The design matrix $\mathbf{E}$ consists of the pair matrices $\mathbf{X}_T$ and $\mathbf{X}_P$ that take differences between the events involved in each measurement and the matrix $\mathbf{A}$ that takes differences between the signals that arise from the linear trend and seasonal signals. Callies et al. (2023) described how these matrices are constructed. Contributions to the measurement errors $\boldsymbol{n}$ will be discussed below.

The T-wave travel time anomalies are obtained by taking the difference between the T- and P-wave arrival time anomalies: $\boldsymbol{\tau} = \mathbf{D}\boldsymbol{a}$, where $\mathbf{D}$ is the difference matrix as defined in Callies et al. (2023). We convert these travel time anomalies to kernel-weighted temperature anomalies $\langle \boldsymbol{T} \rangle = K_B^{-1}\boldsymbol{\tau}$ using the bulk sensitivity $K_B = \iint K\,\mathrm{d}r\,\mathrm{d}z$. We calculate kernels for H11 and WAKE using two source locations separated by 3° in azimuth (141.25°E, 37.00°N and 142.00°E, 39.00°N). These calculations give $K_B = -6.03$ and -6.18 s K^{-1} for H11 and $K_B = -5.96$ and -5.98 s K^{-1} for WAKE. The azimuthal dependence of the bulk sensitivity thus appears to be weak, and we use $K_B = -6$ s K^{-1} throughout. We also exclude any uncertainties associated with this conversion from the uncertainty estimates discussed below.

The sensitivity kernels tend to peak around 1.5 km depth for both receivers (Fig. 2.3). This is similar to kernels used in Wu et al. (2020), Callies et al. (2023), and Wu et al. (2023). There are some differences between the kernels for H11 and WAKE. The kernels for H11 are fairly homogeneous in range and appear to consist primarily of the fundamental acoustic mode (Fig. 2.3ac). The kernels for WAKE, in contrast, exhibit range dependence due to interaction with bathymetry (Fig. 2.3b,d). In
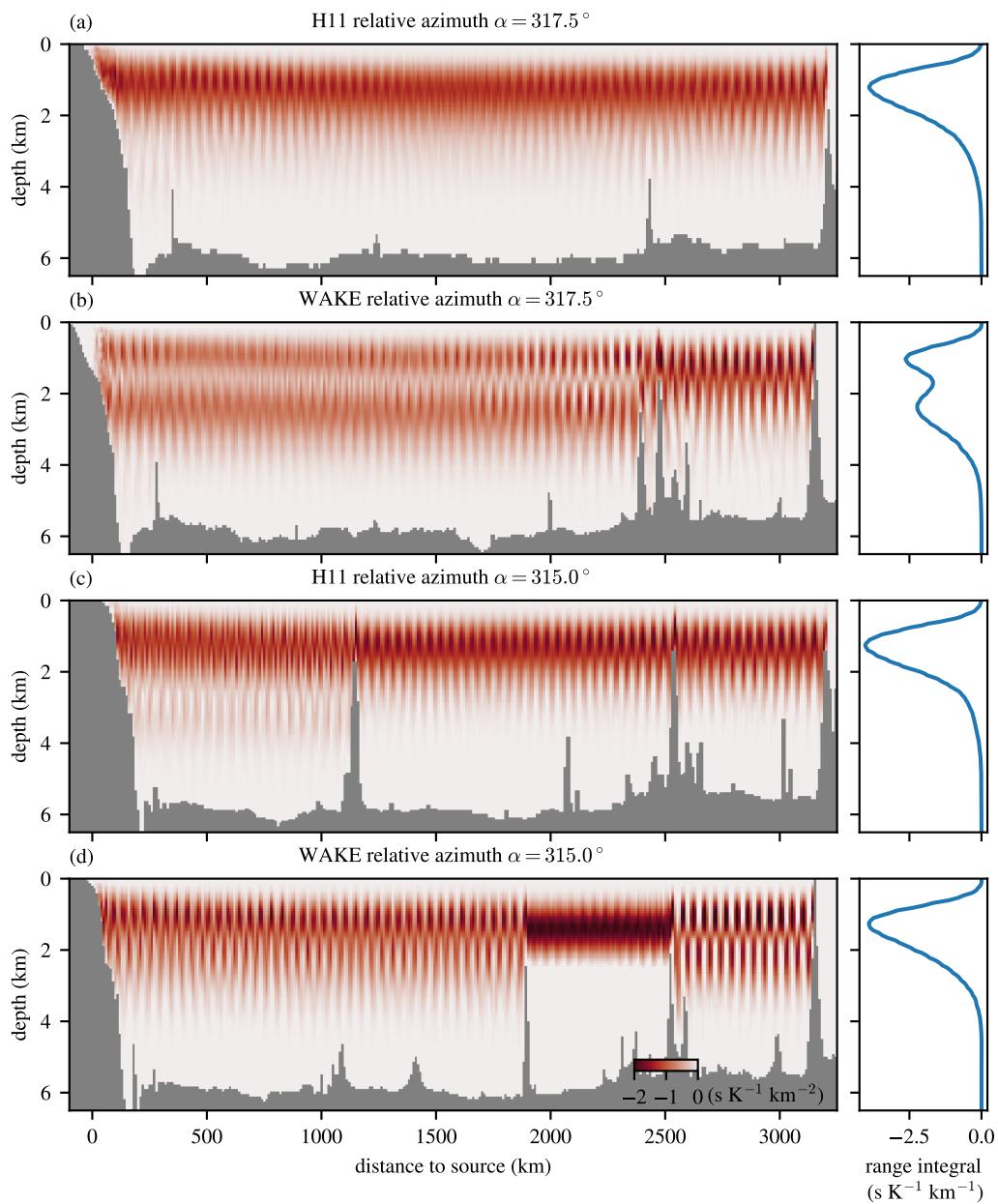
Figure 2.3: *T*-wave sensitivity kernels at the sampling frequency 2.5 Hz from SPECFEM2D numerical simulation. (a,c) Kernels at azimuths $\alpha = 317.5°$ and 315.0° referenced at H11. (b,d) Kernels at the same azimuths referenced at WAKE. Left panels show range-dependent kernels, and right panels show corresponding range integrals.

particular, at azimuth $\alpha = 315.0°$ two seamounts constrain the sensitivity to above 2 km depth between about 2000 and 2500 km from the source, while at azimuth $\alpha = 317.5°$ a group of adjacent seamounts generate complex mode interactions and induce higher-order mode energy within 2500 km from the source. These differences highlight the importance of the bathymetry near the receivers and suggest that T waves received at H11 and WAKE sample different waters even at the same azimuth. It should be noted, however, that three-dimensional propagation effects neglected in the kernel calculations might change the details of the kernels' structure. As discussed below, the two receivers produce very similar travel time anomalies, so we neglect the azimuth dependence of the sensitivity kernels and the ways this would affect covariances of T-wave travel time anomalies.

Constructing prior and noise covariance models

We specify the prior statistics for T-wave travel time anomalies with a correlation structure in both time and azimuth, and we improve on the simple noise covariances used in Wu et al. (2020), Callies et al. (2023), and Wu et al. (2023) to better model source location discrepancy and hydrophone motion in addition to measurement errors arising from noisy waveforms. Furthermore, we employ maximum likelihood estimation to infer the parameters of our covariance model from the data themselves.

We prescribe a time–azimuth covariance function based on range-averaged sea level anomaly inferred from satellite altimetry. While seismic thermometry and satellite altimetry measure different ocean properties—T waves sample the ocean's sound speed with sensitivities peaking at mid-depth, whereas altimetry measures the sea level change due to thermal expansion, haline expansion, and mass variation (e.g., Wunsch and Stammer, 1998)—they have in common that they are sensitive to Kuroshio Extension meanders and mesoscale eddies. The range-averaged sea level anomaly substantially differs from the T-wave signal in that it includes a strong seasonal signal arising from the seasonal warming and cooling of the surface ocean (Gill and Niller, 1973), which is absent in the T-wave data because T waves have little sensitivity near the surface (Fig. 2.3). Once this seasonal signal is removed, the range-averaged sea level and T signals covary significantly, and the altimetry data can be used to estimate the azimuth and time covariance structure of T-wave travel time anomalies.

Specifically, we use the sea level daily gridded data from satellite observations available at the Copernicus Climate Change Service Climate Data Store. We use the

data from 2010 to 2019 at the 1st, 6th, 11th, 16th, 21st, and 26th day of each month and linearly interpolate the anomaly field onto a range of great circle paths from Japan Trench to Wake Island. These paths represent T-wave trajectories with various azimuths. One end of the paths is fixed at the respective receiver location, and the paths are constrained to run through points at 142.86°E and a latitude varying from 33 to 43°N with a resolution of 0.1°. Each path has a length of 3200 km and a range resolution of 10 km. Along each path, we range-average the interpolated anomaly to get a time series for the corresponding azimuth, analogous to how T waves sample the path. We fit to each time series a function consisting of a mean, a linear trend, an annual sinusoid, and a semi-annual sinusoid. We then subtract these fits from the original time series. To calculate the time–azimuth covariance, we subset the result into five overlapped five-year segments with the first year ranging from 2010 to 2015. We then interpolate each chunk onto a regular grid with five-day time resolution and 0.3° azimuth resolution and calculate the two-dimensional power spectrum, averaging over the five chunks. We inverse-transform the power spectrum to get an estimate of the covariance function.

The covariance of these range-averaged sea level anomalies is well-captured by a product between an exponential decay in time and a Gaussian decay in azimuth. Therefore, we assume a stationary and separable time–azimuth covariance function for the stochastic part of the T-wave travel time anomalies: the covariance between times t_i and t_j and azimuths α_i and α_j is

$$C_{ij} = \sigma_\tau^2 \exp\left[-\frac{|t_i - t_j|}{\lambda_t} - \frac{(\alpha_i - \alpha_j)^2}{2\lambda_\alpha^2} \right], \tag{2.3}$$

where λ_t and λ_α determine the correlation scale in time and azimuth, respectively. The deterministic parts of the T-wave travel time anomalies—the linear trend, an annual cycle, and a semi-annual cycle—are assumed mutually independent and independent of the stochastic part. Their prior covariance is prescribed through a diagonal matrix $\mathbf{\Xi}$, and the prior standard deviations are set to $\sigma_t = 0.01$ s yr^{-1} for the trend (corresponding to 1.7 mK yr^{-1}) and $\sigma_a = \sigma_{sa} = 0.1$ s for the seasonal cycle. The above covariance function is intended to be a compromise between simplicity and realism. The stochastic piece is designed to capture typical mesoscale variations, and it may be too simple to capture rapid meanders of the Kuroshio Extension that can occur within days, although the following results imply that the inversion does not excessively smooth some rapid variations implied in the data. Still, future work should aim to apply a more realistic covariance function.

We assign these covariances of the T-wave travel time anomalies to the T-wave arrival time anomalies $\boldsymbol{a}_T$. The T-wave arrival time anomalies $\boldsymbol{a}_T$ also contain the errors in the cataloged event times that we constrain with the P-wave arrival time anomalies $\boldsymbol{a}_P$. We thus prescribe the covariance matrix for the stacked vector $\boldsymbol{a}$ as

$$\mathbf{R} = \begin{pmatrix} \mathbf{C} & \mathbf{0} & \mathbf{0} \\ \mathbf{0} & \mathbf{0} & \mathbf{0} \\ \mathbf{0} & \mathbf{0} & \boldsymbol{\Xi} \end{pmatrix} + \sigma_{\mathrm{o}}^2 \begin{pmatrix} \mathbf{I} & \mathbf{I} & \mathbf{0} \\ \mathbf{I} & \mathbf{I} & \mathbf{0} \\ \mathbf{0} & \mathbf{0} & \mathbf{0} \end{pmatrix}, \tag{2.4}$$

where σ_{o} is the prior standard deviation of the P-wave arrival time anomalies. The T- and P-wave arrival time anomalies arising from these origin time corrections are the same and thus perfectly correlated.

For the measurement error $\boldsymbol{n}$, we assume that it arises from four distinct processes: a discrepancy in the source location of the repeating earthquakes, a difference in the hydrophone location between the two events (for H11 only), and the errors arising from the correlation of noisy P and T waveforms. The location uncertainties are given in terms of corresponding travel time anomalies. We assign different errors for the latter two because the P and T waveforms arise from distinct propagation processes, instrumentation, and data processing. We further assume these four components to be independent and the underlying anomalies to be zero-mean Gaussian random variables. We assign isotropic source and hydrophone location uncertainties and specify the noise statistics

$$\mathbf{N} = \sigma_{\mathrm{s}}^2 \left(\mathbf{E}_{\cos} \mathbf{E}_{\cos}^{\mathrm{T}} + \mathbf{E}_{\sin} \mathbf{E}_{\sin}^{\mathrm{T}} \right) + \sigma_{\mathrm{h}}^2 \left(\mathbf{E}_{T,\cos} \mathbf{E}_{T,\cos}^{\mathrm{T}} + \mathbf{E}_{T,\sin} \mathbf{E}_{T,\sin}^{\mathrm{T}} \right) + \sigma_{\eta}^2 \mathbf{I}_{\mathrm{T}} + \sigma_{\varepsilon}^2 \mathbf{I}_{\mathrm{P}}, \tag{2.5}$$

where σ_{s}^2 is the variance of the source location discrepancy, σ_{h}^2 the hydrophone location variance, σ_{η}^2 the measurement noise variance for T waves, and σ_{ε}^2 the measurement noise variance for P waves. The source and hydrophone location error variances are not diagonal and specified using

$$\mathbf{E}_{\cos} = \begin{pmatrix} \mathbf{X}_{\mathrm{T},\cos} \\ \mathbf{X}_{\mathrm{P},\cos} \end{pmatrix}, \quad \mathbf{E}_{\sin} = \begin{pmatrix} \mathbf{X}_{\mathrm{T},\sin} \\ \mathbf{X}_{\mathrm{P},\sin} \end{pmatrix}, \quad \mathbf{E}_{T,\cos} = \begin{pmatrix} \mathbf{X}_{\mathrm{T},\cos} \\ \mathbf{0} \end{pmatrix}, \quad \mathbf{E}_{T,\sin} = \begin{pmatrix} \mathbf{X}_{\mathrm{T},\sin} \\ \mathbf{0} \end{pmatrix}. \tag{2.6}$$

These matrices consist of trigonometric pair matrices obtained by replacing ± 1 in $\mathbf{X}_{\mathrm{T}}$ and $\mathbf{X}_{\mathrm{P}}$ with $\pm \cos \theta_i$ or $\pm \sin \theta_i$, where θ_i is the azimuth of the event pair i, calculated from the average catalog location of the two events. The hydrophone movement due to local currents is generally expected to be complicated and anisotropic (Nichols and Bradley, 2017), yet the representation as an isotropic Gaussian displacement

used here should be a reasonable first step to account for this uncertainty. The diagonal matrices $\mathbf{I}_T$ and $\mathbf{I}_P$ contain identity sub-matrices for T- and P-wave data, respectively, such that $\mathbf{I} = \mathbf{I}_T + \mathbf{I}_P$. For WAKE data, we set $\sigma_h = 0$. All together, the observed arrival time change vector δ is assumed to be a Gaussian variable with zero mean and covariance $\mathbf{\Sigma} = \mathbf{E}\mathbf{R}\mathbf{E}^T + \mathbf{N}$.

Estimating prior variances, correlation scales, and error variances

Within the formulation above, the measurement covariance matrix $\mathbf{\Sigma}$ is a function of the parameters

$$\boldsymbol{\theta} = (\lambda_t, \lambda_\alpha, \sigma_\tau, \sigma_o, \sigma_s, \sigma_h, \sigma_\eta, \sigma_\varepsilon), \tag{2.7}$$

and the log-likelihood of $\boldsymbol{\theta}$ is

$$\mathcal{L}(\boldsymbol{\theta}) = \log p(\boldsymbol{\delta}|\boldsymbol{\theta}) = -\frac{1}{2}\left(\log\det\mathbf{\Sigma} + \boldsymbol{\delta}^T\mathbf{\Sigma}^{-1}\boldsymbol{\delta} + n\log 2\pi\right), \tag{2.8}$$

where n is the length of the observation vector $\boldsymbol{\delta}$. We do not aim to estimate the variances of the linear trend and seasonality and exclude them from the parameter vector $\boldsymbol{\theta}$ because the data supply but one realization and therefore provide a weak constraint. The maximum likelihood estimator (MLE) of $\boldsymbol{\theta}$ is

$$\hat{\boldsymbol{\theta}} = \underset{\boldsymbol{\theta}\in\mathbb{R}^7}{\arg\max}\,\mathcal{L}(\boldsymbol{\theta}) = \underset{\boldsymbol{\theta}\in\mathbb{R}^8}{\arg\min}\left(\log\det\mathbf{\Sigma} + \boldsymbol{\delta}^T\mathbf{\Sigma}^{-1}\boldsymbol{\delta}\right). \tag{2.9}$$

To obtain the MLE via numerical optimization, we log-transform the parameters, which must all be positive, and use the BFGS quasi-Newton algorithm with a line search satisfying the strong Wolfe conditions (Nocedal and Wright, 2006). We further examine the marginal distribution for each parameter around the MLE, and we compare the results between H11 and WAKE, both for the full population of repeating pairs and for the restricted population of 363 pairs that yield a successful measurement at both receivers. We expect the correlation scales λ_t and λ_α to be comparable to the corresponding scales in the range-averaged sea level anomalies, which gives 71 days in time and $1.6°$ in azimuth.

The MLE using pairs detected at both receivers produces mutually consistent estimates that align with expectations (Fig. 2.4, dashed lines). The distributions for the time correlation scale λ_t from both receivers peak at 60 days, which is in line with typical time scales of the Kuroshio Extension meanders and mesoscale eddies. The distributions for the azimuth correlation scale λ_α center around $2.2°$, which is slightly greater than that inferred from the sea level anomaly covariance, likely due to distributed T-wave excitation. The standard deviation scale σ_τ for the stochastic
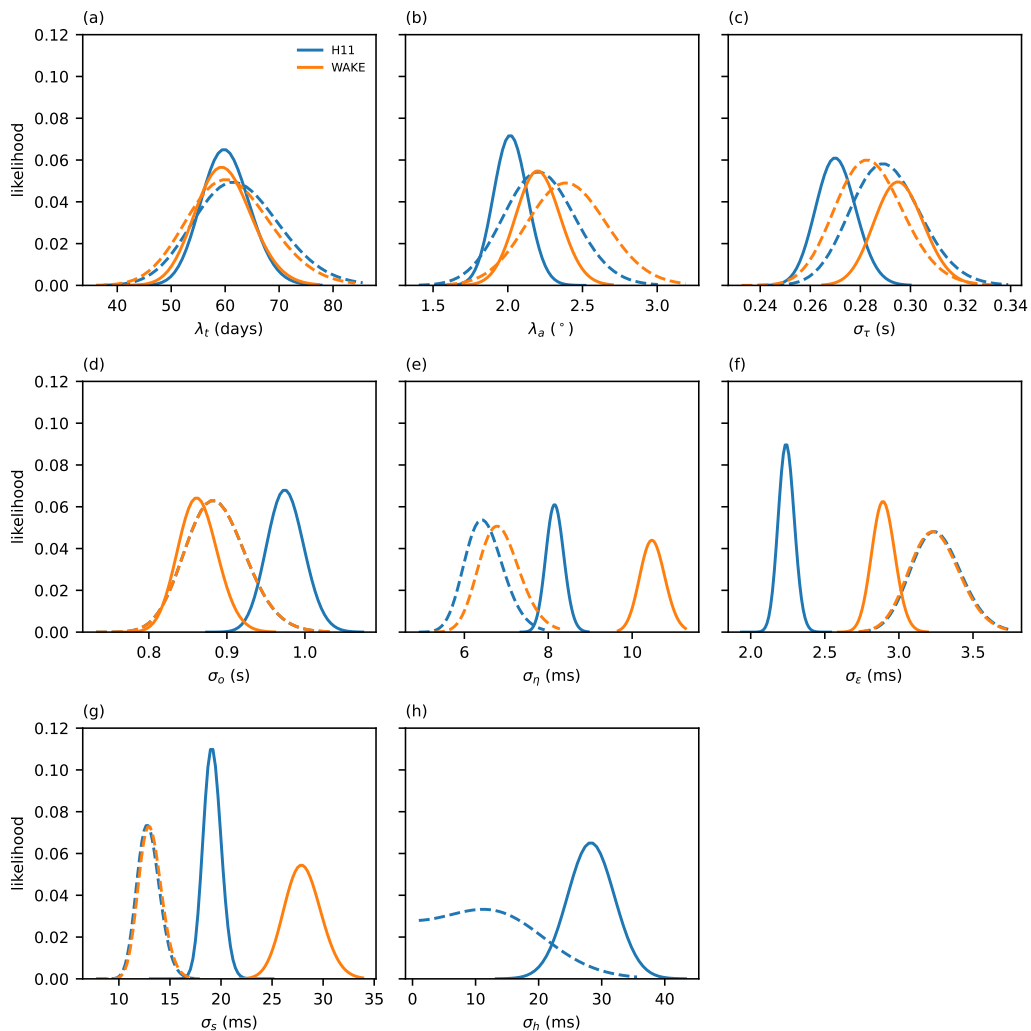
Figure 2.4: Marginal likelihood distributions for H11 (blue) and WAKE (orange). Shown are (a) time correlation scale, (b) azimuth correlation scale, (c) travel time anomaly scale, (d) origin time deviation scale (dashed lines indistinguishable), (e) T-wave instrumental uncertainty, (f) P-wave instrumental uncertainty, (g) source location discrepancy, and (h) hydrophone location uncertainty. Each distribution consists of 50 weighted sample points such that the result is independent of resolution. To calculate the distribution, we independently vary the corresponding parameter around its MLE result while keep other parameters fixed. Dashed and solid lines show distributions using common pairs only and full catalogs, respectively.

part of the travel time anomalies is 0.28 s, equivalent to a temperature anomaly scale of 47 mK.

The two receivers give indistinguishable distributions for the standard deviation σ_o of the P-wave arrival time anomalies that peak at 0.88 s, consistent with the general timing uncertainty of seismic events. The measurement error σ_η is 6.8 ms for WAKE and H11, greater than that arising from P-wave correlation at 3.2 ms. The distribution for the source location discrepancy σ_s peaks at 13 ms, equivalent to a distance on the order of 100 m. The hydrophone data further suggests a receiver location uncertainty σ_h of 11 ms, equivalent to a distance of 17 m. The broad distribution could implies that this error is not well-constrained by just common pairs, which likely contributes to a larger waveform correlation error at H11.

The source location discrepancy distribution provides a quantitative constraint on the T-wave source properties. It demonstrates directly that the uncertainty arising from differences in the source locations of the repeating events is an order of magnitude smaller than the signal arising from temperature changes in the ocean. This result is consistent with the analysis in the supplementary material of Wu et al. (2020). Compared with the noise statistics formulation of Wu et al. (2020), Callies et al. (2023), and Wu et al. (2023), incorporating this effect explicitly reduces the overall uncertainty of the inferred temperature signal. We can also generalize the location covariance to include discrepancies in the depth as well as anisotropy, but we leave this refinement to future work.

Compared to the MLE using only common pairs, estimates with full catalogs of the two receivers tend to be better constrained but also exhibit more pronounced differences between the two receivers (Fig. 2.4 solid lines, Table 2.1). The three parameters characterizing the oceanic variability, the time and azimuth correlation scales λ_t and λ_α, and the T-wave travel time anomaly scale σ_τ have distributions that substantially overlap, both between the two receivers and with the common-catalog estimates. The correlation constants stay around 60 days and 2.0°.

The full-catalog estimate for the origin time correction σ_o is larger for H11, while that for WAKE mostly overlaps with the common-catalog estimate (Fig. 2.4d). This is likely because the smaller earthquakes detected at H11 tend to have larger errors in the cataloged origin time.

The full-catalog T-waveform correlation error σ_η is estimated to be significantly larger for WAKE than for H11, and both estimates are significantly larger than their

common-catalog estimates (Fig. 2.4e). We can understand this error increase as arising from a modest drop in the coherence between waveforms. Both receivers have a mean CC of 0.75 for the common repeaters, but this drops to 0.71 and 0.72 at H11 and WAKE, respectively, when using the full catalog. The differences in travel time changes inferred from the two receivers generally increases as the CC drops, implying that a coherence reduction generally translates into an increased correlation error σ_η. Interestingly, the coherence reduction for a given pair is distinct at the two receivers. In addition to the 363 common repeaters, H11 detects 898 repeaters that do not pass the CC > 0.6 threshold at WAKE, while WAKE detects another 605 repeaters that do not pass the threshold at H11. If the generally lower SNR at WAKE was the main cause for coherence reduction, most pairs detected at WAKE would also be detected at H11. Similarly, if changes in the source properties dominated the coherence loss, the coherence drop should be similar at the two receivers. We therefore suspect that the coherence loss is instead dominated by changes to the waveforms caused by strong ocean perturbation coupled with differences in the sensitivity along the two paths (Fig. 2.3). As a result, for any given pair, one receiver might suffer a coherence drop beyond the threshold when the other suffers a smaller drop that merely leads to an increase in the correlation error σ_η. That said, the higher noise in the waveforms from small earthquakes detected at H11 only likely also contribute to the increased error.

In contrast, the P-waveform correlation error σ_ε is reduced in the full catalogs, significantly so for H11 (Fig. 2.4f). The partition of measurements among the four P-wave stations could matter. INU and ERM detect smaller earthquakes than MAJO and TSK but have worse SNR statistics when averaged over all detections. INU and ERM measurements make up 26.7%, 29.0%, and 28.5% of all measurements for H11, WAKE, and the common catalog, respectively, so the H11 catalog has a larger contribution from the more reliable reference stations MAJO and TSK. Another possible explanation for the drop in the correlation error is that the events detected as repeaters in the full catalogs are more ideally located for good measurements on the P-wave stations. For example, the full catalog includes 51 pairs north of 40°N that are close to ERM station, whereas the common catalog only has one of them.

The reduction in P-waveform correlation error goes along with a significant increase in the source location error σ_o (Fig. 2.4g). This could be because detecting coherent waveforms at both receivers puts a more stringent constraint on the source location properties of the repeating events.

	λ_t (days)	λ_α (°)	σ_τ (s)	σ_o (s)	σ_s (ms)	σ_h (ms)	σ_η (ms)	σ_ε (ms)
H11	60	2.0	0.27	0.97	19	28	8.1	2.2
WAKE	59	2.2	0.29	0.86	28	–	10	2.9

Table 2.1: Parameters used for the time series inversion for H11 and WAKE. The parameter values are inferred using maximum likelihood estimation from the full set of repeating earthquakes detected by the respective receiver.

The most likely hydrophone location error σ_h increases for H11 compared to the common-pair catalog (Fig. 2.4h). The distribution inferred from the common-pair catalog is fairly broad, however, and overlaps substantially with that inferred from the full H11 pair catalog.

Given this discussion, it seems reasonable to use the parameters inferred from the full catalogs in the inversion for T-wave travel time anomalies (Table 2.1). The noise characteristics are then a better representation of the noise present in the respective catalogs used, while the physical parameters are very close to one another for the two stations.

Inverting for posterior distribution

Given covariances with parameters inferred using maximum likelihood estimation (Table 2.1), we solve for the mean $\tilde{a}$ and covariance $\mathbf{P}$ of the Gaussian posterior:

$$\tilde{a} = \mathbf{P}\mathbf{E}^{\mathrm{T}}\mathbf{N}^{-1}\delta \quad \text{and} \quad \mathbf{P} = \left(\mathbf{R}^{-1} + \mathbf{E}^{\mathrm{T}}\mathbf{N}^{-1}\mathbf{E}\right)^{-1}. \tag{2.10}$$

We can obtain the posterior mean of the T-wave travel time anomaly vector τ as $\tilde{\tau} = \mathbf{D}\tilde{a}$, and the corresponding posterior covariance is $\mathbf{D}\mathbf{P}\mathbf{D}^{\mathrm{T}}$.

With the same prior statistics, we can formulate another inverse problem to interpolate these irregular samples of the anomaly field onto a regular time–azimuth grid. We use a grid resolution of 10 days and 0.25°, and we calculate estimates for azimuths between 307.5° and 325.5°. We estimate the arrival time anomalies at the grid points a_g, which as before also includes the fit parameters a_{fit}, for one year at a time:

$$\tilde{a}_g = \mathbf{R}_{\mathrm{ga}}\mathbf{R}^{-1}\tilde{a} = \mathbf{R}_{\mathrm{ga}}\mathbf{E}^{\mathrm{T}}\mathbf{\Sigma}^{-1}\delta, \tag{2.11}$$

where $\mathbf{R}_{\mathrm{ga}}$ is the prior covariance between a_g and a. The gridded travel time anomalies are then inferred as $\tau_g = \mathbf{D}_g\tilde{a}_g$, where $\mathbf{D}_g$ is like $\mathbf{D}$ except that it acts on the gridded arrival time anomalies. The posterior covariance of the gridded travel time anomalies is then $\mathbf{D}_g(\mathbf{R}_{\mathrm{gg}} - \mathbf{R}_{\mathrm{ga}}\mathbf{E}^{\mathrm{T}}\mathbf{\Sigma}^{-1}\mathbf{E}\mathbf{R}_{\mathrm{ga}}^{\mathrm{T}})\mathbf{D}_g^{\mathrm{T}}$, where $\mathbf{R}_{\mathrm{gg}}$ is the prior covariance
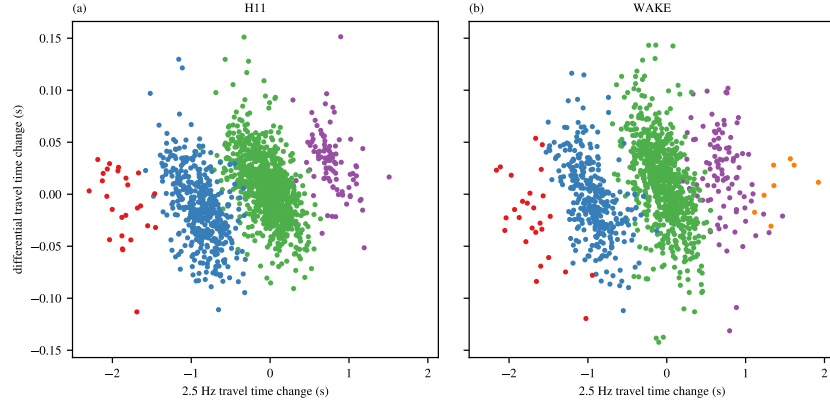
Figure 2.5: Cycle-skipping corrections for the data received at (a) H11 and (b) WAKE. Shown are the differential T-wave travel time changes between 3.5 and 2.5 Hz vs. the corresponding travel time changes at 2.5 Hz. The red and blue dots indicate pairs for which cycle skipping is corrected to the right, the purple and orange dots indicate pairs for which cycle skipping is corrected to the left, and the green dots indicate pairs for which no cycle-skipping correction is made.

matrix for a_g. We estimate the corresponding range-averaged temperature anomalies using the bulk sensitivity, $\langle \tilde{T}_g \rangle = K_B^{-1} \tilde{\tau}_g$, and scale the uncertainty accordingly.

Cycle-skipping correction

The cycle-skipping correction performs a cluster analysis based on Gaussian mixture models and the inversion statistics. It analyzes T-wave pairs in a scatter plot comparing the differential T-wave travel time anomaly between 3.5 and 2.5 Hz with the travel time anomaly at 2.5 Hz. The former can be calculated directly from the data, whereas the latter requires the subtraction of the P-wave arrival time anomaly, so we use $\delta_T - \mathbf{X}_T \tilde{a}_P$. The analysis uses a Gaussian mixture model with four (for H11) and five (for WAKE) members and shared covariance to find clusters of pairs. We perform an initial cycle-skipping correction based on the identified cluster. We then cycle through the T-wave pairs to find additional corrections (or reverse initial corrections) that reduce negative log-likelihood until no further corrections are found. The details of the algorithm are discussed in Callies et al. (2023). To finalize the pair catalog, we iterate between the MLE and cycle-skipping corrections to exclude a few outliers until the MLE does not change with further corrections.

For H11 and WAKE, this procedure corrects about 2% of the pairs to the right twice, 28% of the pairs to the right once, and 6% of the pairs to the left once (Fig. 2.5). For WAKE, a few pairs are also corrected to the left twice (Fig. 2.5b). The fraction of

pairs affected by cycle skipping is greater than in the East Indian Ocean (Wu et al., 2020; Callies et al., 2023; Wu et al., 2023) because travel time anomalies tend to be larger in the Kuroshio Extension region, making cycle skipping more likely.

Testing prior assumptions

An essential step for implementing the inversion is testing the prior assumptions (e.g., Wunsch, 2006; Kuusela and Stein, 2018). We confirm that our prior covariances are a reasonable choice by comparing predictions based on the inversion with measurements from the population of pairs detected at both H11 and WAKE (Fig. 2.6). For each pair in that population, we use the remaining pairs and a Gaussian process regression to predict the measurement for this left-out pair. Specifically, the predictive mean $\hat{m}_{-i}$ and variance $\hat{v}_{-i}$ for the ith arrival time change δ_i are

$$\hat{m}_{-i} = \mathbf{R}_i^{\mathrm{T}} \Sigma_{-i}^{-1} \boldsymbol{\delta}_{-i} \quad \text{and} \quad \hat{v}_{-i} = \Sigma_{ii} - \mathbf{R}_i^{\mathrm{T}} \Sigma_{-i}^{-1} \mathbf{R}_i, \tag{2.12}$$

where $\mathbf{R}_i = \Sigma_i - \sigma_\eta^2 \boldsymbol{e}_i$ is the covariance vector between δ_i and the remaining measurements, $\boldsymbol{e}_i$ the unit vector along the ith dimension, Σ_{-i} and $\boldsymbol{\delta}_{-i}$ the predefined data covariance and vector with the appropriate entries removed, and Σ_{ii} the ith diagonal of Σ. We use parameters from the MLE for the full set of pairs detected at both H11 and WAKE. If the covariance prescription is consistent with the data, it follows that the random variable $(\delta_i - \hat{m}_{-i})/\sqrt{\hat{v}_{-i}}$ is standard Gaussian. Therefore, we can compare the normalized sample quantiles of $\{(\delta_i - \hat{m}_{-i})/\sqrt{\hat{v}_{-i}}, i = 1, \ldots, 363\}$ with the theoretical standard Gaussian quantile.

For both H11 and WAKE, the center of the distribution is close to Gaussian, but the tails are markedly heavy (Fig. 2.6). This is not too surprising, given the complexity of the ocean signal sampled here, arising from strongly nonlinear and thus non-Gaussian Kuroshio Extension meanders and mesoscale eddies, contrasted with the relative simplicity of our statistical model. The heavy tails are reassuring insofar as they indicate that the CC threshold and outlier rejection does not lead to a sample that is strongly biased toward small anomalies. Nonstationarity, especially in azimuth, is another possible explanation for the deviation from the theoretical distribution. Future work should improve our simple covariance model, for example by accounting for the azimuthal dependence of the sensitivity kernel or including prior knowledge based on eddy-resolving ocean circulation models that can capture the nonstationary, non-Gaussian statistics of the real ocean.
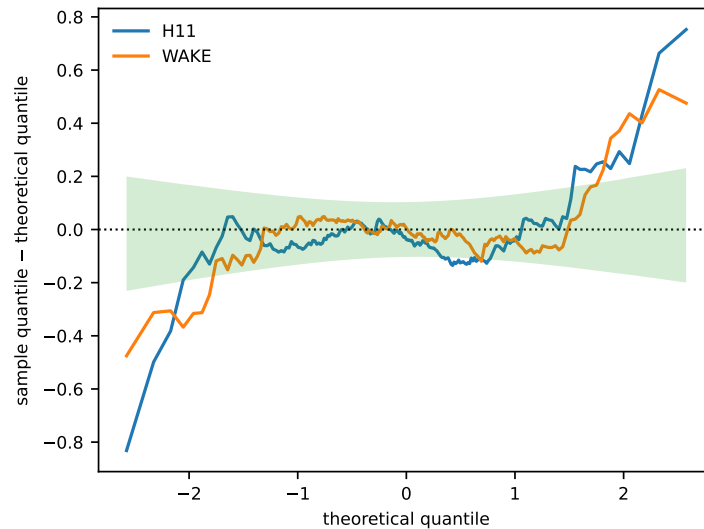
Figure 2.6: Difference between the sample quantile and the corresponding standard Gaussian theoretical quantile ($q_{sample} - q_{theory}$) plotted against the theoretical quantile (q_{theory}) for the leave-one-out cross-validation using the 363 pairs detected at both H11 and WAKE. Shown are quantile differences using H11 data (blue) and WAKE data (orange) as well as a two-sided 95% confidence interval (light green).

Consistency among receivers and with altimetry

For repeating earthquakes successfully detected at both WAKE and H11, the difference between the two measured T-wave arrival time changes has a standard deviation of 0.06 s (Fig. 2.2b). This difference exceeds the size of the errors inferred above, so real differences in the travel times to the two receivers likely contribute. The two receivers are roughly 50 km apart in the direction transverse to propagation (Fig. 2.1b), which is a fair separation for travel time anomalies produced by mesoscale eddies. Differences in the sensitivity kernel for the two receivers might also matter (Fig. 2.3), with WAKE having a more range-dependent sensitivity and a bigger contribution from higher acoustic modes.

The T-wave travel time change between repeating earthquakes is correlated with the corresponding range-averaged sea level anomaly change from altimetry (Fig. 2.7). The sea level data is processed as described above, except that we only use the 1st, 11th, and 21st day of each month here. We again remove the seasonal signal from the sea level data because it is dominated by the upper ocean, where the T waves have little sensitivity. We interpolate the sea level data onto each pair's event times and azimuth. The resulting sea level changes and the T-wave travel time anomalies, turned into weighted-average temperature anomalies using the bulk
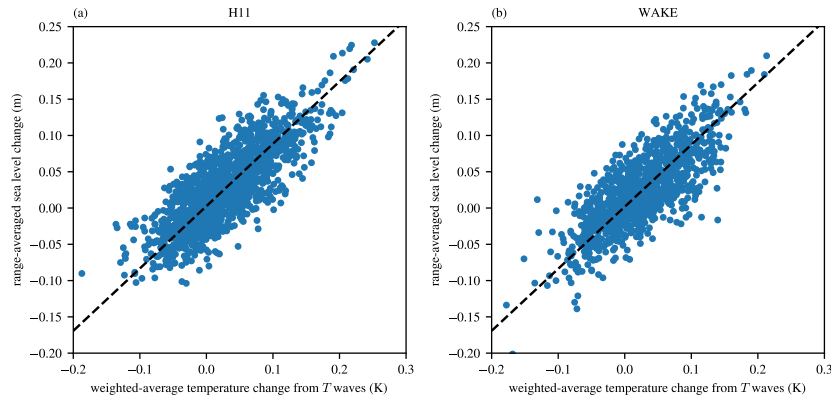
Figure 2.7: Comparison between the weighted-average temperature change inferred from the T-wave arrival time change between repeating earthquakes and the corresponding range-averaged sea level change from altimetry. This comparison is shown for pairs detected at (a) H11 and (b) WAKE. The black dashed lines show the first principal component direction as an indication of the correlation.

sensitivity, show an approximately multivariate normal distribution with positive covariance. The first singular value of the covariance suggest that a 1 K temperature change in the T-waves data corresponds to 0.75 m sea level change in altimetry. The second singular value is about 15% of the first, indicating that the T waves supply information that is statistically independent from the sea level data.

We can further interpret the full covariance between these two measurements as a result of the vertical covariance of temperature anomalies in the ocean. If we assume that the steric change dominates the sea level change, then the sea level change is essentially a vertically-integrated temperature signal weighted by the thermal expansion coefficient. This contrasts with the T-wave sensitivity kernel that peaks at mid-depth and vanishes at the surface (Fig. 2.3). But if temperature anomalies are coherent in the vertical, these two distinct weightings will still produce correlated anomalies. Assuming a covariance model in which temperature anomalies decay exponentially with depth and are correlated with some vertical correlation scale, we can predict the resulting covariance of the two measurements. An MLE applied to all pairs that are separated in time by more than a few correlation scales gives a temperature standard deviation of 0.5 K, a decay scale of 520 m, and a vertical correlation scale of 1040 m. These are all plausible numbers, suggesting that the covariance between the two measurements is as expected.
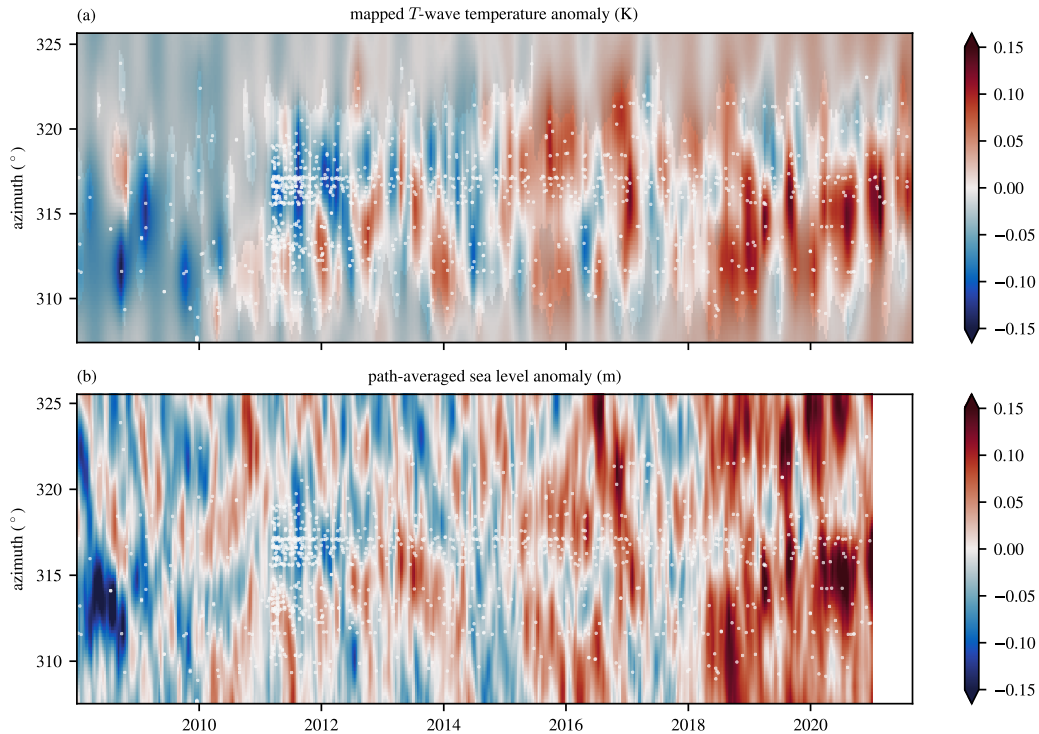
Figure 2.8: Temperature anomalies inferred from the *T* waves received at H11 and corresponding sea level anomalies. (a) *T*-wave temperature anomalies mapped onto a regular time–azimuth grid. The grey shading shows where the posterior variance remains greater than half the prior variance. (b) The range-averaged sea level anomaly, with the seasonal cycle removed yet trend retained. The white dots in both panels show the times and azimuths of earthquakes used in the *T*-wave inversion. Back-azimuths are relative to due north. There is no data from the ISC catalog after August 2021.

2.5 Inferred temperature anomalies

The temperature anomalies inferred from the *T*-wave data are on the order of 0.1 K (Fig. 2.8a, 2.9a). Despite being averaged along the *T*-wave path, these anomalies are dominated by structures that are a few degrees in azimuth and a few tens of days in time, length and time scales consistent with Kuroshio Extension meanders and mesoscale eddies. At times, the inferred temperature differs between a few degrees of azimuth by as much as 0.3 K (e.g., early 2012; cf., Fig. 2.1b). The degree to which these anomalies are resolved by the *T*-wave data varies in time and azimuth due to the inhomogeneous abundance of repeating earthquakes. The M 9.1 Tōhoku earthquake in March 2011 triggered numerous aftershocks, which markedly increase the resolution in the years following the megathrust event. The anomalies inferred from H11 generally have better resolution, but the WAKE data extends much farther
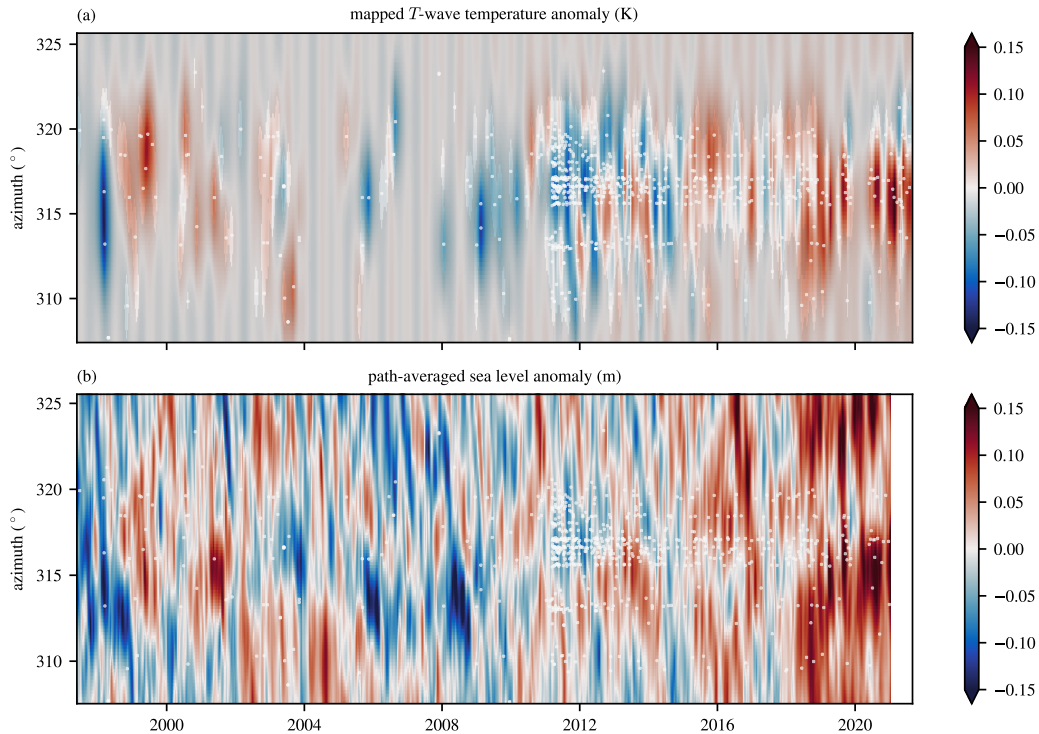
Figure 2.9: Temperature anomalies inferred from the *T* waves received at WAKE and corresponding sea level anomalies. (a) *T*-wave temperature anomalies mapped onto a regular time–azimuth grid. The grey shading shows where the posterior variance remains greater than half the prior variance. (b) The range-averaged sea level anomaly, with the seasonal cycle removed yet trend retained. The white dots in both panels show the times and azimuths of earthquakes used in the *T*-wave inversion. Back-azimuths are relative to due north. There is no data from the ISC catalog after August 2021.

back in time.

Where sufficient resolution is present, the temperature anomalies inferred from the *T*-wave data show a remarkable resemblance to the path-averaged sea level anomalies (Fig. 2.8b, 2.9b). While this can be anticipated from the correlation between the measured *T*-wave arrival changes and the range-averaged sea level change, it strengthens our confidence that the inverted *T*-wave temperature anomalies robustly captures a real physical signal. We emphasize that the correlation between the *T*-wave temperature anomalies and path-averaged sea level anomalies is not expected to be perfect—as discussed above, the correlation depends, among other factors, on how strongly deep and column-averaged temperature anomalies are correlated.

The H11 data show predominantly cold anomalies in 2008 to 2012 and predomi-

nantly warm anomalies in 2015 to 2021 (Fig. 2.8a). As a result, over its full duration from 2008 to 2021, the H11 time series exhibits a warming trend of $4.7\pm1.9\,\mathrm{mK\,yr^{-1}}$. The WAKE data, however, reveal that this is likely a decadal signal rather than a secular trend. While the coverage from WAKE before 2011 is sparse, there are enough constraints reaching back to 1997 to exclude a trend of the size inferred from H11 to extend over this longer time span. The trend for 1997 to 2021 inferred from the WAKE data is 1.1 ± 1.3 mK yr^{-1}. The decadal-scale variations are likely related to the decadal displacements in the Kuroshio Extension path and meander behavior (e.g., Qiu and Chen, 2005; Qiu et al., 2023), but the correspondence between indices commonly used to characterize this variability and the path-averaged signal in the T-wave data needs further investigation.

To compare the T-wave results to previous estimates and better display the uncertainty, we show time series at a few azimuths (Fig. 2.10, 2.11). (Note that our display of the uncertainty in Fig. 2.10 and 2.11 differs from that in Wu et al. (2020), Callies et al. (2023), and Wu et al. (2023). In these previous papers, estimates and uncertainties were shown at event times only. Here, we estimate T-wave anomalies and their uncertainties on a regular grid. The displayed uncertainty thus captures its increase between event times.) We sample the mapped Argo product by Roemmich and Gilson (2009) and the ECCO state estimate v4r4 (ECCO Consortium et al., 2021; Forget et al., 2015) with the T-wave sensitivity kernels at a few azimuths to produce equivalent weighted-average temperature anomalies (cf., Wu et al., 2020; Callies et al., 2023; Wu et al., 2023). There is a broad correspondence between the H11 time series and the Argo estimates, both on decadal and inter-annual time scales (Fig. 2.10a, 2.11a). Given that Argo floats under-sample the mesoscale meanders and eddies (Fig. 2.1b), however, the mapped estimate cannot be expected to capture every variation on a sub-seasonal time scale, and the Argo estimate lies well outside of the 95% confidence range of the T-wave inversion. (Note that no uncertainty estimate is available for the Argo product.) ECCO, fitting a coarse model to available observations, does not capture mesoscale anomalies at all, but there is some correspondence in the inter-annual variations. Over the longer time period, the ECCO and WAKE estimates agree in that they do not display a large secular trend between 1997 and 2021. WAKE samples prior to 2004 are valuable as constraints on the pre-Argo period regardless of its relative sparseness.

As expected from the close correspondence between H11 and WAKE pairs detected by both (Fig. 2.2), the time series inferred from the two are consistent with one
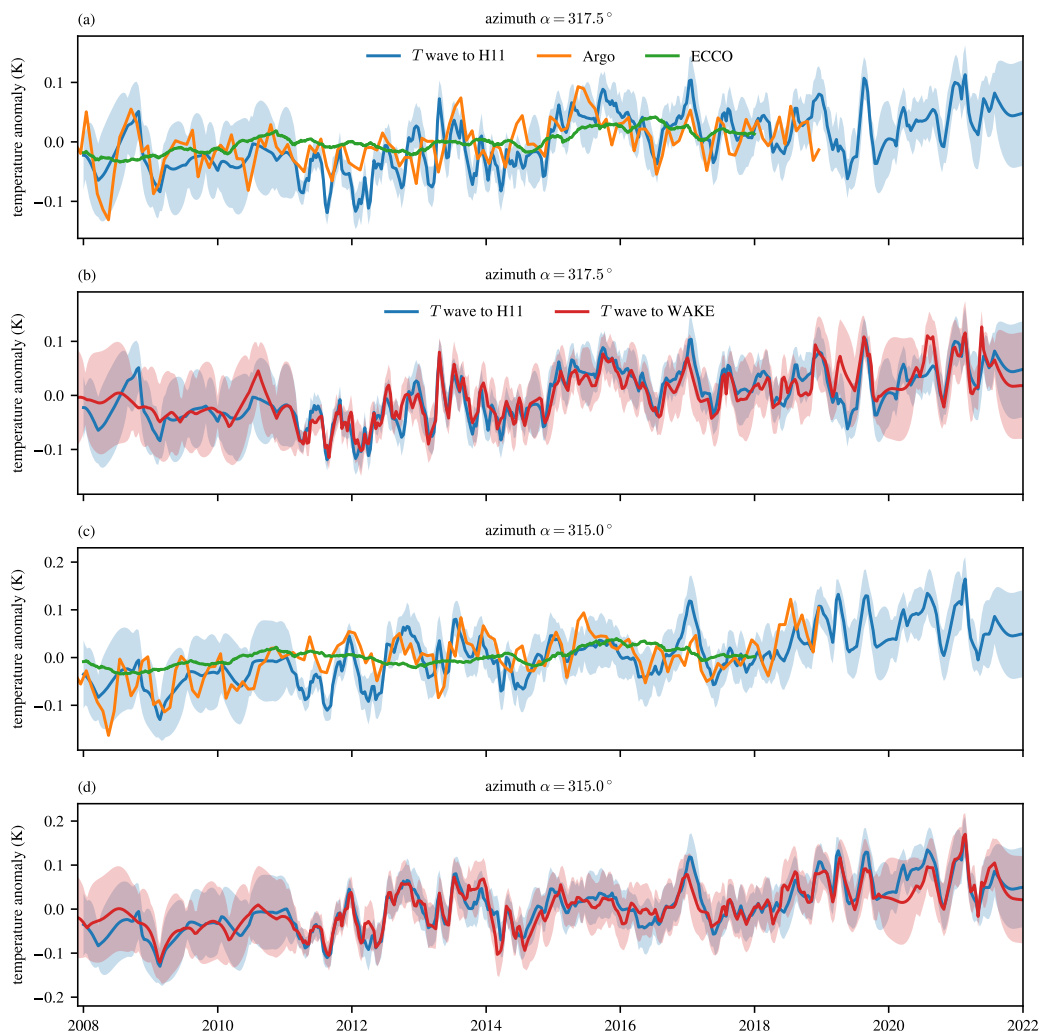
Figure 2.10: Temperature anomalies at two specific azimuths inferred from *T* waves and previous estimates. (a,c) Time series at azimuths $\alpha = 317.5°$ and 315.0° as inferred from *T* waves received at H11 and previous estimates sampled with the corresponding *T*-wave sensitivity kernel. (b,d) Comparison at the same azimuths between the *T*-wave results inferred from H11 and WAKE. The *T*-wave estimates are shown on a regular grid, and the shading shows the $\pm 2\sigma$ uncertainty range.
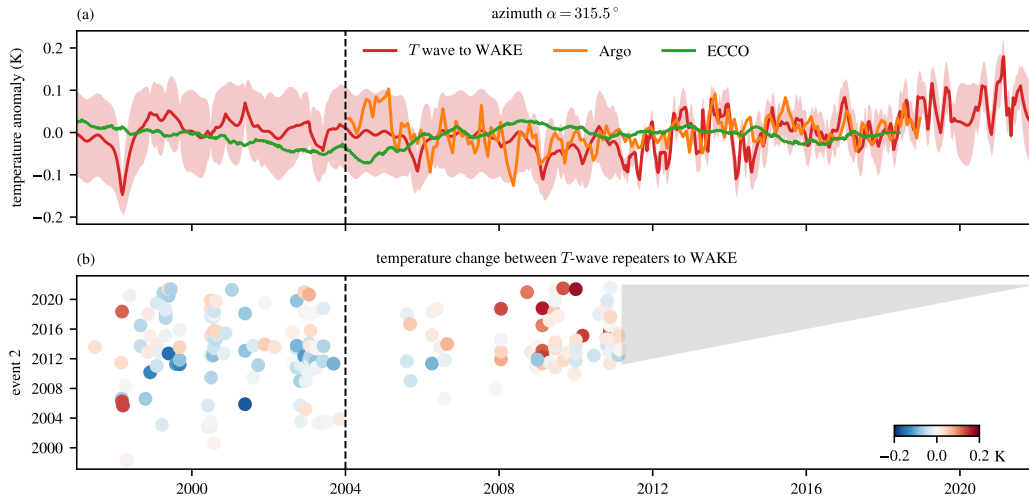
Figure 2.11: Longer-term constraints from the WAKE station. (a) Temperature anomalies at an azimuth $\alpha = 315.5°$ inferred from T waves received at WAKE and previous estimates sampled with the corresponding T-wave sensitivity kernel. The T-wave estimates are shown on a regular grid, and the shading shows the $\pm 2\sigma$ uncertainty range. (b) Pairs detected at WAKE and the corresponding temperature changes. Only those pairs that involve at least one event prior to the Tōhoku earthquake are shown. The many pairs that are not shown would fall into the gray triangle.

another (Fig. 2.10b,d). This is not a trivial result because both stations detect many pairs that the other station does not, and all of these pairs are used in the respective inversion. This confirms that the two stations sample very nearly the same part of the ocean and builds further confidence that the assumptions employed in the inversion are reasonable.

2.6 Discussion

Travel time changes in T waves excited along the Japan Trench and received at Wake Island capture temperature anomalies in the Kuroshio Extension region along the waves' paths. The inferred anomalies vary markedly over just a few degrees of azimuth. At a distance of 3000 km, a degree in azimuth corresponds to a lateral separation of about 50 km between the paths, so these azimuth variations are produced by mesoscale anomalies. This supports the previous attribution by Callies et al. (2023) and Wu et al. (2023) of sharp spikes in the time series of path-averaged temperature anomalies between Sumatra and Cape Leeuwin to mesoscale anomalies. In both regions, the averaging nature of the T-wave measurements over travel paths a thousand kilometers long suppresses the mesoscale anomalies relative to their local values by a factor of ten or so, yet the mesoscale anomalies remain a leading-

order signal. This is in contrast to the ATOC results from the Northeast Pacific, where mesoscale eddies are relatively weak and travel time anomalies varied much more smoothly (The ATOC Consortium, 1998; Dushaw et al., 1999). These results further emphasize the importance of widespread sampling to avoid the aliasing of mesoscale anomalies when attempting to constrain a large-scale signal, especially in eddy-rich regions in the vicinity of western boundary currents and the Southern Ocean.

While we obtain constraints from a total of 1566 T-wave pairs at H11 and 1201 T-wave pairs at WAKE, these numbers are less than a tenth of the number of coherent pairs detected at the land stations. This shortfall is likely due to a combination of the following explanations:

1. Many of the P-wave pairs may be false detections. Because we also require coherent waveforms at the T-wave receiver to consider a pair measurement reliable, we use somewhat less stringent criteria for the detection of repeaters at land stations than previous studies looking to identify repeaters from land stations only (e.g., Uchida and Bürgmann, 2019; Igarashi, 2020).

2. Large-amplitude T waves are excited only by earthquakes that occur sufficiently far east of the trench, which allows efficient coupling of the seismic waves to near-axis waves in the ocean's sound channel (e.g., Okal, 2008). Events that occur too far east and too deep are not ideal either because the seismic waves then suffer substantial loss along their longer solid-earth path. Repeaters not optimally located in relation to the trench produce weak T waves that give rise to noisy signals at the receivers.

3. While the source properties are sufficiently similar between pairs to produce coherent P-wave pairs, they may be sufficiently different for many pairs to produce T waves with substantially different waveforms. T waves are understood to be excited along a section of a trench that exhibits complicated topographic variations, a process that might make the waveforms of T waves an even more sensitive function of the source properties than those of P waves.

4. For many pairs, the change in the ocean's sound speed field may cause changes in the received waveforms even if the excited T waves are highly coherent between the events. There are distinct processes that might cause this loss of coherence:

a) The fundamental acoustic mode that tends to dominate the T-wave signal at low frequencies experiences a greater shift in its travel time at high frequencies than at low frequencies when temperature anomalies are surface-intensified. This property of T waves appears to be the primary cause for cycle skipping and is the basis of our correction scheme (Callies et al., 2023). It also reduces the coherence of the waveforms.

b) If higher acoustic modes contribute to the received waveform, they would experience different travel time shifts than the fundamental mode, so the superimposed arrival pattern will be less coherent than it would be if it consists of the fundamental mode only. Callies et al. (2023) and Wu et al. (2023) attributed the loss of coherence at frequencies higher than 4 Hz to this effect. Higher modes interact strongly with the bottom at low frequencies but progressively contract into the sound channel as the frequency is increased. They can also be excited by mode coupling when T waves encounter bathymetry changes.

c) The excitation of T waves along a section of the trench means that the received waveforms have contributions from a range of azimuths (de Groot-Hedlin and Orcutt, 1999). This raises the possibility that different parts of this multipath experience different temperature changes between the repeating events. If the excitation region is a few tens of kilometers wide, mesoscale anomalies will contribute substantially to such variations across the multipath. If the excitation is substantially narrower, sharp fronts and internal waves can still produce such variations and suppress the waveform coherence.

d) Mesoscale anomalies and shifts in the Kuroshio Extension cause lateral deflections of the T-wave paths (e.g., Munk, 1980; Dushaw, 2014; Heaney and Campbell, 2016) that change between the repeating events. Sufficiently large deflections could produce lensing and thus changes in the received waveforms.

The location of earthquakes in relation to the trench clearly matters: earthquakes that produce a successful T-wave measurement are preferentially located in a band some 200 km east of the trench (Fig. 2.1a). This cannot be the only reason, however, for the reduction of T-wave coherence. We find many families of P-wave repeaters with more than two members. Among the pairs that produce a coherent T-wave signal, there are many families of connected pairs. These families consist of events
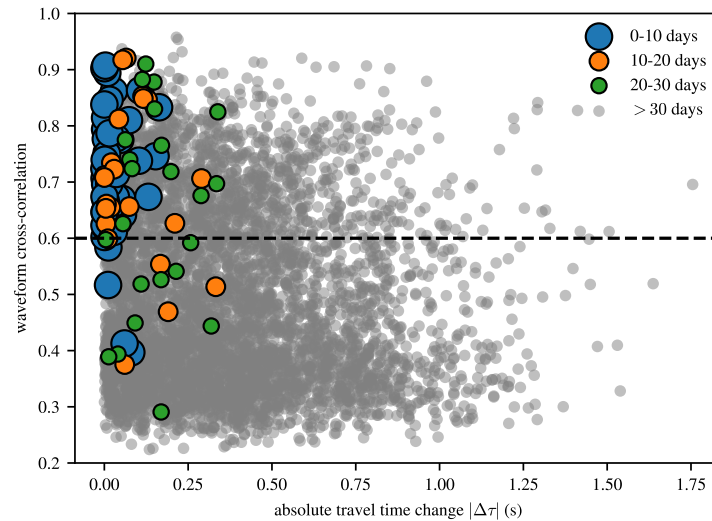
Figure 2.12: Drop in *T*-wave coherence with the repeat interval. Shown is the peak CC for a population of 5214 potential pairs between events that are part of at least one successful detection at H11. We estimate the *T*-wave travel time change of these pairs using the inverted results based on the successful measurements. The potential pairs are split into those with a repeat interval of <10 days (blue), 10 to 20 days (orange), 20 to 30 days (green), and > 30 days (transparent gray). The horizontal dashed line highlights the CC threshold for *T*-wave detection.

that are connected by pairs that pass our CC thresholds for at least one *P*-wave station and the *T*-wave receiver. These families of events therefore likely share very similar source properties, so the excitation of *T* waves should be similarly efficient. Yet, for H11, out of 5214 possible pairs that can be formed by these families of events and that have an SNR greater than two at the receiver, only 1566 events pass our *T*-wave CC threshold of 0.6. We therefore surmise that the waveform coherence is reduced substantially by the propagation through a changing ocean.

The proposition that the *T*-wave propagation through a changing ocean reduces the coherence between repeating pairs is further supported by the observation that the coherence between repeaters systematically drops with the amount of time between the repeating events (Fig. 2.12). We again consider the 5214 possible repeating pairs between events that are involved in at least one successful detection at H11. Of the potential pairs with a repeat interval less than 10 days, 92% have a CC greater than 0.6. For those with a repeat interval of 20 to 30 days, the CC passes this threshold at a rate of 77% and 57%, respectively. For pairs with a longer repeat interval, making up the bulk of the total population, this rate drops to 28%. This drop in waveform coherence over a time scale comparable to the evolution time
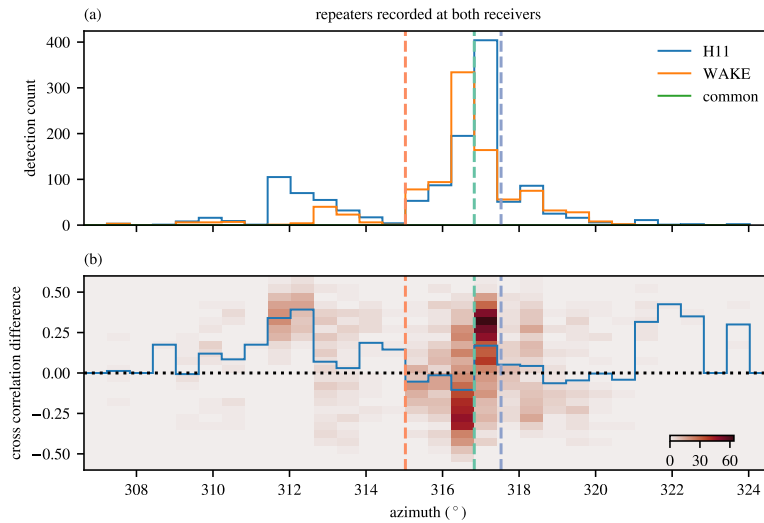
Figure 2.13: Change in *T*-wave coherence with azimuth. (a) Histograms of the number of repeaters detected at H11, WAKE, and both for a total of 1261 pairs recorded by both receivers. (b) Waveform cross-correlation differences between H11 and WAKE for 1830 pairs detected by at least one receiver but available at both. The vertical dashed lines highlight azimuths of 1.0° (blue), 0.3° (green), and −1.5° (orange). The azimuth calculation is referenced to H11. The bin size in azimuth is 0.6°, and the blue curve in (b) shows the mean difference for each bin.

scale of Kuroshio Extension meanders and mesoscale eddies suggests that these changes in the ocean's sound speed field affect the waveform coherence. This effect should be investigated further in future work because it raises the possibility that there is a selection bias for pairs between times at which the current and eddies had similar configurations. Furthermore, understanding this effect better may allow extracting usable information from these many potential pairs. It should also be kept in mind, however, that the mesoscale variability in the Kuroshio Extension region is exceptionally strong, so the loss of coherence seen here is likely rather extreme compared to the rest of the global ocean.

T-wave coherence also varies with azimuth, likely due to local bathymetry, and it is not always better at H11 than at WAKE (Fig. 2.13). At both receivers, most detections are recorded around 316.5°, the azimuth of the M 9.1 Tōhoku earthquake in 2011 that caused a large number of aftershocks. Splitting the azimuth range into 0.6° bins, we find that H11 detects most pairs between 316.8° and 317.4°—more than double the number of detections at WAKE and quadruple the number of common detections in the same bin. WAKE detections, in contrast, maximize between 316.2° and 316.8° at a number also nearly double that of H11 and quadruple

that of common detections. Here, we only consider pairs for which the T waves were received at both stations, excluding periods when one of the stations was not available. Clearly, T waves display a different amount of coherence at the two stations, despite the small azimuth difference. This shift is seen clearly in a histogram of the differences in the CC for all pairs detected by at least one receiver (Fig. 2.13b). We speculate that differences in the bathymetry near the receivers explains this shift in T-wave coherence. The sensitivity kernels for the two receivers at 317.5° do show a larger amount of interaction with bathymetry for WAKE than for H11 (Fig. 2.3a,b). Further work is needed, however, to fully understand these effects.

2.7 Conclusions

Seismically generated sound waves propagating from the Japan Trench to Wake Island can help constrain the deep temperature variability in the Kuroshio Extension region. The change in the travel time of these T waves between repeating earthquakes gives a measurement of a weighted-average temperature change along the waves' path. Thousands of such measurements can be made and combined in a carefully calibrated inversion to estimate the time and azimuth dependence of these path-averaged temperature anomalies. Smaller earthquakes can be detected at the CTBTO station H11, but the island station WAKE has a longer record and allows constraints back to the pre-Argo period. Analog records may yield valuable constraints going even further back in time.

A comparison with altimetry reveals similarities with the T-wave measurements, suggesting that meanders of the Kuroshio Extension and mesoscale eddies produce a large part of the signal. This variability must be captured if long-term changes in the deep ocean are to be confidently inferred. The array of Argo floats, however, captures only part of this variability. Even in its current configuration with some 4000 floats globally, mesoscale eddies are not resolved. As a result, mapped Argo products capture some but not all of the variability seen in the T-wave measurements. Core Argo floats also only sample to 2000 m depth. The T-wave measurements thus offer valuable constraints that should be combined with hydrographic measurements, for example in the ECCO framework (Forget et al., 2015).

This successful application of seismic ocean thermometry in the Kuroshio Extension region encourages a geographic expansion of the approach. While the seismicity produced by the 2011 Tōhoku earthquake and the extensive seismic station network

on Japan are advantageous for seismic ocean thermometry, the vigorous variability produced by the Kuroshio Extension appears to substantially reduce the number of measurements by substantially deforming the waveforms between repeating earthquakes. Applying this method in regions with more modest seismicity but also less vigorous mesoscale eddies may therefore be expected to still produce a large number of useful constraints on changes in deep ocean temperatures.

C h a p t e r   3

ESTIMATING TEMPERATURE VARIABILITY AND TRENDS FROM A COMBINATION OF SEISMIC AND IN SITU DATA

3.1 Abstract

Estimates of the large-scale variability and trends in subsurface ocean temperatures have thus far been based exclusively on in situ observations, which are typically too coarse to resolve mesoscale eddies. Recently, seismically generated sound waves propagating thousands of kilometers along the ocean's acoustic waveguide have been recognized as offering a complementary constraint. The travel time of these waves depends on the temperature of seawater along their path, so they provide integral rather than point constraints. Using earthquakes along the Japan Trench and receivers at Wake Island, it is shown here that these seismic measurements are quantitatively consistent with the conventional in situ data and that combining the two constraints substantially reduces the uncertainty of temperature variability and trends. For example, the error variance of the area-mean stochastic temperature fluctuations due to mesoscale eddies in the period from 2008 to 2021 is reduced by 30% by the conventional data, 39% by the seismic data, and 50% by the combination.

3.2 Introduction

During the past two decades, the Argo program has drastically improved our ability to quantify the variability and trends in subsurface ocean temperatures (e.g., Abraham et al., 2013; Riser et al., 2016). Prior to the Argo era, subsurface measurements from ships were sparse in space and time (e.g., Purkey and Johnson, 2010; Desbruyères et al., 2017), whereas the nearly 4000 autonomous floats currently deployed across the world ocean each sample the top 2000 m of the water column every 10 days. But even with this unprecedented coverage, uncertainties in temperature estimates persist, principally due to the presence of large-amplitude transient eddies that are not resolved by the present array of Argo floats (Wunsch, 2016; Wang et al., 2018, see also Fig. 3.1). To complement ship-based and Argo data, Wu et al. (2020), Callies et al. (2023), Wu et al. (2023), and Peng et al. (2024) recently developed a way to constrain changes in the large-scale temperature of the subsurface ocean using seismically generated sound waves. We here show that such seismic measurements (1) are quantitatively consistent with the conventional temperature data from Argo

floats and (2) reduce the uncertainty in large-scale temperature estimates when combined with the conventional data.

Wu et al. (2020) showed how temperature changes in the subsurface ocean can be measured using acoustic waves generated by repeating earthquakes. Enabled by the ocean's mid-depth waveguide, the waves produced by submarine earthquakes are routinely received far from the generation site after propagation through thousands of kilometers of ocean (e.g., Okal, 2008). Because changes in the speed of sound in seawater are caused primarily by temperature anomalies, changes in the travel time of these waves are proportional to the average temperature anomalies encountered by these waves along their path from the earthquake to the receiver (cf., Munk and Wunsch, 1979; Munk et al., 1995). Wu et al. (2023) improved on the original method by using hydrophones rather than seismic stations on islands as receivers, which made many smaller earthquakes usable and allowed Callies et al. (2023) to extract information on the vertical structure of temperature anomalies. After these initial studies using earthquakes off Sumatra to sample the East Indian Ocean, Peng et al. (2024) applied the same principle to the Kuroshio Extension region using earthquakes along the Japan Trench and a hydrophone station off Wake Island, finding qualitative agreement with altimetry data and previously published estimates of temperature variability in the region.

It has remained challenging, however, to quantitatively demonstrate consistency between these new seismic constraints and previous estimates based on Argo and other conventional data, a prerequisite for making full use of the seismic measurements and combining them with the conventional data. This consistency would require that measured changes in the acoustic travel time fall into the uncertainty range of predictions based on Argo data. Because an acoustic travel time constrains a spatial integral of temperature anomalies, calculating the uncertainty of Argo-based predictions requires knowledge not only of the pointwise uncertainty of temperature anomalies but also of spatial error covariances. Few published estimates provide a pointwise uncertainty, and none, to the best of our knowledge, provide the full error covariance. We therefore develop below a statistical estimation procedure that fully quantifies the uncertainty and shows quantitatively that the two sets of data are in fact statistically consistent.

This new estimation procedure furthermore allows us to combine the conventional and seismic data. We produce improved estimates of temperature anomalies and trends in the Kuroshio Extension region, either averaged over the path of seismic

waves from a point on the Japan Trench to Wake Island or averaged over a sector sampled by waves generated by earthquakes along the Japan Trench (Fig. 3.1). These combined estimates demonstrate that the two data sets are complementary, as quantified by the uncertainty reduction achieved by incorporating the seismic data into an estimate based on conventional data only. We contextualize the results by mapping out multidecadal trends in the region.

3.3 Estimation procedure

Our goal is to estimate temperature variations in the subsurface ocean from a combination of conventional in situ measurements and travel time measurements of seismically generated acoustic waves, so-called T waves. We put the two data sources on an equal footing by weighting the conventional profile data according to the sensitivity kernel of T waves. At the low acoustic frequencies used here, T waves propagate approximately as the fundamental acoustic mode, whose phase speed depends on the sound speed over a wide swath of the water column, with a peak in the mid-depth waveguide and a zero at the surface (Fig. 3.2b). Measurements of the travel time of T waves thus constrain a weighted average of the temperature anomaly profile (Fig. 3.2a,c).

It is convenient to work with anomalies of the slowness of the fundamental acoustic mode, the inverse of its phase speed, because travel time anomalies are then simply range integrals of these slowness anomalies. At any position and time, the slowness anomaly s' is related to the profile of temperature anomalies T' by

$$s'(x, y, t) = \int K(x, y, z) \, T'(x, y, z, t) \, \mathrm{d}z, \tag{3.1}$$

where K is the local sensitivity kernel and the integration is over the full water column. The slowness anomaly is directly proportional to the weighted average of the temperature anomaly, with the weighting defined by the sensitivity kernel:

$$\langle T' \rangle (x, y, t) = \frac{\int K(x, y, z) \, T'(x, y, z, t) \, \mathrm{d}z}{\int K(x, y, z) \, \mathrm{d}z} = -\alpha \, s'(x, y, t), \tag{3.2}$$

where

$$\alpha^{-1} = \int K(x, y, z) \, \mathrm{d}z \tag{3.3}$$

is roughly uniform in space, depending solely on the sensitivity of the sound speed to temperature. Its value of $\alpha = 1.875$ ms km^{-1} K^{-1} allows us to convert slowness anomalies to weighted temperature anomalies. All of our calculations are performed
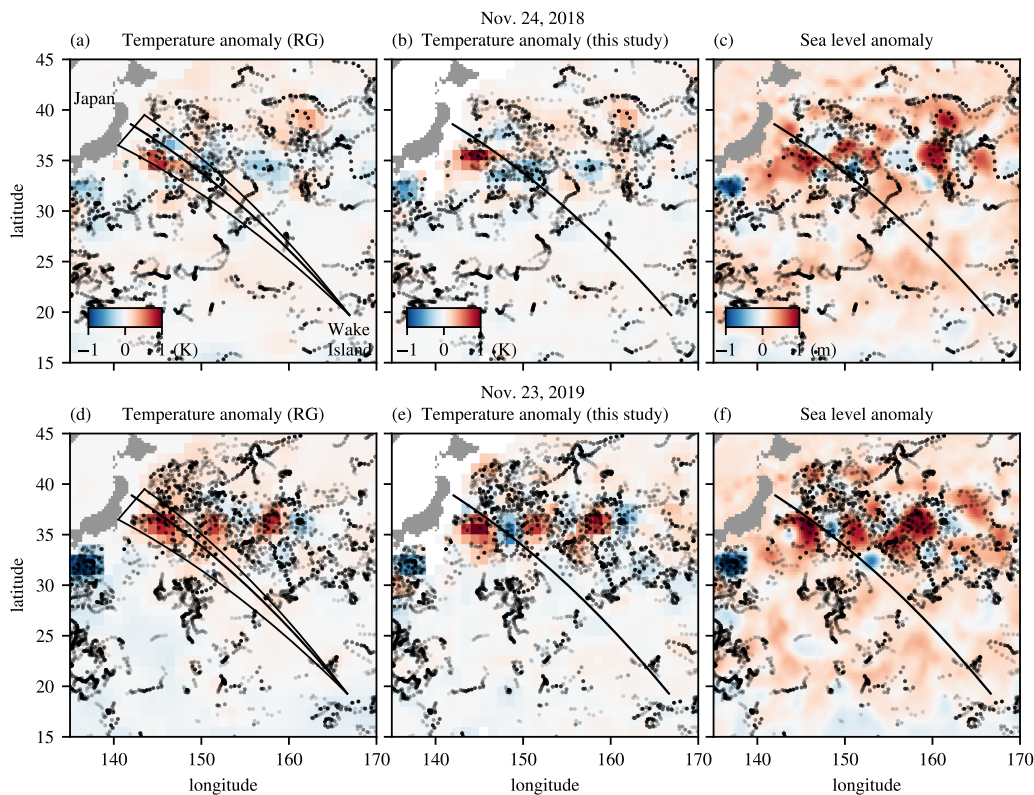
Figure 3.1: Comparison between previous estimates of temperature anomalies, our estimates of temperature anomalies, and sea level anomalies from satellite altimetry. Two dates in the recent Argo era are shown (24-11-2018 and 23-11-2019), when the sampling in the Kuroshio Extension region was dense but still did not resolve the full mesoscale eddy field. Panels (a,d) show the product by Roemmich and Gilson (2009, RG), whereas panels (b,e) show our estimate based on conventional data only. The locations of the Argo float and shipboard CTD profiles used in our estimation on these days are shown by black markers, with the transparency proportional to the correlation with the mapped day. Only data within ±2 correlation scales of the mapping date are included in the inversion. All temperature anomalies are the weighted profile averages defined in (3.2). The sea level anomaly maps in panels (c,f) are relative to the time mean from 1993 to 2012. The black line in (a,b,c) show the T-wave path to the hydrophone station H11 at an azimuth of $\theta = 316.5°$, and the corresponding line in (d,e,f) shows the path to the seismic station WAKE at $\theta = 317.1°$. The black frames in (a,d) shows the region over which we estimate the area mean for the H11 and WAKE time series, respectively.
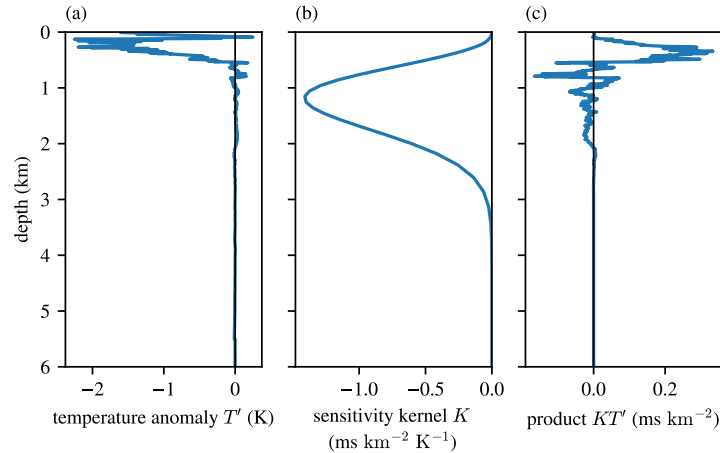
Figure 3.2: Weighting of the temperature anomaly profile from an example CTD cast. Shown are (a) the temperature anomaly T' sampled at 37°N, 150°E on 07-05-2014, (b) the sensitivity kernel K calculated from the local fundamental acoustic mode at 2.5 Hz, and (c) the product of the two illustrating the contributions to the local slowness anomaly s' or equivalently the weighted average of the temperature anomaly $\langle T' \rangle$.

in terms of slowness anomalies, but we display the results converted to temperature anomalies using this conversion factor.

We calculate the local sensitivity kernel K by solving an eigenvalue problem for the structure of the fundamental mode at the acoustic frequency of 2.5 Hz (e.g., Munk et al., 1995), at which we make all measurements of T waves. We base this calculation on the time mean slowness field from the ECCO state estimate (Forget et al., 2015; ECCO Consortium et al., 2021) averaged over 2008 to 2017 and the Gibbs Seawater Toolbox (McDougall and Barker, 2011). At each grid point in the region, we solve a finite-element version of the eigenvalue problem for the mode structure $P(x, y, z)$ and calculate the kernel as $K(x, y, z) = -\alpha P^2(x, y, z)$, using the normalization

$$\int P^2(z) \, dz = 1. \tag{3.4}$$

Although this simple calculation ignores the acoustic energy in higher modes, it captures the bulk structure of the T-wave sensitivity kernel estimated from more complete calculations (Wu et al., 2023).

We illustrate this weighting with an example of a full-depth shipboard conductivity–temperature–depth (CTD) profile (Fig. 3.2). All temperature anomalies are taken relative to the time mean from the 2018 World Ocean Atlas (WOA) based on the time
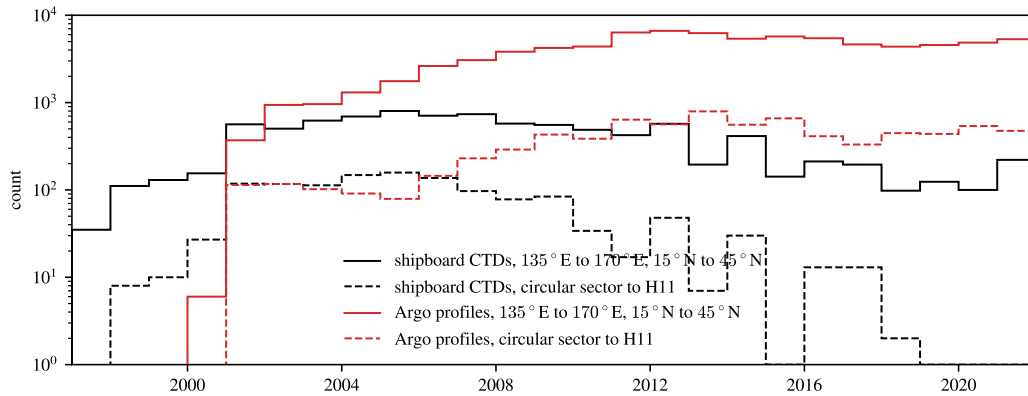
Figure 3.3: Temporal distribution of conventional data. Shown are annual sample counts for shipboard CTD casts (black) and Argo profiles (red). Solid curves show data from 135°E to 170°E, 15°N to 45°N, and dashed curves show data in a triangular area illustrated in Fig. 3.1a.

span from 2005 to 2017 (Garcia et al., 2019). As is typical, the anomalies in this profile are largest in the upper 1 km of the water column, so much so that they still dominate the weighted average despite the small weight in the near-surface waters. Contributions from below 2 km are small, so the fact that most Argo floats only profile to this depth has a negligible impact on the weighted temperature anomalies considered here.

We use two sets of T-wave observations, one from the Comprehensive Nuclear-Test-Ban Treaty Organization (CTBTO) hydrophone station H11 to the north of Wake Island (2008 to 2021) and one from the seismic station WAKE on Wake Island (1997 to 2021). Data selection and processing are described in Peng et al. (2024). Aside from measurements of T-wave arrival time changes between repeating earthquakes, the data also include P/S-wave arrival time changes at land stations to correct for errors in the cataloged origin times. We use a total of 1566 T-wave arrival time change measurements at H11 and 1201 such measurements at WAKE.

We use shipboard CTD data from the World Ocean Database (Boyer et al., 2018), and we use the argopy library to extract Argo data through the ERDDAP data service (Simons and John, 2022). We retrieve data from 135°E to 170°E, 15°N to 45°N, and from 05-06-1997 to 31-12-2021. We keep shipboard data that reached below 2 km depth and Argo data that reached below 1.9 km depth. When subtracting the WOA reference and projecting the resulting temperature anomalies onto the local sensitivity kernel, we retain only those with the closest reference profile reaching

below 2 km. We also exclude data in the Sea of Japan and outliers that give absolute slowness anomalies greater than 10 ms km^{-1}. This produces a total of 9265 shipboard CTD profiles and 80,789 Argo profiles (Fig. 3.3). Shipboard CTD data is most abundant in the mid-2000s, while Argo data show a steady coverage starting late 2011.

The task is then to estimate spatial maps or spatial averages of the weighted temperature anomalies, which we break up into (1) a stochastic component that is dominated by meanders of the Kuroshio Extension and mesoscale eddies, (2) a linear trend over the duration of the data set, (3) a seasonal signal that consists of an annual component and a semi-annual component, and (4) a time mean offset from the WOA. We denote the combination of the desired quantities by the vector $\boldsymbol{x}$, and we estimate it given the observations $\boldsymbol{y}$.

Assuming that both $\boldsymbol{x}$ and $\boldsymbol{y}$ have Gaussian prior statistics with zero mean and covariances $\mathbf{R}_{xx}$, $\mathbf{R}_{xy}$, and $\mathbf{R}_{yy}$, we can use a general Gauss–Markov estimator to obtain the posterior mean and covariance (e.g., Wunsch, 2006)

$$\tilde{\boldsymbol{x}} = \mathbf{R}_{xy}\mathbf{R}_{yy}^{-1}\boldsymbol{y}, \quad \mathbf{P} = \mathbf{R}_{xx} - \mathbf{R}_{xy}\mathbf{R}_{yy}^{-1}\mathbf{R}_{xy}^{\mathrm{T}}. \tag{3.5}$$

We can split up the observations $\boldsymbol{y}$ into conventional observations $\boldsymbol{a}$ and seismic observations $\boldsymbol{b}$. The conventional observations are the slowness anomalies s' inferred from Argo floats and shipboard CTD casts, whereas the seismic observations are T- and P/S-wave arrival time changes between repeating earthquakes. With the observations and their covariance written as

$$\boldsymbol{y} = \begin{pmatrix} \boldsymbol{a} \\ \boldsymbol{b} \end{pmatrix} \quad \text{and} \quad \mathbf{R}_{yy} = \begin{pmatrix} \mathbf{R}_{aa} & \mathbf{R}_{ab} \\ \mathbf{R}_{ab}^{\mathrm{T}} & \mathbf{R}_{bb} \end{pmatrix}, \tag{3.6}$$

we can then obtain estimates based on the conventional data only,

$$\tilde{\boldsymbol{x}}_a = \mathbf{R}_{xa}\mathbf{R}_{aa}^{-1}\boldsymbol{a}, \quad \mathbf{P}_a = \mathbf{R}_{xx} - \mathbf{R}_{xa}\mathbf{R}_{aa}^{-1}\mathbf{R}_{xa}^{\mathrm{T}}, \tag{3.7}$$

or the seismic data only,

$$\tilde{\boldsymbol{x}}_b = \mathbf{R}_{xb}\mathbf{R}_{bb}^{-1}\boldsymbol{b}, \quad \mathbf{P}_b = \mathbf{R}_{xx} - \mathbf{R}_{xb}\mathbf{R}_{bb}^{-1}\mathbf{R}_{xb}^{\mathrm{T}}. \tag{3.8}$$

We can also rewrite the combined estimate, using the block matrix formula for $\mathbf{R}_{yy}^{-1}$, as

$$\tilde{\boldsymbol{x}} = \left(\mathbf{R}_{xa} - \mathbf{R}_{xb}\mathbf{R}_{bb}^{-1}\mathbf{R}_{ab}^{\mathrm{T}} \right) \mathbf{P}_{a\,|\,b}^{-1}\boldsymbol{a} + \left(\mathbf{R}_{xb} - \mathbf{R}_{xa}\mathbf{R}_{aa}^{-1}\mathbf{R}_{ab} \right) \mathbf{P}_{b\,|\,a}^{-1}\boldsymbol{b} \tag{3.9}$$

with the posterior covariance

$$\mathbf{P} = \mathbf{R}_{xx} - \left(\mathbf{R}_{xa} - \mathbf{R}_{xb}\mathbf{R}_{bb}^{-1}\mathbf{R}_{ab}^{\mathrm{T}}\right)\mathbf{P}_{a\,|\,b}^{-1}\mathbf{R}_{xa}^{\mathrm{T}} - \left(\mathbf{R}_{xb} - \mathbf{R}_{xa}\mathbf{R}_{aa}^{-1}\mathbf{R}_{ab}\right)\mathbf{P}_{b\,|\,a}^{-1}\mathbf{R}_{xb}^{\mathrm{T}}, \quad (3.10)$$

where $\mathbf{P}_{a\,|\,b} = \mathbf{R}_{aa} - \mathbf{R}_{ab}\mathbf{R}_{bb}^{-1}\mathbf{R}_{ab}^{\mathrm{T}}$ and $\mathbf{P}_{b\,|\,a} = \mathbf{R}_{bb} - \mathbf{R}_{ab}^{\mathrm{T}}\mathbf{R}_{aa}^{-1}\mathbf{R}_{ab}$. This decomposition avoids the inversion of the full matrix $\mathbf{R}_{yy}$ and shows how the two data sources contribute to the uncertainty reduction.

This estimation procedure requires us to specify the various covariances. We begin by specifying the spatiotemporal covariance function of the stochastic component of the slowness anomalies that represents mesoscale eddies. The covariance between the points (x_i, y_i, t_i) and (x_j, y_j, t_j) is assumed to follow the separable form

$$\Xi_{\mathrm{s},ij} = \sigma_{\mathrm{s}}^2 \sqrt{2} \exp\left(-\frac{|t_i - t_j|}{\lambda_{\mathrm{t}}} - \frac{d_{ij}}{\lambda_{\mathrm{d}}}\right) \cos\left(\frac{d_{ij}}{\lambda_{\mathrm{d}}} - \frac{\pi}{4}\right), \quad (3.11)$$

where d_{ij} denotes the great-circle distance between the two points. This functional form is inspired by wavenumber spectra inferred from satellite altimetry (Callies and Wu, 2019; Lawrence and Callies, 2022) and corresponds to a high-wavenumber roll-off of k^{-4}.

We anticipate that decadal-scale trends in this region are dominated by changes in the transport and path of the Kuroshio Extension (e.g., Qiu and Chen, 2005; Wu et al., 2012; Wu et al., 2021), so we impose a comparably short spatial correlation scale of $\lambda_0 = 200$ km for the linear trend, and we allow for large trends of order $\sigma_{\mathrm{t}} = 34$ µs km^{-1} yr^{-1} (18 mK yr^{-1}). Likewise, we allow for the estimate of time-mean offsets from the WOA reference with the same spatial correlation scale and a magnitude σ_{m}. The covariance functions associated with these two components of the slowness anomalies is thus

$$\Xi_{\mathrm{t},ij} = \sigma_{\mathrm{t}}^2 (t_i - t_{\mathrm{m}})(t_j - t_{\mathrm{m}}) \exp\left(-\frac{d_{ij}}{\lambda_0}\right), \quad \Xi_{\mathrm{m},ij} = \sigma_{\mathrm{m}}^2 \exp\left(-\frac{d_{ij}}{\lambda_0}\right), \quad (3.12)$$

where t_m is the midpoint of the time period under consideration. We note that the seismic measurements constrain the trend but not the time mean offset because they are measurements of arrival time changes, not absolute measurements of the travel time (Wu et al., 2020). These ingredients are enough to formulate the point-point covariance $\mathbf{R}_{aa}$ for the conventional data.

We estimate the variances σ_{s}^2, σ_{m}^2 and correlation scales λ_{t}, λ_{d} with a maximum likelihood estimator (MLE). We only use Argo data before 01-08-2021 and within a sector defined by the back-azimuths 310° and 320° at the WAKE station relative

to due north (Fig. 3.1d). This spatial constraint equivalent to the area mean to be estimated below, and it results in 7555 profiles dating back to 25-02-2001. The following MLE formulation and numerical implementation are similar to those described in Peng et al. (2024). We initialize the parameters with $\sigma_s = \sigma_m = 0.5$ ms km^{-1}, $\lambda_t = 60$ days, $\lambda_d = 100$ km and set a relative tolerance to 10^{-3}. The estimation gives a time scale $\lambda_t = 60$ days with a 95% confidence interval $(55\,\text{d}, 65\,\text{d})$ and a horizontal scale $\lambda_d = 103$ km with a 95% confidence interval $(100\,\text{km}, 106\,\text{km})$. These are consistent with typical characteristics of mesoscale eddies. The corresponding stochastic amplitude is $\sigma_s = 0.55$ ms km^{-1} with a 95% confidence interval $(0.53\,\text{ms km}^{-1}, 0.57\,\text{ms km}^{-1})$, and the offset amplitude is $\sigma_m = 0.44$ ms mm^{-1} with a 95% confidence interval $(0.41\,\text{ms km}^{-1}, 0.46\,\text{ms km}^{-1})$. Because the Argo profiles are concentrated around the meanders of the Kuroshio Extension that exhibits extreme variability compared to the mesoscale eddy field in the remainder of the region, we suspect the stochastic amplitude to be over-estimated and not representative of what T waves have sampled. Therefore, we adjust the magnitude of the stochastic fluctuations in the following calculation to be the same as the offset amplitude, i.e., $\sigma_s = \sigma_m = 0.44$ ms mm^{-1}. We also use a slightly adjusted spatial scale of $\lambda_d = 100$ km.

We integrate the pointwise covariance functions to obtain covariances between local slowness anomalies, T-wave travel time anomalies τ', and area-mean slowness anomalies $[s']$. The latter two are defined in polar coordinates as

$$\tau'(\theta, t) = \int_0^L s'(r \cos \theta, r \sin \theta, t)\, \mathrm{d}r \tag{3.13}$$

and

$$[s'](t) = \frac{2}{L^2(\theta_2 - \theta_1)} \int_{\theta_1}^{\theta_2} \int_0^L s'(r \cos \theta, r \sin \theta, t)\, r\, \mathrm{d}r \mathrm{d}\theta, \tag{3.14}$$

where r is the distance to the receiver H11 or WAKE, and θ is the azimuth referenced at the respective receiver and relative to due north. The area that we average over is a circular sector (Fig. 3.1a,d). We perform the integration of covariance functions numerically with the h-adaptive scheme implemented in the HCubature module for Julia (Genz and Malik, 1980). We set both the relative and absolute tolerance to 10^{-6} and calculate corresponding covariances involving path- or area-means. The computation in some cases involves numerous integral evaluations, and to reduce computation cost we combine integration on coarser grids with interpolations to approximate the results. Specifically, path–path covariances are evaluated between 0°

and 20° differential azimuth with a 0.05° spacing; path–area covariances are evaluated for paths with azimuths between 306.5° and 326.5°, again with a 0.05° spacing; point–path covariances are evaluated for point that fall within 135°E to 170°E and 15°N to 45°N and for azimuths between 306.5° and 326.5°, all with a 0.1° spacing; and point–area covariances are evaluated on the same latitude–longitude grid. We obtain covariance matrices for the data by linearly interpolating these calculations onto the sampling locations and azimuths.

We calculate path–path covariances for all T-wave events and transform them to covariances of T-wave arrival time changes using a design matrix that takes the difference for each repeating event pair (Peng et al., 2024). We apply the same covariances as in Peng et al. (2024) for P/S-wave arrival time changes and noise statistics of the seismic data. This gives the full seismic covariance $\mathbf{R}_{bb}$. The point–path covariances are evaluated to get $\mathbf{R}_{ab}$. Depending on whether x is pointwise, path-mean, or area-mean slowness anomaly, its covariance $\mathbf{R}_{xx}$ is evaluated from point–point, path–path, or area–area calculations, and the relevant $\mathbf{R}_{xa}$ and $\mathbf{R}_{xb}$ are evaluated accordingly.

If x consists of different components of the pointwise slowness anomaly, the full slowness anomaly s, if desired, can be calculated by adding the stochastic piece, the trend, and the seasonal cycle. This can be written as $\tilde{s} = \mathbf{D}\tilde{x}$, and the posterior variance is $\mathbf{DPD}^{\mathrm{T}}$. These slowness anomalies are converted to temperature anomalies using the conversion factor α. Analogous transformations are applied when x involves path- or area-mean anomalies.

3.4   Results

The following three subsections demonstrate that the seismic data quantitatively agree with the conventional data and that temperature times series can be improved by combining the two data sets. The unknown x is different in each subsection. For a systematic comparison between the seismic and conventional data, we constrain it using conventional observations from within a specific circular sector, collected in the vector a, and T-wave observations that fall within the corresponding azimuth range, collected in the vector b. We define these areas with the origin placed on the T-wave receiver, either H11 or WAKE, a radius of $L = 3200$ km, and an azimuth range from $\theta = 310°$ to $320°$ (Fig. 3.1a,d). We constrain the time periods to those with data available from the T-wave receivers: 12-16-2007 to 31-07-2021 for H11 and 06-05-1997 to 31-07-2021 for WAKE. This results in 7457 conventional samples
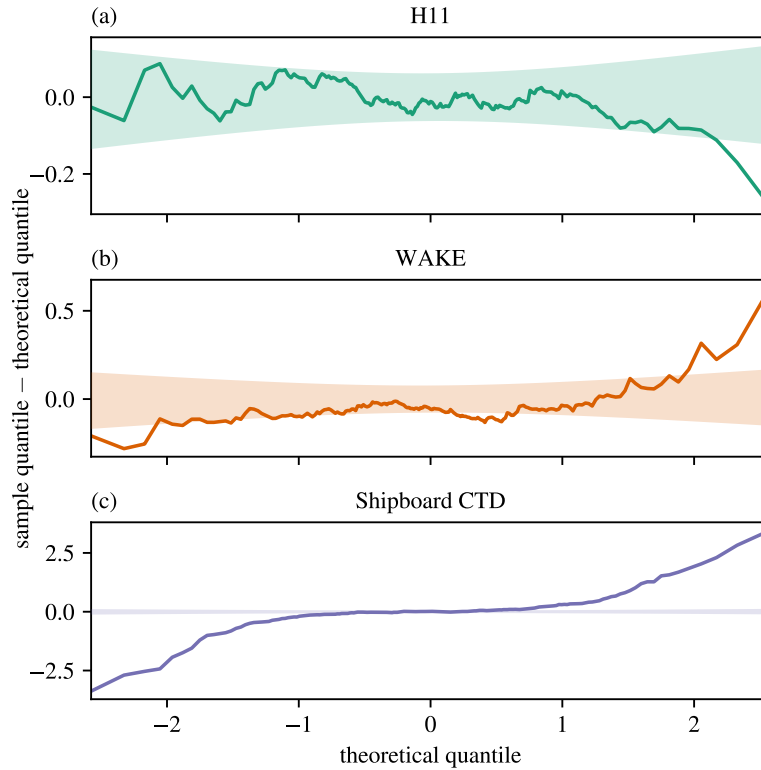
Figure 3.4: Difference between the sample quantile and the corresponding standard Gaussian theoretical quantile ($q_{\text{sample}} - q_{\text{theory}}$) plotted against the theoretical quantile (q_{theory}) for inferred travel time or slowness anomaly using nearby Argo profiles only. Shown are sample quantiles from decorrelated and normalized travel time anomaly differences between estimates from Argo data and (a) H11 measurements and (b) WAKE measurements. The equivalent analysis is shown in (c) for slowness anomaly differences estimated from Argo floats and shipboard data. Two-sided 95% confidence intervals are indicated with light shading.

and 1491 T-wave pairs for the H11 time series and 9108 conventional samples and 1161 T-wave pairs for the WAKE time series. We estimate $\boldsymbol{x}$ from $\boldsymbol{a}$, $\boldsymbol{b}$, or their combination $\boldsymbol{y}$. In the final subsection of this section, we estimate spatial patterns of the trend and time-mean offset using all conventional observations from 135°E to 170°E, 15°N to 45°N with the same constraints for the time periods. This allows us to contextualize the observations along the T-wave paths.

Consistency between seismic and conventional data

To test the statistical consistency between the Argo data and seismic observations, we estimate the travel time anomalies at the times of all earthquakes that produce a usable T-wave measurement. The vector $\boldsymbol{x}$ thus denotes the collection of these

travel time anomalies, and we estimate it from all Argo data collected in $\boldsymbol{a}$ as well as from all seismic data collected in $\boldsymbol{b}$. We obtain $\tilde{\boldsymbol{x}}_a$, $\tilde{\boldsymbol{x}}_b$, and the posterior covariances $\mathbf{P}_a$ and $\mathbf{P}_b$ from (3.7) and (3.8), and we calculate the difference between the two measurements as $\boldsymbol{\Delta} = \mathbf{D}(\tilde{\boldsymbol{x}}_a - \tilde{\boldsymbol{x}}_b)$. Under the null hypothesis that the two estimates are consistent, $\boldsymbol{\Delta}$ has a Gaussian distribution centered at zero with covariance $\mathbf{P}_\Delta = \mathbf{D}(2\mathbf{R}_{xx} - \mathbf{P}_a - \mathbf{P}_b - \mathbf{R}_\Delta - \mathbf{R}_\Delta^\mathrm{T})\mathbf{D}^\mathrm{T}$, where $\mathbf{R}_\Delta = \mathbf{R}_{xa}\mathbf{R}_{aa}^{-1}\mathbf{R}_{ab}\mathbf{R}_{bb}^{-1}\mathbf{R}_{xb}^\mathrm{T}$. Using a Cholesky decomposition $\mathbf{P}_\Delta^{-1} = \mathbf{LL}^\mathrm{T}$, we can decorrelate and normalize $\boldsymbol{\Delta}$ as $\boldsymbol{z} = \mathbf{L}^\mathrm{T}\boldsymbol{\Delta}$. Under the consistency hypothesis, the elements of $\boldsymbol{z}$ are then independent samples of a standard Gaussian. Given that 96 and 94% of these elements fall between -2 and 2 for H11 and WAKE, respectively, and the quantile differences of these estimates with those from the standard Gaussian generally fall into a 95% confidence interval (Fig. 4.7ab), the T-wave and Argo estimates are statistically consistent.For H11, 98% of the sample quantiles fall within the 95% uncertainty range of the theoretical quantiles. Although this fraction is only 72% for WAKE, the departures are small and largely confined to the tails of the distribution. A covariance that takes the statistical inhomogeneity between the Kuroshio Extension meanders and gyre interior into account appears to be needed for an improved match.

A similar consistency test between shipboard CTD casts and Argo data shows a greater degree of mismatch. Now, $\boldsymbol{x}$ denotes the collection of slowness anomalies at shipboard CTD profile locations that fall into the selected region between 02-25-2001 and 31-07-2021, where the start date is set by the first available Argo profile in this region. This procedure selects 1223 shipboard CTD casts and 7555 Argo profiles. The slowness anomaly calculated from nearby Argo measurements is $\boldsymbol{a}$, and the slowness anomalies calculated directly from shipboard CTD casts is $\boldsymbol{b}$. Performing the same consistency analysis as above reveals that the decorrelated and normalized difference $\boldsymbol{\Delta} = \mathbf{D}(\tilde{\boldsymbol{x}}_a - \tilde{\boldsymbol{x}}_b)$ shows significant deviations from a standard Gaussian (Fig. 4.7c). Although the center of the distribution is nearly Gaussian, the tails are too heavy, suggesting that the shipboard CTD profiles produce larger slowness anomalies than expected from the Argo-based predictions. We suspect that this is caused primarily by a bias in the shipboard sampling locations. Many of the profiles targeted the intense variability in the Kuroshio Extension and the mesoscale eddies shed by it. This targeted sampling increases the likelihood of finding a strong anomaly in the shipboard CTD data relative to a set of randomly chosen locations and times. That said, the non-Gaussian statistics of mesoscale eddies may also contribute to the heavy tails. Temperature anomalies below 2 km that are captured by full-depth shipboard CTD casts but not Argo profiles make negligible contributions to

slowness anomalies and cannot explain the heavy tails. Despite these results, we treat the shipboard data as if it were drawn from a random Gaussian distribution for the calculations below, and we leave more realistic considerations for future work.

Path-mean temperature anomalies

We now estimate time series of temperature anomalies averaged along a T-wave path from the Japan Trench to Wake Island (Fig. 3.1). We choose paths that are well-sampled by T waves, $\theta = 316.5°$ for H11 and $\theta = 317.1°$ for WAKE. The vector x contains the stochastic (with a 10-day spacing), trend, and seasonal components of the path-averaged slowness anomalies, and we estimate it from the set of conventional observations a, from the seismic observations b, or from their combination y.

The time series constructed from conventional and seismic data are consistent with one another, but the uncertainty is reduced substantially if the seismic data is used (Fig. 3.5). The uncertainty reduction is largest after the M 9.1 Tōhoku earthquake on 11-03-2011, when abundant aftershocks start providing tight seismic constraints. The contributions from the trend and seasonality are comparably well-constrained, and the uncertainty throughout the time series is dominated by the stochastic component. For H11, the conventional data reduces its prior variance by 45%, the seismic data reduces it by 80%, and the combination achieves a reduction by 83%. For WAKE, these numbers are 49%, 69%, and 74%, respectively. This demonstrates the ability of the seismic data to efficiently constrain range-averaged temperature anomalies by providing an intrinsically integrating measurement, whereas the conventional data suffers from insufficient coverage to resolve mesoscale anomalies.

Noticeable differences between the estimates based on the conventional and seismic data occur, for example, in late 2018 for both H11 and WAKE (Fig. 3.5a,c). The seismic data capture a sizable warm anomaly that is missed by the conventional data. Comparing maps of the temperature anomalies inferred from conventional data with sea level anomalies from satellite altimetry on 24-11-2018 sheds some light on these differences (Fig. 3.1b,c). Although the conventional data captures a warm anomaly in the Kuroshio Extension just south of the path, it misses a number of warm anomalies presumably associated with sea level highs, one off the coast of Japan and a number of them along the southeast portion of the path. The seismic data, intrinsically averaging, capture these anomalies.

Although our estimate based on conventional data generally agrees with that by
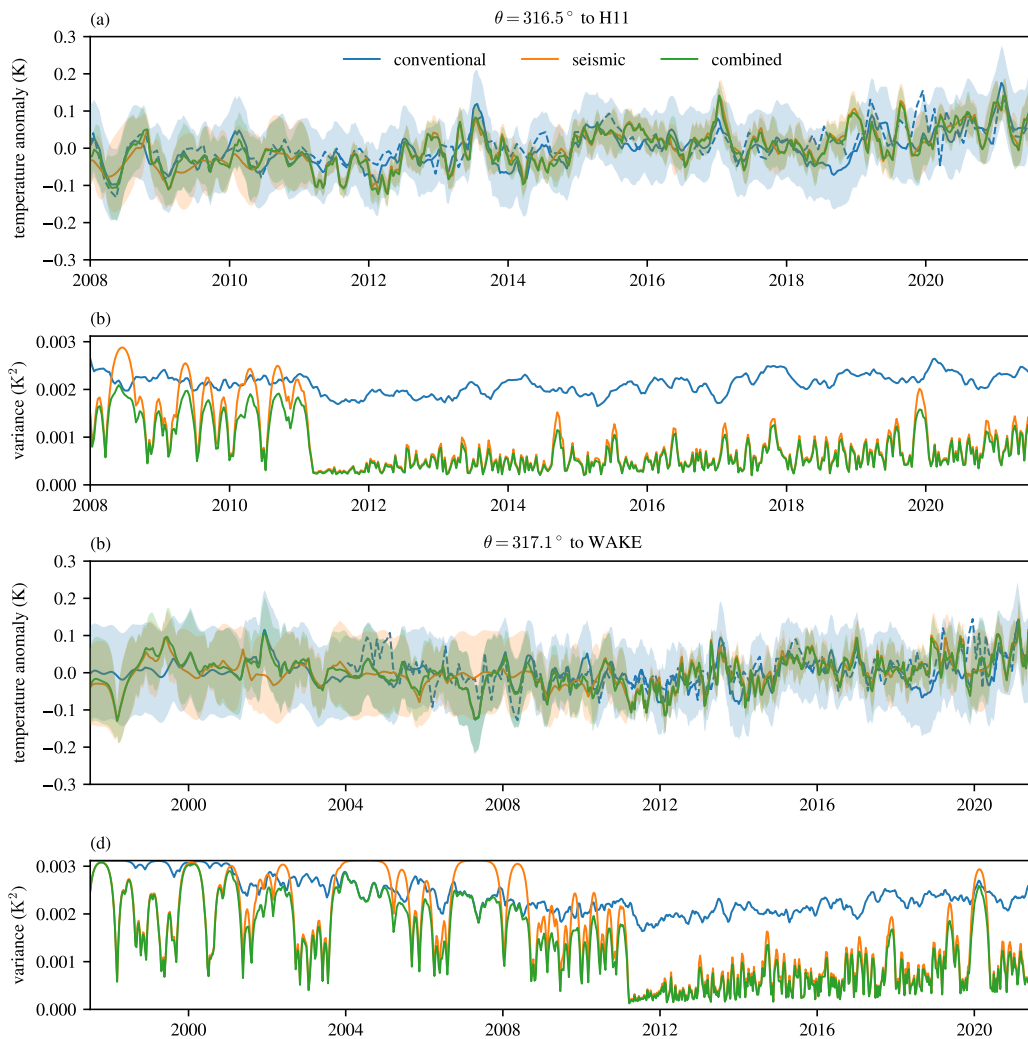
Figure 3.5: Path-averaged temperature anomalies and uncertainties inferred from conventional and seismic measurements. (a,c) Time series of temperature anomalies at azimuths $\theta = 316.5°$ and $317.1°$ as inferred conventional data (Argo and shipboard CTD profiles), T waves received at either H11 and WAKE, and a combination of the two types of measurement. Shading shows the $\pm 2\sigma$ uncertainty range. The dashed blue curve is inferred from the previously published Argo product by RG. (b,d) Time series of the pointwise posterior variance of the stochastic component of the three estimates. The upper bound of the vertical axis corresponds to the prior. All estimates are shown on a regular 10-day grid.
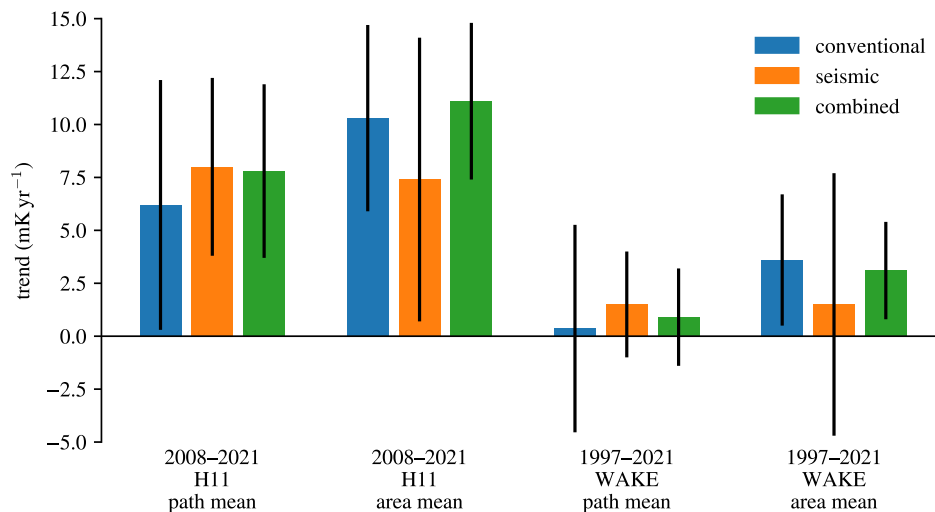
Figure 3.6: Trends of either path- or area-averaged temperatures as inferred from conventional data, seismic data, or a combination. The error bars show the $\pm 2\sigma$ uncertainty range.

Roemmich and Gilson (2009, RG), there are noticeable differences, especially early on (2004 to 2006) but also in late 2019 (Fig. 3.5a,c). A comparison between maps of the RG estimate, our estimate, and sea level anomalies for 23-11-2019, one such time of large disagreement, reveals that the RG estimate has a widespread positive anomaly over the northwest portion of the path, missing a strong cold anomaly in between that is present in our estimate and the sea level (Fig. 3.1a–c). The seismic data provide a strong constraint at this time that excludes the possibility of a widespread warm anomaly.

The seismic data also helps better constrain the linear trends during these two time periods (Fig. 3.6). Compared to estimates based only on conventional data, the posterior variance of the trend estimate is reduced by 53% for H11 and 78% for WAKE. The best estimates based on the combination of conventional and seismic data are 7.6 ± 4.7 mK yr^{-1} for the H11 time period and 0.9 ± 2.7 mK yr^{-1} for the WAKE time period. The insignificance of the trend over the longer WAKE time period suggests that the significant trend over the H11 time period was either part of multidecadal variability or the onset of a forced trend around 2008. A longer time series (in both directions) is needed to distinguish between these two possibilities. There is not a big change between the conventional and combined estimates for the WAKE period, likely due to sufficient samples in the early 2000 (Fig. 3.3). We also note that there is an irreducible component to the trend uncertainty in the presence

of stochastic anomalies. Perfect sampling would reduce the posterior variance of the trend estimate by 56% for H11 and 87% for WAKE.

Area-mean temperature anomalies

To obtain more representative estimates of the temperature variability in the Kuroshio Extension region than from the single paths analyzed in the previous section, we now estimate area-mean temperature anomalies for the areas defined at the beginning of the section (Fig. 3.1a,d). The vector x now includes the area-mean slowness anomalies due to the stochastic, trend, and seasonal components.

The time series of these area means are somewhat less well-constrained than the path means, but the seismic data again contributes substantially to the uncertainty reduction (Fig. 3.7). Relative to the prior, the posterior variance of the stochastic component in the H11 time series is reduced by 30% by the conventional data, 39% by the seismic data, and 50% by the combination. These reductions are 23%, 25%, and 37%, respectively, for the WAKE time series. The uncertainty reduction by the two data sets by themselves is thus comparable, and the two are highly complementary, leading to a substantial further reduction when combined. Broadly, this is because the conventional data do not resolve mesoscale eddies, whereas the seismic data provide integral constraints that capture these mesoscale anomalies but cannot distinguish between anomalies that are close to the receiver, which contribute little to the area mean, and anomalies that are farther out, which contribute more substantially. There is again a noticeable drop in the uncertainty in 2011, when T-wave constraints become more abundant. The conventional data show a decline in the uncertainty as Argo data becomes available over the course of the 2000s, making pre-Argo constraints from WAKE particularly valuable.

The time series show a steady warming from 2008 to 2021, whereas there is no substantial trend before 2008 (Fig. 3.7). This is reflected in the trend estimates, which are 11.8 ± 5.0 mK yr^{-1} for the H11 time period and 2.5 ± 3.2 mK yr^{-1} for the WAKE time period (Fig. 3.6). For H11, the posterior variance of this trend estimate is reduced relative to the prior by 82% by the conventional data, 61% by the seismic data, and 83% by the combination. How much additional observations could further improve these estimates is limited by the indeterminacy between the trend and stochastic components. Perfect observations would reduce the posterior variance by 94%. For WAKE, the variance reductions are 91%, 86%, and 93%, respectively, and the maximum possible reduction is 99%.
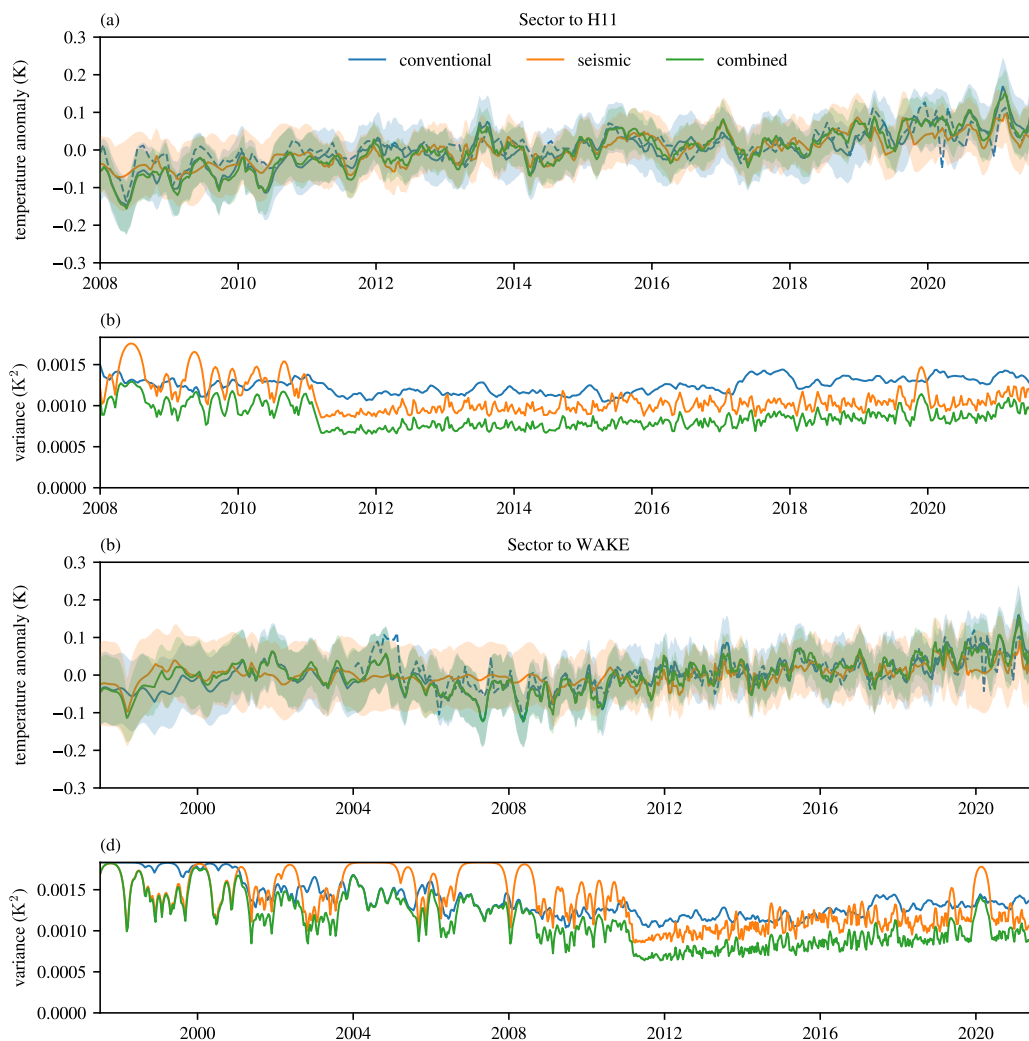
Figure 3.7: Area-averaged temperature anomalies and uncertainties inferred from conventional and seismic measurements. (a,c) Time series of area-averaged temperature anomalies as inferred conventional data (Argo and shipboard CTD profiles), T waves received at either H11 and WAKE, and a combination of the two types of measurement. Shading shows the $\pm 2\sigma$ uncertainty range. The dashed blue curve is inferred from the previously published Argo product by RG. (b,d) Time series of the pointwise posterior variance of the stochastic component of the three estimates. The upper bound of the vertical axis corresponds to the prior. All estimates are shown on a regular 10-day grid.

Mapped trends

To better understand the trends in the time series of path- and area-averaged temperatures, we use the conventional data to map out the local trends during the H11 (2008 to 2021) and WAKE (1997 to 2021) time periods for a wider region centered on the T-wave path (Fig. 3.8). We estimate the pointwise trend as well as the time-mean offset from the WOA reference from 15°N to 45°N and 135°E to 170°E. We estimate these trends and offsets latitude by latitude, using all profile data that fall within ±3° of latitude, resulting in 10,000 to 30,000 measurements per estimate.

The time-mean offset is concentrated along the path of the Kuroshio Extension at about 35°N (Fig. 3.8c,g). We suspect that this offset appears because we apply less smoothing and thus allow for sharper gradients across the Kuroshio Extension front than the WOA reference. The offset is substantially better constrained for 2008 to 2021 than 1997 to 2021, due principally to the abundance of Argo profiles starting in the mid-2000s.

The trend maps show concentrated warming in two patches along the path of the Kuroshio Extension and cooling in the location of an intermittent meander upstream of the Izu Ridge (Fig. 3.8a,e). The strongest warming around 35°N, 143°E reaches up to 53 ± 20 mK yr^{-1} for 2008 to 2021 and is reduced to 35 ± 15 mK yr^{-1} for 1997 to 2021. There is an indication of broad cooling south of the Kuroshio Extension in 1997 to 2021 that becomes less pronounced and, in part, tips to warming in 2008 to 2021, but the uncertainty is large.

3.5   Discussion

The patterns in the trend maps (Fig. 3.8) strongly suggest that a large component of the trends in the time series (Fig. 3.5, 3.6, 3.7) stems from changes in the Kuroshio Current and Extension. We begin by discussing the patch of strong cooling south of Japan, which coincides with the location of a recurring large meander of the Kuroshio Current. The current is known to switch between a state with a large meander and a state in which it follows the coastline in a straight path (e.g., Kawabe, 1995; Qiu and Chen, 2021). The cooling is likely caused by the prevalence of the large-meander state in the later part of the time series. A large meander emerged in August 2017 and has persisted longer than any other on record (Qiu et al., 2023). Similarly, and relevant for the time series discussed above, the patches with the strongest warming coincide with the locations of standing meanders of the Kuroshio Extension. These meanders are less stable than the upstream large meander, but
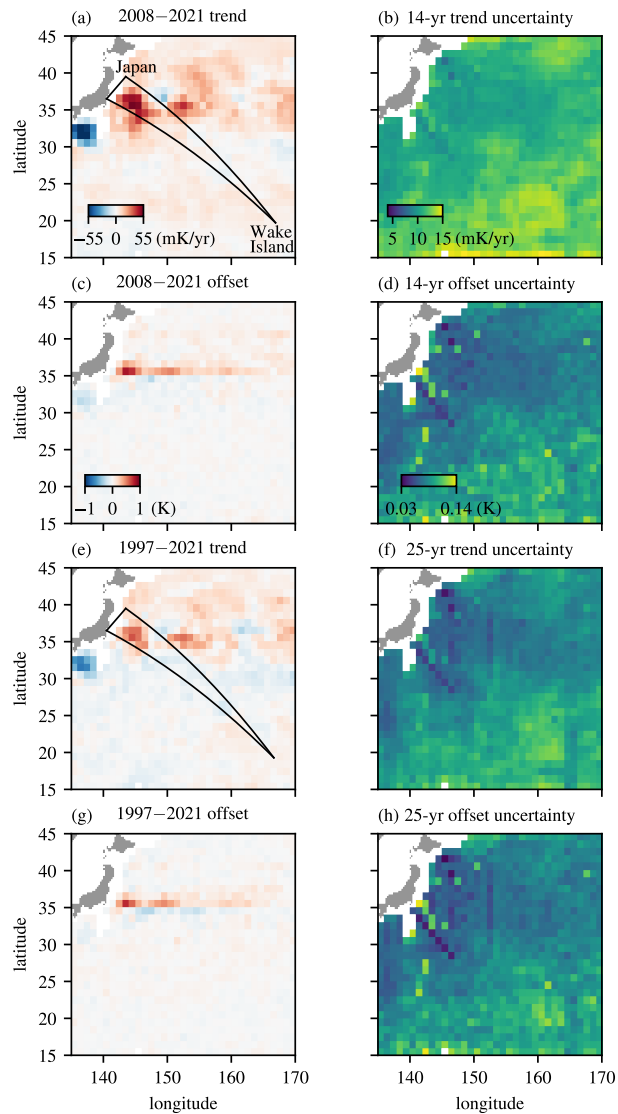
Figure 3.8: Inferred trends and time-mean offsets from the WOA reference. These maps are inferred from conventional data only, with the same weighted averages as used throughout. The trends and offsets are estimated for the same time periods as seismic data was available from H11 (2008 to 2021) and WAKE (1997 to 2021). The left column shows the posterior mean, and the right column shows the posterior uncertainty (1σ).

they are also known to exhibit decadal modulations between a stable and an unstable dynamic state (e.g., Qiu et al., 2020). The phase change between these two states has been linked to the basin-wide wind stress curl variability associated with the Pacific Decadal Oscillations (Mantua et al., 1997), although a clear correspondence between the PDO and our time series is not apparent. We suspect that the strong warming in this region over the time periods analyzed is part of the decadal variability of the Kuroshio Extension, although the data do not exclude the possibility of a forced component to this signal in the later part of the time series. Subtropical mode waters like that in this region have taken up a large fraction of the excess heat globally (e.g., Li et al., 2023). Longer observational records or ensembles of eddy-resolving climate simulations are needed to disentangle these possibilities.

Here we do not combine H11 and WAKE data to estimate area-mean temperatures, yet this should be feasible given the generality of our estimation procedure. The two stations are 50 km apart, so the T waves received at the two stations sample somewhat different parts of the ocean (Peng et al., 2024), Combining the two would therefore yield an improved estimate, and it would help to more quantitatively compare the H11 and WAKE time series from 2008 to 2021.

Given our demonstration that the seismic and conventional measurements are consistent and complementary, combining them in more sophisticated estimation schemes such as the ECCO state estimate is likely to lead to improved estimates. This will involve the development of "integral" constraints beyond current ECCO's point-wise only constraints. It also encourages further expansion of the seismic data set. The current measurement procedure can be applied more widely to all CTBTO hydrophones and to T waves arriving from all azimuths, which would provide near-global constraints. Further extensions back in time using digital and potentially analog records from near-shore seismic stations or long-term hydrophone records that are not publicly available at present would provide further valuable constraints on the pre-Argo era. Future expansions of the network of hydrophone stations and the use of vertical arrays would improve constraints on future subsurface warming, which is projected to accelerate considerably (e.g., Cheng et al., 2022). In addition, better understanding of the excitation and propagation of T waves is likely to allow for improved measurements and representation.

Previous statistical estimation using Argo data has provided valuable information on global heat uptake and regional trends. The RG estimate serves as one of the more popular gridded Argo products and is based on a comparably simple mapping

procedure. Recent work has applied more sophisticated statistical methods to arrive at better estimates and quantify their uncertainty (Kuusela and Stein, 2018; Yarger et al., 2022; Baugh and McKinnon, 2022), especially by allowing the data to inform the statistical model. The estimation procedure employed here is similarly based on a prior covariance informed by observations of mesoscale eddies from satellite altimetry that is then calibrated using Argo data, and it assign a prior covariance with a short spatial correlation scale to the trend to capture shifts and transport changes of the Kuroshio Extension. This improves on the assumptions employed in Peng et al. (2024), but the Gaussian, stationary, and separable prior covariance is still too idealized to capture the true variability. Correlation scales vary significantly with latitude, and the variance of mesoscale eddies varies substantially between major current regions and the interior of gyres. Future works might take advantage of the correlation between seismically sampled temperature anomalies and sea level anomalies (Peng et al., 2024) to construct a more realistic nonstationary covariance field from sea level statistics. A more realistic covariance might also explicitly allow for decadal and multidecadal variability to distinguish it from the forced signal. In the tropical ocean, the covariance should further account for equatorial waves (Wu et al., 2020; Callies et al., 2023; Wu et al., 2023).

3.6   Conclusions

Travel time changes of seismically generated sound waves can be combined with conventional in situ data to better constrain the variability of subsurface temperature. We demonstrate with data from the Kuroshio Extension region that the seismic and conventional data are statistically consistent, building further confidence in the ability of the seismic data to provide tight constraints on oceanic variability. We also show that combining the seismic and conventional data substantially reduces the uncertainty of spatially averaged temperature anomalies. This quantification of the complementary value of the seismic data establishes the foundation for future work to assimilate the seismic data to help better constrain regional and global integrals. Although seismic data are valuable primarily for estimating spatial averages, the approach can be further advanced by expanding the network of T-wave receivers or exploring the historical record further back in time.

Chapter 4

YANAI WAVES IN THE DEEP EAST INDIAN OCEAN OBSERVED WITH SEISMIC TOMOGRAPHY

4.1 Abstract

Near-surface measurements of meridional velocity suggest that wind forcing excites waves in the biweekly band in the equatorial Indian Ocean. However, the characteristics of these waves in the deep ocean are poorly constrained, and it is unclear how well models capture the deep variability. In this work, seismically generated sound waves (so-called "T waves") are used to infer temperature variations due to biweekly oscillations of a few vertical modes in the deep East Indian Ocean. These T waves are generated by earthquakes off Sumatra and received by a hydrophone station off Diego Garcia. The comparison between T wave data and model outputs shows good consistency in biweekly variations dominated by the first three modes. Regression analysis indicates that the origin of these variations is westward-propagating Yanai waves. That said, the biweekly variance differs by up to a factor of two between the data and the models. A similar degree of discrepancy appears in the comparison between the models and deep-mooring measurements. These results highlight the potential of using T wave data to study biweekly Yanai waves in the deep equatorial ocean and to calibrate numerical simulations of these waves.

4.2 Introduction

Approximately biweekly oscillations make a prominent contribution to the variability of the tropical Indian Ocean and potentially affect the mean circulation (Ogata et al., 2017). This variability has been identified in the meridional velocity captured by near-surface current meters on equatorial moorings (Reppin et al., 1999; Sengupta, 2004; Masumoto et al., 2005) as well as in satellite-derived sea level and surface salinity anomalies (Arzeno et al., 2020; Roman-Stork et al., 2020; Subrahmanyam et al., 2018). Both in situ measurements and remote-sensing observations consistently exhibit the meridional structure of mixed Rossby–gravity or Yanai waves (Pujiana and McPhaden, 2021). These measurements thus suggest that wind stress variations preferentially excite waves in the biweekly band where they project onto the dispersion curve of Yanai waves (Fig. 4.1a).

Observations have captured the space and time characteristics of Yanai waves near

the surface and to a lesser extent in the deep ocean as well (Sengupta, 2004; Pujiana and McPhaden, 2021). Mooring data show largest biweekly variance near the surface, weakening significantly below 150 m depth; these data derive from just a few locations and do not adequately describe the full scope of the variability. Models indicate the importance of vertical propagation and bottom reflections of Yanai waves in setting the zonal and vertical distribution of biweekly variability in the Indian Ocean (Miyama et al., 2006; Ogata et al., 2008). In particular, Miyama et al. (2006) used a continuously stratified linear model model together with ray theory to demonstrate eastward propagation of Yanai wave energy to the deep ocean and reflection from the seafloor. Downward-propagating wave packets transmit energy below the near-surface pycnocline and provide the main sink of biweekly surface energy, while upward-propagating packets arising from bottom reflections approach the surface east of the forcing region and become increasingly important in enhancing the surface energy. Both these processes are sensitive to the stratification and vertical mixing. Furthermore, Miyama et al. (2006) found that the eastward ray path can be blocked by a ridge near 75°E in a moderate-resolution (~0.33°) ocean general circulation model (OGCM), which reduced near-surface variations in the eastern basin. This model also disagreed with the linear model on the zonal gradient of biweekly variability in the central basin and the phase of biweekly variability in the eastern basin.

As such, OGCMs can provide valuable insights, but the degree to which they capture the deep variability of the real ocean remains unclear, largely because in situ measurements are too limited in the deep ocean to better assess the model results. Using an OGCM with higher spatial resolution (~0.1°), Ogata et al. (2008) reproduced the downward ray propagation effect and showed that wind forcing around 83°E produces energetic biweekly variability at 4000 m at 0°, 93°E, the site of a deep moored current meter. They found qualitative consistency between the OGCM output and the observed current variability in the biweekly band, but it remains uncertain what contributes to the quantitative discrepancies in both magnitude and phase. Nagura and McPhaden (2023) showed a remarkable consistency between the observations reported by Pujiana and McPhaden (2021) and the simulated biweekly variability in both amplitude and phase in the upper 200 m at 0°, 80.5°E, but the variability in the deep ocean was not investigated.

Agreement between near-surface observations and model results does not necessarily imply that the models capture the deep variability equally well, because the
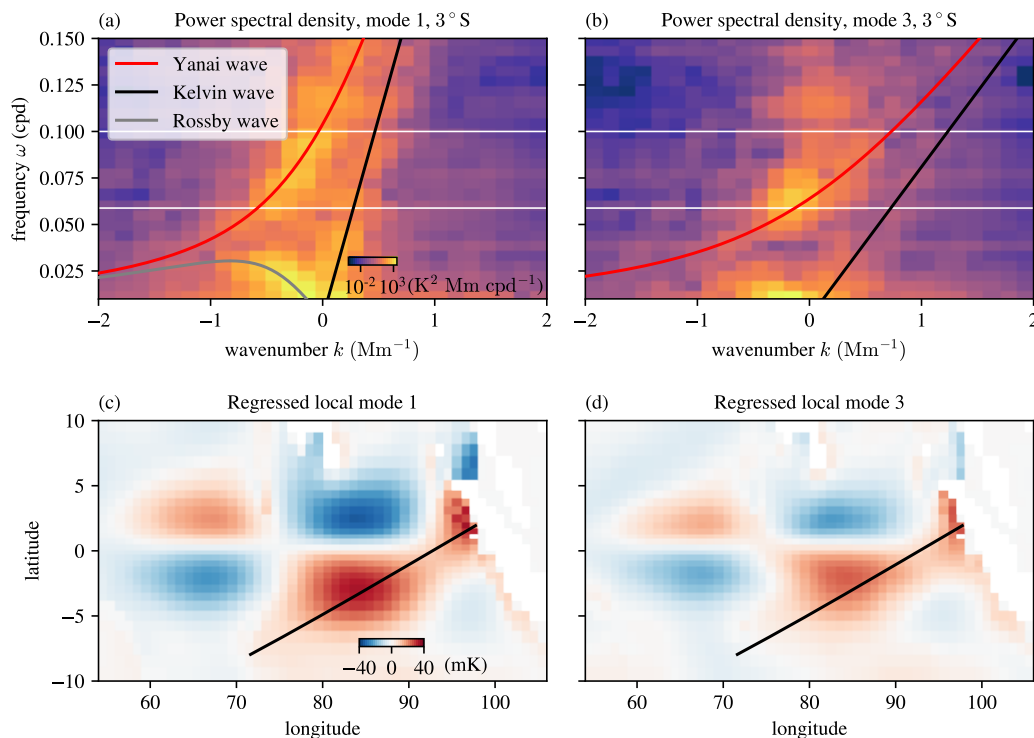
Figure 4.1: Yanai waves sampled by seismically generated T waves propagating from Nias Island to the hydrophone station H08 off Diego Garcia. (a,b) Frequency–wavenumber spectra of temperature anomalies projected onto the vertical mode 1 and vertical mode 3 at 3°S from ECCO output, together with the corresponding dispersion curves for the equatorial Yanai, Kelvin, and Rossby waves. The spectral density is shown on a logarithmic scale. White lines indicate the biweekly band between 10 to 17 days. (c,d) Regression of local mode 1 and mode 3 onto the their averages over the T wave path from Nias Island to Diego Garcia (black). These mode coefficients are filtered between 10 to 17 days.

models might not accurately capture the wave dynamics in the deep ocean. The propagation of waves into the deep ocean is sensitive to stratification, which in models can drift away from the observed stratification. The waves are attenuated by parameterized vertical mixing, which is poorly constrained observationally. The interaction with complicated topography requires high resolution and can produce errors in wave bottom reflections. Furthermore, regional simulations require boundary conditions that are imperfectly known, producing errors that could propagate into the region of interest. Better observational constraints on the deep biweekly variability could therefore help improve the models and improve our understanding of the processes involved.

Here, we show that biweekly Yanai waves in the deep equatorial Indian Ocean

are sampled by seismically generated sound waves that traverse the southeastern part of the Yanai wave pattern (Fig. 4.1c,d). Natural earthquakes release their energy first as *P/S* waves, which can be converted to sound waves in the ocean at the seafloor (Okal, 2008). The sound waves, so-called *T* waves, propagate more rapidly in warmer water, so changes in wave travel times capture changes in the temperature of the deep ocean traversed by waves (Wu et al., 2020). The vertical structure of these temperature anomalies can be inferred by measuring changes in travel time at different acoustic frequencies, at which the waves are sensitive to different parts of the water column (Callies et al., 2023). In 2005, abundant small earthquakes off Sumatra generated frequent *T* waves received at the CTBTO (Comprehensive Nuclear-Test-Ban Treaty Organization) hydrophone station H08 (Wu et al., 2023), so that intraseasonal temperature variations can be resolved. Naturally integrating along their path and thus averaging out small-scale fluctuations, the seismic waves complement point measurements from Argo floats and moorings that alias such small-scale fluctuations (cf., Munk and Wunsch, 1979). Thus, these acoustic measurements provide an opportunity to better constrain the large-scale biweekly variability of the deep equatorial Indian Ocean, including some of its vertical structure.

Although models may not fully capture all processes involved in the Yanai wave propagation, the interpretation of *T* wave measurements also involves uncertainties that must be accounted for in data–model comparisons. Changes in *T* wave travel time are related to changes in temperature using a numerically calculated sensitivity kernel (Wu et al., 2020, 2023). This calculation makes a number of assumptions. It only models *T* wave propagation along the geodesic path, while in reality the problem is three-dimensional. Furthermore, the *T* wave excitation and propagation depends to some degree on the sediment distribution, which is not well constrained observationally. Therefore, discrepancies between *T* wave data and ocean models can arise from errors in the kernel calculation, the ocean models, or both. To distinguish between these possibilities, we also compare the models with velocity data from deep moorings on the equator.

In our comparison, we find generally good consistency between *T* wave data and model predictions in both the magnitude and phase of biweekly variations. The modeled *T* wave travel time anomalies are dominated by the first three baroclinic modes (cf., Miyama et al., 2006), and regression analysis demonstrates their horizontal Yanai wave structure. Despite this general consistency, however, the biweekly

variance differs by up to a factor of two between the models and observations. A similar degree of disagreement is found in the comparison between models and deep mooring measurements, precluding the conclusion that the model–data misfit can be ascribed to the T wave observations alone. More broadly, our results demonstrate the potential of T wave measurements in studying Yanai waves in the deep equatorial ocean and to calibrate the representation of these waves in numerical models.

4.3   Data and models

Seismic and mooring data

We use seismic data from 11,479 repeating earthquake pairs arising from 3,457 earthquakes that occurred near Nias Island off Sumatra from 2005 to 2018 (Callies et al., 2023; Wu et al., 2023). We measure T wave arrival time changes at the CTBTO hydrophone station H08 near Diego Garcia at the acoustic frequencies 2.0, 3.0, and 4.0 Hz. For each frequency, we apply a Gaussian filter with width 0.5 Hz centered on that frequency before calculating the correlation function between the T-wave arrivals of an earthquake pair, as described in Wu et al. (2023). We describe in the next section the inversion framework to obtain ocean temperature time series from measured arrival time differences between repeating earthquakes.

We further use observations of meridional velocity from current meters mounted on the INCOIS (Indian National Centre for Ocean Information Services) moorings at 77°E, 83°E, and 93°E along the equator (Jain et al., 2021), providing ten, twelve, and nine time segments from 2000 to 2020, respectively. The sampling interval ranges from 30 min to 1 h. We compute daily averages if more than two-thirds of the data are available in a day, and fill daylong gaps in the resulting time series by linear interpolation. We keep the time series segments that are longer than 250 days.

Ocean circulation and wave propagation models

We compare the data to a regional high-resolution model as well as a coarser global state estimate. The global model is the ECCO (Estimating the Circulation and Climate of the Ocean) v4r4 state estimate (ECCO Consortium et al., 2021; Forget et al., 2015), whose solution minimizes a weighted quadratic sum of differences between the MITgcm and data from Argo floats, satellite altimetry, equatorial mooring arrays, and most other previously available oceanographic data (not the T wave data). This is done using the adjoint method (Wunsch and Heimbach, 2013; Wunsch et al., 2009). It has a nominal 1° horizontal grid spacing and 50 z levels for the vertical discretization; the model output spans January 1992 to December 2017 in a daily

resolution. The external forcing uses 6-hourly ERA-Interim re-analysis fields (Dee et al., 2011) for freshwater flux, wind stress and buoyancy flux, which are adjustable in the state estimation. The regional model is the ocean general circulation model for the Earth Simulator (OFES; Masumoto et al., 2004; Sasaki et al., 2020; Nagura and McPhaden, 2023). The model domain is 20°S to 20°N and 35°E to 115°E, and the horizontal grid spacing is 0.1° in longitude and latitude. The model was forced by the Japanese 55-year atmospheric reanalysis (JRA55-do; Tsujino et al., 2018). We use daily averages of potential temperature and salinity in 2005 to compare with the T wave data and meridional velocity output from 2000 to 2019 to compare with the mooring observations.

T wave sensitivity kernels at different acoustic frequencies come from SPECFEM2D wave propagation simulations (Wu et al., 2020, 2023). These simulations use the mean hydrography from ECCO and a statistical solid-earth model. We evaluate uncertainties in these kernels by comparing two versions, with or without a sediment layer. We expect the version with sediment to be more realistic, but the thickness and properties of the sediment is not very well constrained. The sediment thickness is prescribed based on GlobSed (version 3; Straume et al., 2019).

4.4 Methods

Linear wave modes in the deep equatorial ocean

To relate T wave observations to the linear theory of Yanai waves, we decompose the temperature anomaly field $T'(x, y, z, t)$ into vertical modes:

$$T'(x, y, z, t) = \sum_{n=1}^{\infty} T'_n(x, y, t)\, N^2(z)\, G_n(z), \tag{4.1}$$

where $T'_n(x, y, t)$ is the nth mode coefficient field, $N^2(z)$ the stratification averaged in space and time, and $G_n(z)$ the nth local vertical mode satisfying

$$\frac{\partial^2 G_n}{\partial z^2} + \frac{N^2}{c_n^2} G_n = 0, \tag{4.2}$$

where c_n is the eigenspeed of mode n (e.g., Gill, 2006). We assume flat-bottom and rigid-lid boundary conditions,

$$G_n = 0 \quad \text{at} \quad z = 0 \quad \text{and} \quad z = -H, \tag{4.3}$$

and the modes satisfy local orthogonality:

$$\int_{-H}^{0} N^2 G_n G_m \, \mathrm{d}z = \delta_{nm} N_0^{-2} H, \tag{4.4}$$

where we set the water depth H to 5375 m, and $N_0 = 10^{-3}$ s^{-1} is a reference buoyancy frequency. This normalization ensures that the mode coefficients T'_n have units of temperature. Multiplying both sides of (4.1) by G_m and integrating over the water column gives:

$$T'_m(x, y, t) = \frac{N_0^2}{H} \int_{-H}^{0} T'(x, y, z, t) \, G_m(z) \, \mathrm{d}z, \tag{4.5}$$

where we have applied the orthogonality condition (4.4). Assuming a rigid lid, a flat bottom, a horizontally uniform stratification, and perturbations that are sufficiently small to allow for a linearization, each $T'_n(x, y, t)$ follows linear shallow-water dynamics. Bathymetry and horizontal variations in N^2 require locally defined modes, whose dynamics are coupled (e.g., Kelly, 2016). If this coupling is sufficiently weak and the perturbations are far from continental boundaries, we can further project the baroclinic modes $T'_n(x, y, t)$ onto meridional wave modes:

$$T'_n(x, y, t) = \frac{1}{2\pi} \int_{-\infty}^{+\infty} \sum_{m=-1}^{\infty} \sum_{\omega=\omega(k)} \tilde{T}_{nm}(k, y, \omega) \, e^{i(kx-\omega t)} \, \mathrm{d}k \tag{4.6}$$

with the dispersion relation (e.g., Gill, 2006):

$$\left(\frac{\omega}{c_n}\right)^2 - k^2 - \beta\frac{k}{\omega} = (2m + 1)\frac{\beta}{c_n}. \tag{4.7}$$

The special case $m = 0$ corresponds to Yanai waves. Forced by large-scale wind patterns, they are excited preferably around the biweekly frequency (Fig. 4.1a,b) and have a meridional structure that is symmetric for meridional velocity and anti-symmetric for temperature (Fig. 4.1c,d; explained in detail below). Symmetric signals have their largest amplitude along the equator, while anti-symmetric signals peak around one equatorial deformation radius $\ell_n = (c_n/\beta)^{1/2}$ off the equator, which is about 3° in latitude for $n = 1$ (e.g., Gill, 2006). The path from Nias Island to H08 covers 1°N to 7°S, so T waves effectively sample the large-scale anti-symmetric temperature signals of biweekly Yanai waves (Fig. 4.1c,d). Given that the acoustic travel time for the 2900 km distance is around 0.5 hour, these samples are practically instantaneous. This simple one-mode equatorial wave model has its limitation, of course, given that the real ocean has bathymetry and boundaries, but it captures key features of the modeled and observed variability that justifies classifying said variability as Yanai waves. We emphasize that the severe assumptions needed to arrive at the above dispersion relation are not made in the data–model comparison discussed below.
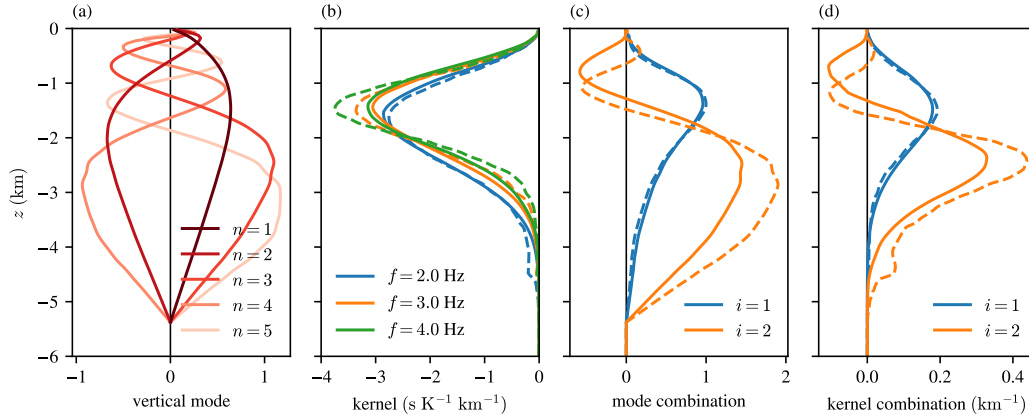
Figure 4.2: Baroclinic modes, sensitivity kernels, and their covarying combinations. (a) First five baroclinic modes $N_0^2 G_n(z)$. (b) Range-integrated sensitivity kernels $[K_j](z)$ for the three acoustic frequencies used in the measurements. (c) First two mode combinations covarying with kernel combinations, $N_0^2 \sum_n V_{ni} G_n(z)$ with $i = 1, 2$. (d) First two kernel combinations covarying with mode combinations, $\lambda_i^{-1} \sum_j U_{ji} [K_j](z)$ with $i = 1, 2$. The solid curves in (b–d) correspond to kernel calculations with sediments, and the dashed curves correspond to sediment-free kernel calculations. All calculations are based on the stratification from OFES. Only slight differences exist in modes 4 and 5 below 2000 m depth between OFES and ECCO.

Given these dominantly linear and large-scale dynamics of equatorial waves, ocean models forced by atmospheric reanalysis should capture the associated variability reasonably well. The simulation of high vertical modes becomes more challenging because they are affected by poorly constrained vertical mixing (Miyama et al., 2006). The representation of topographic mode coupling also requires sufficient numerical resolution to capture narrow topographic features and the interaction of Yanai waves with them.

We expect the variance of T_n' to decrease rapidly with n for high-order baroclinic modes because the surface forcing projects most strongly on low modes and because vertical mixing preferentially damps high modes (Miyama et al., 2006). Results from a linear continuously stratified model suggest that the first three modes dominate the biweekly variance (Miyama et al., 2006), and Nagura and McPhaden (2023) confirmed using OFES output that mode amplitudes at periods of 10 to 17 days decay significantly and remain weak for modes 5 to 15. Although near-surface observations are yet to disentangle relative dominance among different modes, these models can serve as a first guide. We therefore expect a truncation at mode 5 to be sufficient to capture the bulk of the biweekly Yanai wave propagation in the deep

ocean:

$$T'(x, y, z, t) \approx \sum_{n=1}^{5} T'_n(x, y, t) \, N^2(z) \, G_i(z). \qquad (4.8)$$

We calculate the stratification, baroclinic modes, and projections from both OFES and ECCO (Fig. 4.2a). We average the daily stratification over the transect in 2005. Despite slight differences in the stratification between the two models, the first three modes are virtually identical between the models. The differences are more noticeable in modes 4 and 5 and below 2000 m depth, but they remain slight. We do not expect these differences to substantially affect the comparison between the models and with the data, which are dominated by the temperature variability itself rather than differences in the modes.

Seismic sampling of barolinic modes

Sensitivity kernels are critical for a quantitative interpretation of T wave data and a quantitative comparison with model results (Wu et al., 2020; Callies et al., 2023; Wu et al., 2023). We express the T wave travel time anomaly $\tau'_j(t)$ at acoustic frequency f_j as an integral of the temperature anomaly field $T'(x, y, z, t)$ along a travel path $(x(r), y(r))$, with r ranging from 0 to R, multiplied by the sensitivity kernel $K_j(r, z)$:

$$\tau'_j(t) = \int_{-H}^{0} \int_{0}^{R} K_j(r, z) \, T'(r, z, t) \, dr \, dz \approx \int_{-H}^{0} [K_j](z) \, \overline{T'}(z, t) \, dz, \qquad (4.9)$$

where

$$[K_j](z) = \int_{0}^{R} K_j(r, z) \, dr \quad \text{and} \quad \overline{T'}(z, t) = \frac{1}{R} \int_{0}^{R} T'(r, z, t) \, dr \qquad (4.10)$$

are the range-integrated sensitivity kernel and range-averaged temperature anomaly, respectively. The approximation in (4.9) assumes that the range-dependence of $K_j(r, z)$ is weak, generally a reasonable assumption (Callies et al., 2023).

We use the sensitivity kernels K_j for the three frequencies $f_j = 2.0, \ 3.0,$ and 4.0 Hz (Fig. 4.2b; Wu et al., 2023; Callies et al., 2023). At all three frequencies, the strongest sensitivity is located between 1 and 2 km depth, yet the 2.0 Hz kernel exhibits noticeably more sensitivity below. Based on these vertical structures and those of the baroclinic modes (Fig. 4.2a), we expect that the travel time anomaly averaged over the three frequencies is most sensitive to the first two baroclinic modes, whereas the difference between the 4.0 and 2.0 Hz travel time anomalies should be most sensitive to baroclinic mode 3. The kernels computed using (less

realistic) simulations without sediment have a more marked frequency dependence. While this does not qualitatively change the following analysis, it does affect the quantitative comparison between the T wave data and the models.

To systematically extract information on the baroclinic modes from the travel time anomalies τ_j', we substitute (4.8) into (4.9), giving

$$\tau_j'(t) \approx \sum_{n=1}^{5} A_{jn}\overline{T_n'}(t), \quad \text{where} \quad A_{jn} = \int_{-H}^{0} [K_j](z)\, N^2(z)\, G_n(z)\, \mathrm{d}z. \qquad (4.11)$$

At each time, the travel time anomaly τ_j' is thus expressed as a linear combination of the range-averaged modal coefficients $\overline{T_n'}$. In matrix form, this reads

$$\boldsymbol{\tau}(t) = \mathbf{A}\boldsymbol{T}(t), \qquad (4.12)$$

where $\boldsymbol{\tau}$ and $\boldsymbol{T}$ collect the τ_j' and $\overline{T'}_n$ into vectors. The singular-value decomposition (SVD) $\mathbf{A} = \mathbf{U}\boldsymbol{\Lambda}\mathbf{V}^{\mathrm{T}}$ allows us to define

$$\boldsymbol{a}(t) = \boldsymbol{\Lambda}^{-1}\mathbf{U}^{\mathrm{T}}\boldsymbol{\tau}(t) = \mathbf{V}^{\mathrm{T}}\boldsymbol{T}(t). \qquad (4.13)$$

The elements of $\boldsymbol{a}$ are linear combinations of travel time anomalies that covary with linear combination of the (range-averaged) mode coefficients. We pay particular attention to the first two elements a_1 and a_2 because the singular values decrease rapidly in amplitude, which amplifies noise and makes the third element unreliable.

The matrix $\mathbf{A}$ depends on the mean stratification (directly and through the baroclinic modes) as well as on the sensitivity kernel. We therefore calculate four versions of this matrix and its SVD: with the stratification from either OFES or ECCO and with the sensitivity kernel from the calculation either with or without sediment.

Whether OFES or ECCO stratification is used has little impact on the SVD (Fig. 4.3). The first singular value λ_1 varies between 26 and 28 s K^{-1}, and a_1 corresponds approximately to a scaled average of the three travel time anomalies or a weighted mean temperature anomaly. As indicated by the right singular vectors, a_1 captures primarily the first two baroclinic modes, with the second mode making a smaller and opposing contribution. The sensitivity $\lambda_1^{-1} \sum_j U_{j1}[K_j](z)$ of a_1 peaks around 1.5 km depth and is one-signed (Fig. 4.2d). The corresponding normalized mode combination $N_0^2 \sum_n V_{n1} G_n(z)$ has a very similar vertical structure (Fig. 4.2c). These structures agree by construction up to a projection onto the truncated-mode basis.

The second singular value λ_2 varies between 1.4 and 1.8 s K^{-1} depending on the model and kernel version, and a_2 corresponds approximately to a difference between
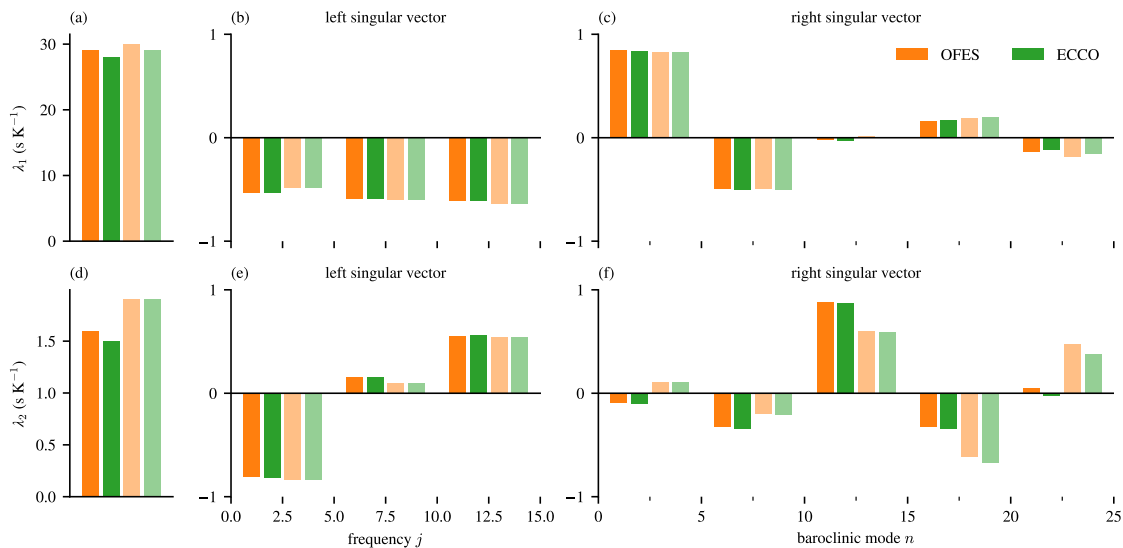
Figure 4.3: Singular value decomposition for various combinations of sensitivity kernels and model stratification profiles. Left singular vectors are the columns of **U**, and right singular vectors are the columns of **V**. Results are listed for the two largest singular values only. Three T wave frequencies (2.0, 3.0, and 4.0 Hz) and five baroclinic modes are used. The dark shading shows the SVD using the kernel version with sediment, and the light shading corresponds to the kernel version without sediment.

the travel time anomalies at 4.0 and 2.0 Hz or a differential temperature anomaly between the deep and mid-depth oceans. Baroclinic mode 3 dominates a_2 for the kernel with sediment, whereas mode 4 contributes most strongly to the kernel without sediment. The sensitivity $\lambda_2^{-1} \sum_j U_{j2}[K_j](z)$ of a_2 changes sign near the maximum of the a_1 sensitivity, being positive below and mostly negative above (Fig. 4.2d). Again, the corresponding mode combination $N_0^2 \sum_n V_{n2} G_n(z)$ mirrors this structure, up to the truncation of the mode basis (Fig. 4.2c).

The SVD of **A** thus allows us to construct $a_1(t)$ and $a_2(t)$ from the T wave data, which correspond to a combination of a small set of baroclinic modes along the T wave path. In the models, we can also form these mode combinations at every latitude and longitude, and we can regress those combinations against a_1 and a_2 in the biweekly band (10 to 17 days). What emerges in both cases is the anti-symmetric pattern across the equator of a Yanai wave (Fig. 4.4) that resembles the dominant mode in each combination (Fig. 4.1c,d). The pattern is more narrowly confined to near the equator for a_2, as expected from the dominant contribution of higher baroclinic modes with smaller equatorial deformation radii.
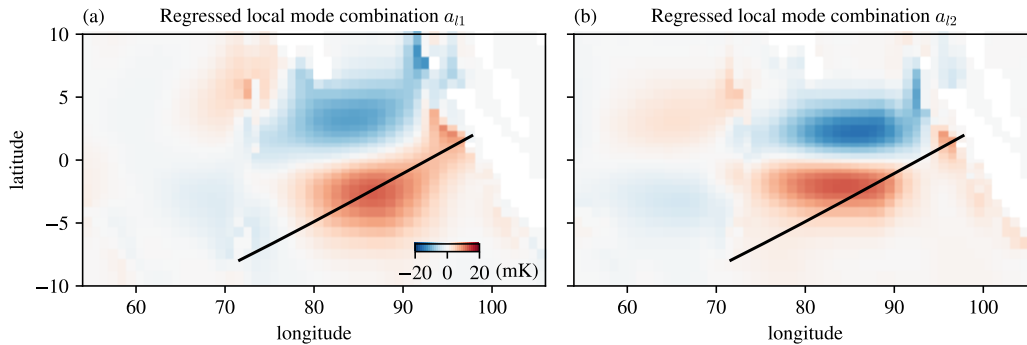
Figure 4.4: Yanai waves sampled by seismically generated T waves propagating from Nias Island to the hydrophone station H08 off Diego Garcia. Shown are Regression of local mode combinations onto the (a) a_1 and (b) a_2 from the T wave path as defined in (4.13). The calculation is based on the ECCO output and the kernel version with sediment. The black line shows the T wave path from Nias Island to Diego Garcia.

Inferring travel time anomalies from repeating earthquakes

The T wave observations determine only the arrival time change between repeating earthquakes. Given these T wave observations, the observations of arrival time changes of seismic waves received on land stations, and the prescription of a set of prior statistics, we invert for the travel time anomalies $\tau'_j(t)$ at acoustic frequency f_j. The inversion we use here is similar to that described in Callies et al. (2023), although we deviate from that procedure by specifying the prior statistics of T wave travel time anomalies based on the ECCO data, motivated by the close correspondence between the seismic data and the ECCO-inferred anomalies (Wu et al., 2020; Callies et al., 2023; Wu et al., 2023, see also below). Specifically, we convert potential temperature and salinity to in situ temperature on ECCO's original LLC90 grid in the Indian Ocean for the year 2005. We calculate daily temperature anomaly fields referenced to the annual mean and linearly interpolate at each depth level onto the great-circle path from Nias Island at 1.62°N, 96.92°E to H08 at 7.65°S, 72.49°E. The horizontal resolution along the path is 5 km, and we interpolate vertically onto a uniform grid with a resolution of 50 m. This grid coincides with that of the sensitivity kernel, and we estimate the daily travel time anomaly time series for each frequency by numerically integrating (4.9) without the approximation.

We calculate the auto-covariance functions for the travel time anomalies at each frequency and for the difference between each pair of frequencies (Fig. 4.5). The results show pronounced semi-annual and annual variability with long-term decay
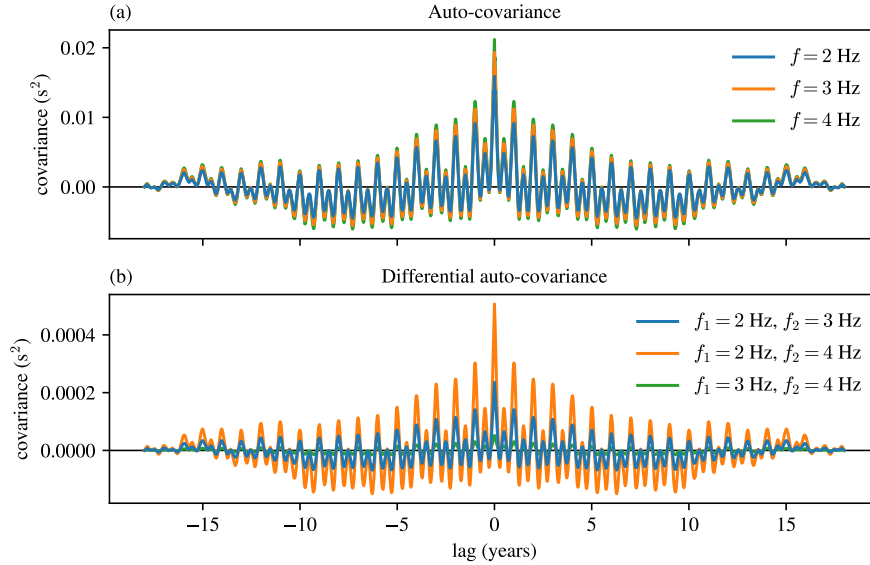
Figure 4.5: Covariance functions of *T* wave travel time anomalies in ECCO. Shown are (a) the auto-covariance of the travel time anomalies at the three acoustic frequencies and (b) the auto-covariance of differences between travel time anomalies at the three frequencies. The calculation shown here is based on sensitivity kernels from simulations with sediment.

that is, in part, due to edge effects. The covariance functions have very similar shapes at all three frequencies, suggesting strongly correlated measurements. The amplitude increases with frequency, consistent with an upward shift of the sensitivity kernels (Fig. 4.2b) and surface-intensified temperature anomalies. As expected, differences between the lowest and highest frequencies are largest and show the strongest auto-covariance. We add to this ECCO-based covariance model a linear trend with a prior uncertainty of 0.01 s yr^{-1} (cf., Callies et al., 2023).

We confirm that the travel time covariance in ECCO is similar to that in the *T* wave data through a direct comparison (Fig. 4.5). For the year 2005, we interpolate the synthetic travel time anomalies from ECCO onto the *T* wave event times to calculate travel time changes between repeating earthquakes. We then average the squares of the travel time changes for both ECCO and the *T* wave data over bins of 60 repeating pairs with a similar separation lag. For frequency f_j, we have

$$\frac{1}{2}\langle[\tau_j'(t+\Delta t)-\tau_j'(t)]^2\rangle = \langle\tau_j'^2(t)\rangle - \langle\tau_j'(t+\Delta t)\tau_j'(t)\rangle = \phi_{jj}(0) - \phi_{jj}(\Delta t), \quad (4.14)$$

where ϕ_{jj} is the auto-covariance function, assuming stationary statistics. The covariance of the travel time change that we can estimate from data therefore tracks the covariance of the travel time anomalies. ECCO captures these statistics quite well
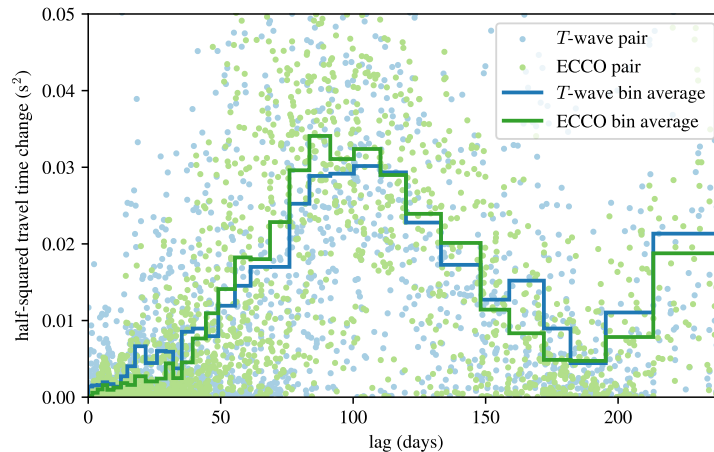
Figure 4.6: Covariance comparison between T wave data and ECCO output. The dots show one half times the square of the T wave travel time change between single repeating pairs at 2.0 Hz, and the curves show averages over bins that each contain 60 repeating pairs.

at 2.0 Hz (Fig. 4.6) and similarly at the other frequencies (not shown), supporting the assertion that ECCO's covariance is a reasonable approximation of the real covariance of T wave travel time anomalies and can be used in the inversion.

We adopt the method described in Peng et al. (2024) to distinguish between different measurement errors. We assume that errors arise from five distinct processes: an origin time error $\sigma_o = 1.3$ s, a discrepancy in the source location of the repeating earthquakes $\sigma_s = 30$ ms, a difference in the hydrophone location between the two events $\sigma_h = 30$ ms, and two errors, $\sigma_\varepsilon = 3$ ms and $\sigma_\eta = 18$ ms, arising from the correlation of noisy P/S and T waveforms, respectively. We estimate these errors via maximum likelihood with fixed ECCO prior covariances calculated and tested as described above. The estimate is not optimal because we only use repeaters that occurred in 2005 to reduce the computational cost, so we adjust the parameters slightly to reduce residual errors calculated with the full repeater catalog (Fig. 4.7). Specifically, we use the larger σ_h while the maximum likelihood estimate gives 21 ms and 26 ms for covariances with and without sediment, respectively. The correlation errors σ_ε and σ_η are also increased from the estimated 2 ms and 14 ms. The normalized distributions of residual quantiles are not statistically consistent with a standard Gaussian (Fig. 4.7), suggesting that either the noise priors are inconsistent or the real statistics is non-Gaussian. Yet we can interpret the inversion from an optimization perspective as minimizing error variances. Suggestions for how to further improve the prior statistics and uncertainty quantification in future work will
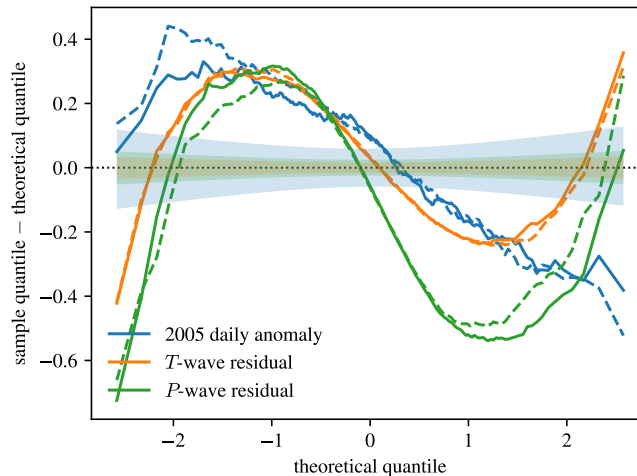
Figure 4.7: Posterior statistics of the inversion for T wave travel time anomalies. Shown is the difference between the sample quantile and the corresponding standard Gaussian theoretical quantile ($q_{\text{sample}} - q_{\text{theory}}$) plotted against the theoretical quantile (q_{theory}) for the daily T wave anomalies in 2005, the T wave residuals for the full set of repeating pairs, and the P/S-wave residuals for the same full set of repeating pairs. The transparent shading in corresponding colors indicates the two-sided 95% confidence interval for the respective estimates.

be discussed below.

We also adopt the technique described in Peng et al. (2024) to estimate the daily temperature anomalies in 2005 from the irregular T wave samples. The normalized quantile differences of these daily anomalies approximately follow a straight line with a negative slope (Fig. 4.7). This tilted line can show up when the anomalies agree with the ECCO covariance scaled by a smaller-than-unity factor. Therefore, the estimator is working as expected, underestimating the variance as any interpolation estimator. This can partly result from the high resolution in 2005 that well constrained the main signal, while the quantile plot for noise statistics is more complicated due to perhaps the use of the full set of repeaters. We subsequently transform the daily anomalies τ'_j to the singular vector projections a_1 and a_2, subtract a mean over the year 2005 to reduce uncertainties arising from longer time scales, and propagate the uncertainties accordingly.

Estimating baroclinic mode coefficients from deep mooring measurements

We estimate the coefficients of baroclinic modes from mooring velocity data following a procedure similar to that described by Wunsch (1997) but with a mode

covariance informed by the models. For every time sample (daily averages), the estimation problem is written as

$$y = \mathbf{E}x + n, \tag{4.15}$$

where y denotes the observations, x the mode coefficients to be estimated, n the residual due to a truncation of the mode basis plus measurement errors, and $\mathbf{E}$ the matrix that converts x to y. With one barotropic and six baroclinic modes in the calculation, the length of x is seven. Assuming x and n have Gaussian statistics with zero mean and covariances $\hat{\mathbf{C}}$ and $\boldsymbol{\Gamma}$, respectively, the probability distribution of $x \,|\, y$, i.e., the posterior distribution of x given the observations y, is also Gaussian, with the mean and covariance given by (e.g., Wunsch, 2006; Sanz-Alonso et al., 2018):

$$m = \mathbf{C}\mathbf{E}^{\mathrm{T}}\boldsymbol{\Gamma}^{-1}y \quad \text{and} \quad \mathbf{C} = (\hat{\mathbf{C}}^{-1} + \mathbf{E}^{\mathrm{T}}\boldsymbol{\Gamma}^{-1}\mathbf{E})^{-1}. \tag{4.16}$$

The square root of the diagonal part of $\mathbf{C}$ gives the standard errors of the estimate m.

To robustly estimate mode coefficients from the mooring observations, we select a subset of all available observations with good coverage of the water column. We only retain observational periods with five current meters on the mooring, which results in 390 days of observations at 77°E, 563 days at 83°E, and 389 days at 93°E(Fig. 4.8). During these observational periods, there are a few instruments above 1 km and the rest around 1, 2, and 4 km depth, with the exact depths depending on the specific locations and periods. We apply an 8-th order Butterworth filter (10 to 17 days) to both the observational and the model time series. The digital filter is applied forward and backward.

The prior covariance matrix for the mode coefficients $\hat{\mathbf{C}}$ and the residual covariance matrix $\boldsymbol{\Gamma}$ are computed using the output of OFES or ECCO. We compute the vertical modes from the model's mean stratification and project daily averages of the model's meridional velocity onto these modes. The result is the "true" value of x. The residual is $n = y - \mathbf{E}x$, where y is meridional velocity at the measurement depths of the moored instruments, is nonzero because we use a truncated set of seven modes (one barotropic plus six baroclinic modes); we tested the estimation with 20 modes, which gives essentially the same results. We compute the covariance matrices based on these model data as $\boldsymbol{\Gamma} = \langle nn^{\mathrm{T}}\rangle$ and $\hat{\mathbf{C}} = \langle xx^{\mathrm{T}}\rangle$, where the angle brackets denote time averages.

In order to compare model and mooring estimates on an equal footing and to evaluate the robustness of the estimates, we apply the estimation procedure to the model data
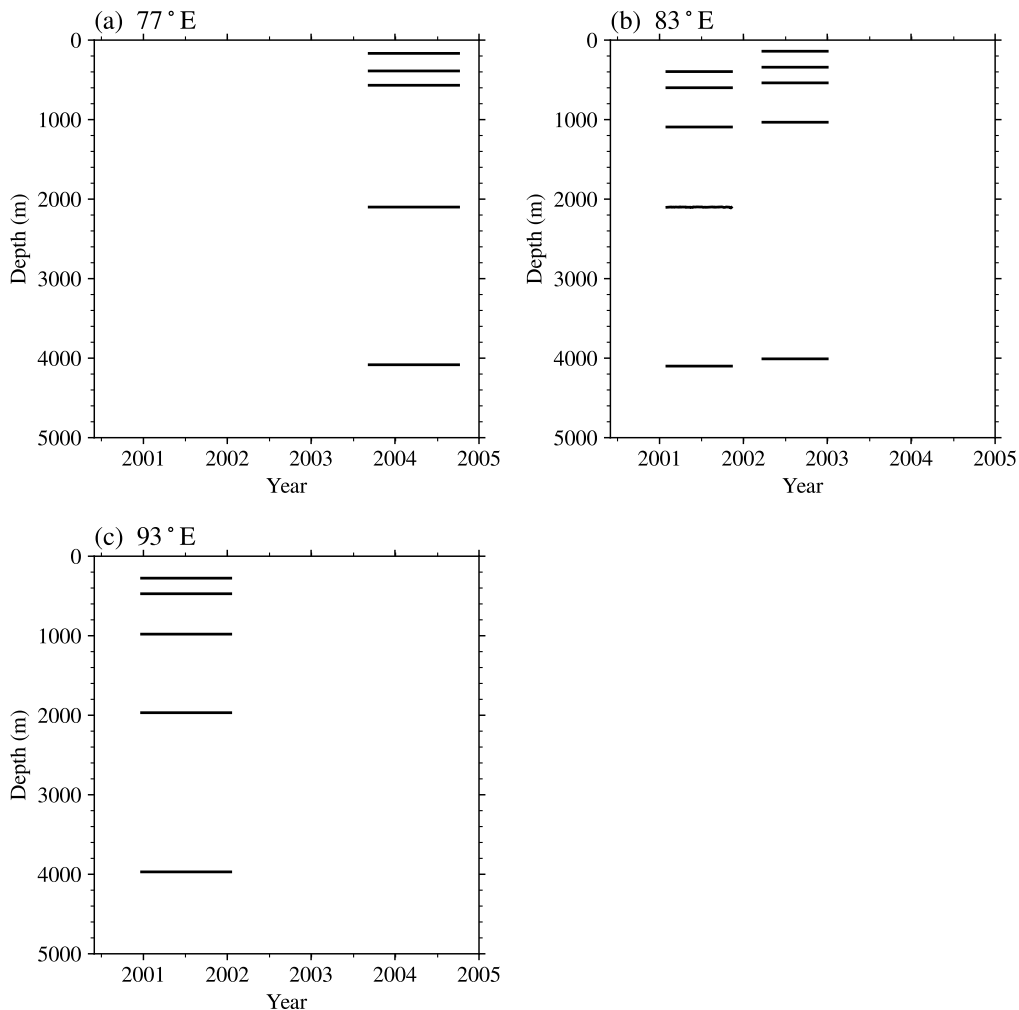
Figure 4.8: Availability of current meter observations at (a) 77°E, (b) 83°E, and (c) 93° along the equator as a function of time and depth.

sampled at the instrument locations and times. We analyze the difference between the estimate m and the actual vertical mode coefficients x computed from full profiles of the model velocities. For the first to third baroclinic modes, the distribution of $m - x$ is approximately a Gaussian, and the standard deviation of a fitted Gaussian is close to or slightly smaller than the uncertainty of m, the square root of the diagonal part of C. This indicates that our prior assumptions are reasonable, at least for the models. The comparison between the models and observations is more subtle and will be discussed in the results section.
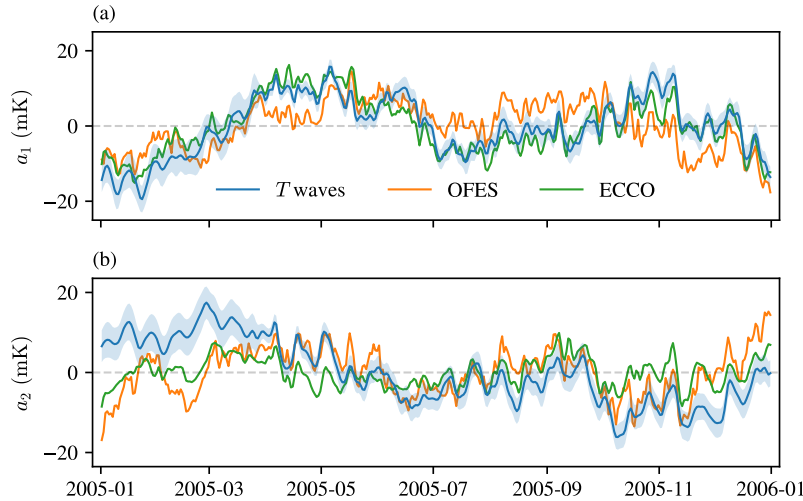
Figure 4.9: Projection coefficients of the 2005 daily travel time anomalies onto the first two singular vectors from T wave observations and the models. Shown are (a) the first singular vector projection a_1 corresponding to a weighted mean temperature anomaly and (b) the second singular vector projection a_2 corresponding to a differential temperature anomaly between the deep and mid-depth ocean (see Fig. 4.2c,d).

4.5   Results

Comparing observed and modeled T wave anomalies

The travel time anomaly combinations a_1 and a_2 in 2005 from both T wave data and model synthetics show clear seasonal and intraseasonal variability (Fig. 4.9). The semiannual cycle is related to the pronounced semi-annual wind forcing along the equator and the propagation of low frequency equatorial wave into the deep ocean (e.g. Huang et al., 2018). The two coefficients exhibit phase offsets, indicating that the baroclinic modes sampled by these coefficients are not in phase, consistent with the expected signals exhibiting vertical phase propagation (cf., Miyama et al., 2006). The observed and modeled variability is broadly in phase, and the amplitudes line up reasonably well. At the seasonal scale, the T wave estimate agrees better with the ECCO synthetics than those from OFES, but this is less clear in the biweekly band of primary interest here. For a more quantitative comparison, with a focus on this band, we next perform spectral and coherence analysis.

We calculate frequency power spectra of a_1 and a_2 from the T wave data and the models. We divide the 2005 time series into three half-year-long segments with 50% overlap and apply a Hann window, $w[n] = 0.5[1 - \cos(2\pi n/N)]$ with $0 \leq n \leq N$
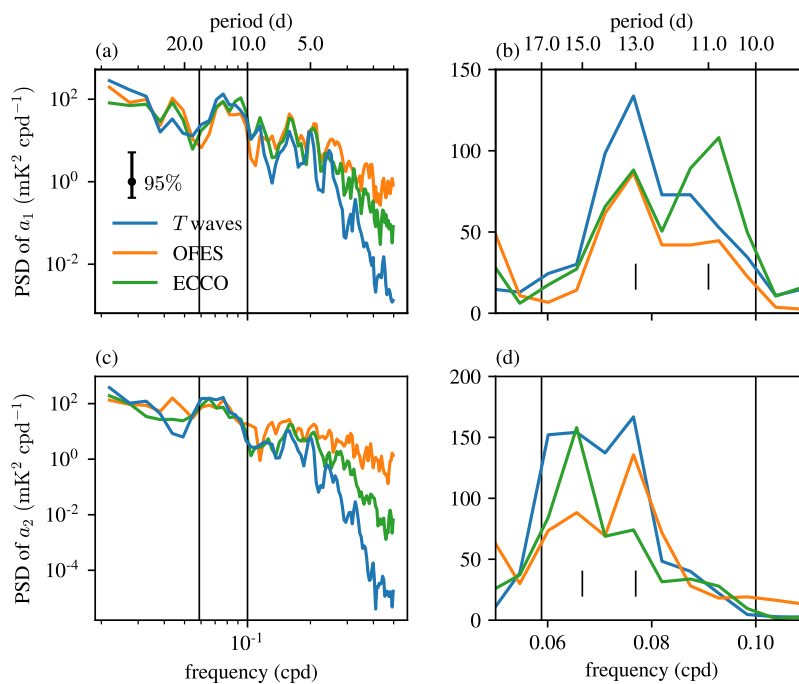
Figure 4.10: Spectra of the projection coefficients onto the first two singular vectors from T wave observations and models. Power spectra are shown for (a,b) a_1, corresponding to a weighted mean temperature anomaly, and (c,d) a_2, corresponding to a differential temperature anomaly between the deep and mid-depth ocean, both for the full resolved frequency range (left) and zoomed in to the biweekly band (right). The vertical bar in (a) shows the 95% confidence interval of the spectral estimation. Long black vertical lines mark the period of 10 to 17 days. Short black vertical lines mark periods at 11 and 13 days in (b) and 13 and 15 days in (d).

and $N = 183$, to each segment, and we average the periodograms from the three segments to estimate the spectrum. All spectra, for both a_1 and a_2, show distinct peaks in the biweekly band (Fig. 4.10). These peaks in the observational estimate are (marginally) significant at the 95% level despite the limited number of degrees of freedom from the short time series. For a_1, the data and both models show a peak at a period of 13 days, yet the spectral density in the observations is roughly 1.5 times that in the models. While this peak is the highest in the biweekly band for the data and OFES, ECCO has a stronger peak at 11 days. The data and OFES both have a hint of a secondary peak at this period. For a_2, the data and OFES have their strongest peak in the biweekly band at 13 days and a hint of a secondary peak at 15 days, whereas ECCO has its strongest peak at 15 days and a secondary peak at 13 days. The 13-day peak in the data is about 1.2 times that in OFES and double that
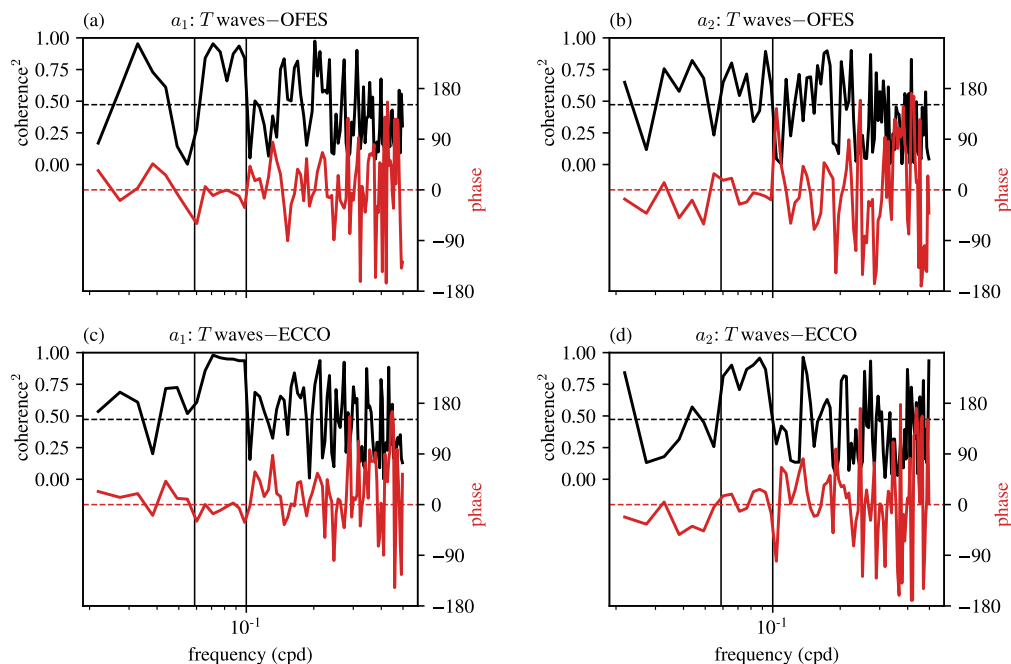
Figure 4.11: Coherence and phase of the projection coefficients onto the singular vectors between the models and T wave observations. Shown are (a,b) T waves vs. OFES and (c,d) T waves vs. ECCO. The left column is for a_1, and the right column is for a_2. The black horizontal lines show the 95% confidence level for squared coherence, and the red horizontal line shows a phase of 0°. Vertical lines mark the period of 10 to 17 days. Coherences are high between models and observations in this biweekly band.

in ECCO. The 15-day peak is comparable in the data and ECCO and suppressed to about half that value in OFES. The multi-peak nature in the biweekly band suggests contributions from various vertical modes (Miyama et al., 2006), and the shift of the biweekly peaks to lower frequencies in a_2 vs. a_1 is expected from the increase in dominant vertical-mode numbers.

The differences between the models and the data all fall within the spectral estimation error but are still significant because the signals are not independent random samples; they are the same realization and share the spectral estimation error. Instead, these differences result from uncertainties in the observations and the sensitivity kernels we use to interpret them, errors in the model simulations, or both.

The models show a high degree of phase coherence with the observations in the biweekly band (Fig. 4.11). For both a_1 and a_2, both OFES and ECCO are coherent with the observations at a 95% confidence level at the biweekly peaks, whereas

the coherence dips below that confidence level away from the peaks. Wherever the coherence is high, the phase is close to zero. ECCO exhibits a higher coherence with the data than OFES.

Overall, the models show remarkable similarity with the data, indicating that they are capable of at least qualitatively capturing the large-scale equatorial dynamics in the biweekly band. In the following, we therefore lean on the models to understand what vertical modes give rise to the biweekly peaks in a_1 and a_2.

Baroclinic-mode contributions to T wave anomalies

The models suggest that biweekly temperature anomalies averaged along the path from Nias Island to Diego Garcia are dominated by the first three baroclinic modes (Fig. 4.12ab), consistent with previous analysis of observations of upper-ocean velocity along the equator (Nagura and McPhaden, 2023). In OFES, modes 1 and 2 dominate the strongest biweekly peak at 13 days, mode 1 dominates the peak at 11 days, and mode 3 dominates the peak at 15 days, although modes 2 and 4 also contribute substantially (Fig. 4.12a). In ECCO, mode 2 more strongly dominates the peak at 13 days, mode 1 again dominates the peak at 11 days, and modes 2 and 3 contribute similarly to the peak at 15 days, with less of a contribution from mode 4 than in OFES (Fig. 4.12b). The increase of peak period with the mode number is consistent with the theoretical wave time scale $1/\sqrt{\beta c_n}$ that increases as c_n decreases with n. Specifically, we use $\beta = 2.3$ m^{-1} s^{-1} and the path-mean of c_n in ECCO to estimate the period scale $2\pi/\sqrt{\beta c_n}$ as 10, 12, and 16 d for modes 1 to 3, roughly agreeing with the spectra peaks. We can also relate these periods to the dispersion relation and infer the corresponding zonal wavelengths. For example, for mode 1, 11 d has a wavelength around 7700 km, roughly the full width of the Indian Ocean. This implies that the peak is reasonable and likely set by the wind forcing and ocean basin scales under resonance, although we do not expect these peaks to stay at the exact same periods among different years. Overall, the spectral density tends to decay with mode number, although this decay is slower in OFES than in ECCO, possibly we suspect because OFES is less viscous.

According to (4.13), the observed and modeled a_1 and a_2 sample a weighted linear combination of these temperature modes. The modes that dominate these combinations depend on both the amplitudes of the modes and the weighting as described by the singular vectors (Fig. 4.3). The biweekly variability of a_1 is strongly dominated by modes 1 and 2 (Fig. 4.12c,d). In both models, the peak at 13 days has comparable
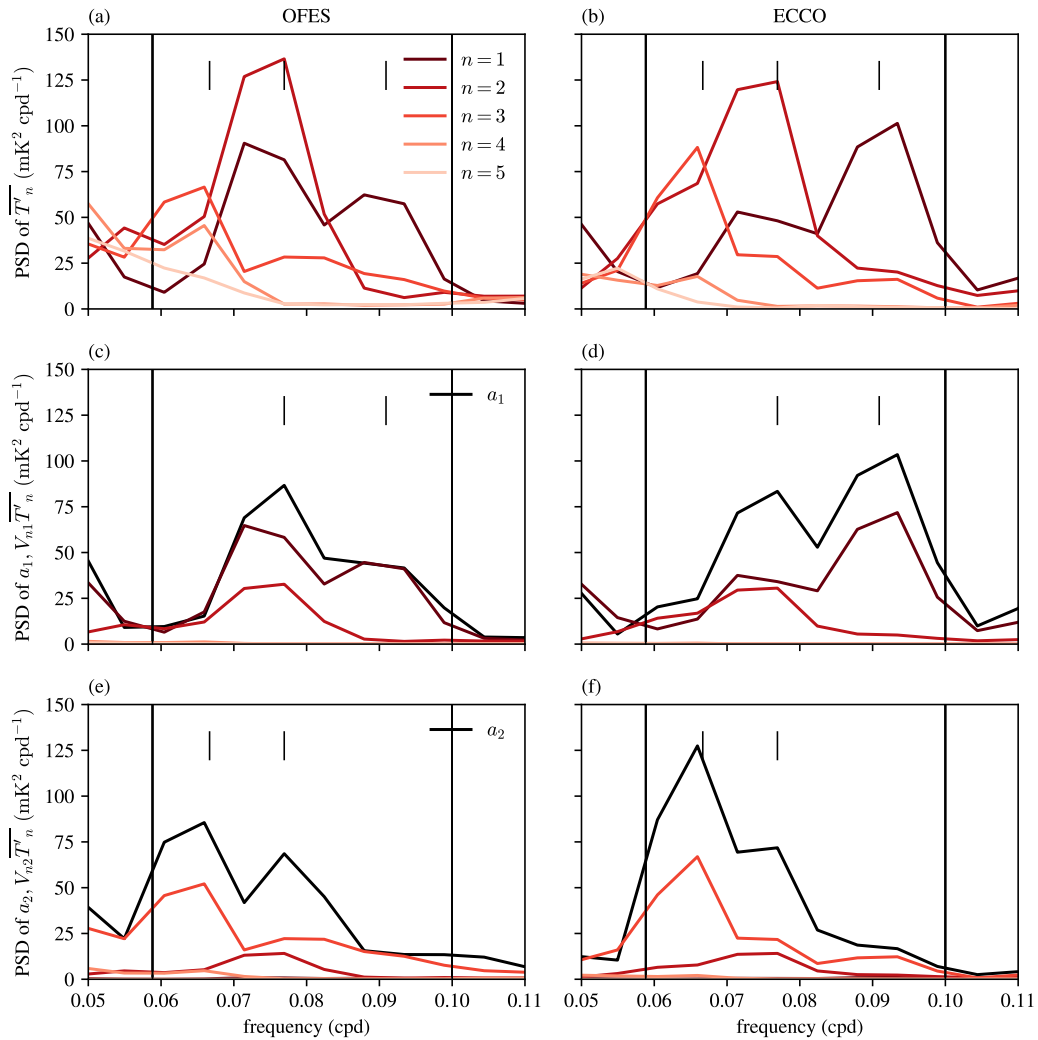
Figure 4.12: Power spectra of the baroclinic mode coefficients of temperature averaged along the T wave path from Nias Island to Diego Garcia. Shown are (a,b) the coefficients $\overline{T'_n}$ of the full signal, (c,d) the contributions $V_{n1}\overline{T'_n}$ to the singular-vector projection a_1, and (e,f) the contributions $V_{n2}\overline{T'_n}$ to the singular-vector projection a_2. The left and right columns show outputs from OFES and ECCO, respectively. Red lines with different brightness levels in the second and third rows indicate scaled mode coefficients sharing the same color code as those in (a). Long black vertical lines mark the period of 10 to 17 days. Short black vertical lines mark periods at 11 and 13 days in (a,b,c,d) and 13 and 15 days in (a,b,e,f).

contributions from modes 1 and 2, whereas the peak at 11 days is strongly domi-
nated by mode 1. The biweekly variability of a_2, instead, is dominated by mode 3
in both models (Fig. 4.12e,f). The peak at 15 days is strongly dominated by mode 3,
whereas the peak at 13 days has a sizable contribution from mode 2. The spectra
do not add up linearly because the modes are correlated, as expected for a vertically
propagating wave packet (Miyama et al., 2006).

This analysis indicates that ECCO has a stronger peak in the spectrum of a_1 at
11 days because its mode 1 is more energetic in that period than in OFES, and has
a stronger peak in the spectrum of a_2 at 15 days because it has more energy in
mode 3 at that period. Although the 13-day peak in a_2 differ between the models
in Fig. 4.10, they look very similar in Fig. 4.12e,f, which tends out to reflect the
range-independence approximation of eq. 4.13. The OFES peak will drop to half in
Fig. 4.10 if we use range-integrated kernels. These differences between the models
and the discrepancies with the T wave observations motivate our analysis of mooring
data below, which independently assesses the models' representation of modes 1
to 3, which dominate the signals in a_1 and a_2.

However, before describing the results of that analysis, we use regression analysis to
investigate the spatial context of the data along the T wave path (Fig. 4.4). We apply
a 5-th order Butterworth filter to filter the local temperature mode coefficients T'_n to
the biweekly band (10 to 17 days), form the combinations $\sum_n V_{n1} T'_n$ and $\sum_n V_{n2} T'_n$
corresponding to a_1 and a_2, and regress the resulting time series onto the time series
of a_1 and a_2 from the T wave path (at zero lag). For this analysis, we use ECCO
output and the kernel version with sediment. The same analysis applied to OFES
output gives very similar patterns (not shown).

The maps of the regression coefficients display antisymmetric patterns across the
equator (Fig. 4.4). For the low baroclinic modes that dominate these signals, the
dispersion relation of equatorial waves only permits antisymmetric Yanai waves and
symmetric Kelvin waves in the biweekly band, so antisymmetric regression patterns
suggest that Yanai waves dominate the biweekly T wave signals in a_1 and a_2. There is
also significant loading right on the equator near the eastern terminus of the ray path,
broader in a_1 than a_2, suggesting that T waves may have also sampled variabilities
due to coastal Kelvin waves there. Consistent with the dominant contributions of
mode 1 to a_1 and mode 3 to a_2, the regression pattern is more closely confined to
the equator for a_2 than for a_1, caused by a reduction in the equatorial deformation
radius with mode number (Fig. 4.1c,d). A lagged regression (not shown) further

reveals a westward phase propagation, consistent with Yanai waves.

Comparing deep-mooring data and model synthetics

Coupled to the antisymmetric temperature pattern, Yanai waves have a symmetric field of meridional velocities that peaks at the equator. For example, the regression pattern east of 70°E in Fig. 4.1c,d should correspond to a counterclockwise circulation with maximum southward meridional velocity around 70°E on the equator. Therefore, we analyze deep-mooring observations along the equator to independently access the biweekly variability in these wave modes. To infer baroclinic mode coefficients from the observations at a few depths, we use the inversion as described in Section 4.4 with priors estimated from OFES output. We use OFES-based priors throughout because the velocity variance at the moored instrument locations is more similar to the observed one in OFES than in ECCO. Our analysis suggests that ECCO tends to underestimate the variability in higher modes ($n \geq 4$) which contribute significant velocity variance, perhaps resulting from its coarse resolution. We include the barotropic mode in the inversion yet do not discuss it here because of its absence in temperature signals.

The equatorial meridional velocities in both models show pronounced variability in the biweekly band, with the largest contribution of order 10 cm s^{-1} coming from mode 2 (Fig. 4.13). We sample the models during the same periods as observations are available and estimate power spectra in the biweekly band. We estimate the power spectral density of the mode coefficients from each segment of the time series and then average the results over arbitrarily defined frequency grid points with a grid spacing of one cycle per 332 days. Every single spectrum is smoothed by applying a Hann window over the full time span. Both models show comparable biweekly variability, although ECCO generally has somewhat higher peaks than OFES (Fig. 4.14). The periods of the highest peak increases with mode number, from 12.5 days for mode 1 to 14 days for mode 2 and 16 days for mode 3. Similar to the peak period shift in the temperature mode spectra, this is also consistent with the increase in theoretical wave time scale with the mode number.

Before comparing this variability with the observations, we assess the robustness of the mode coefficient estimation by sampling the model output at the mooring locations and times. We compare the estimated mode coefficients $\boldsymbol{m}$ with the actual mode coefficients $\boldsymbol{x}$ calculated using the full-depth output (Fig. 4.13). The sampled estimate and full-depth calculation are statistically consistent, yet the estimated
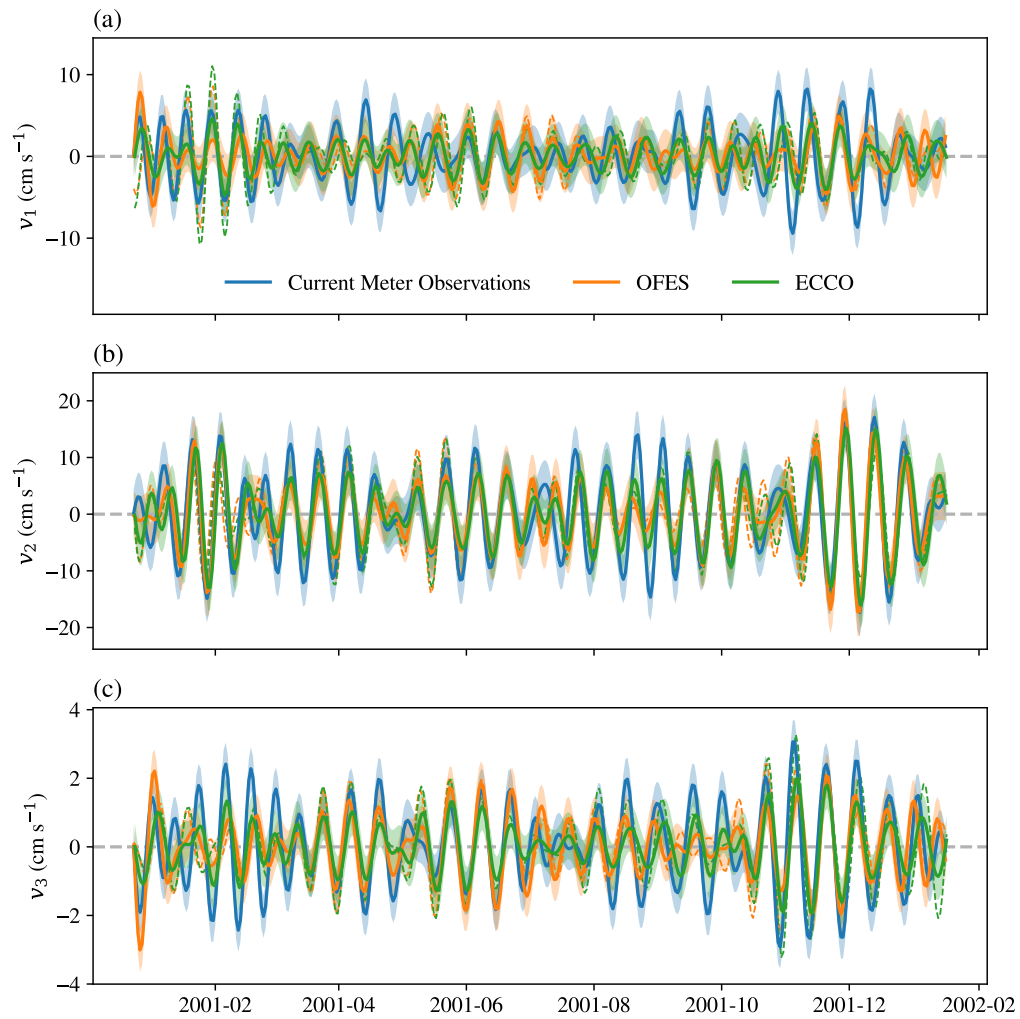
Figure 4.13: Time series of meridional velocity coefficients for the first three baroclinic modes estimated from equatorial moorings and model output at 93°E. Shown are (a) the first baroclinic mode coefficients v_1, (b) the second baroclinic mode coefficients v_2, and (c) the third baroclinic mode coefficients v_3.
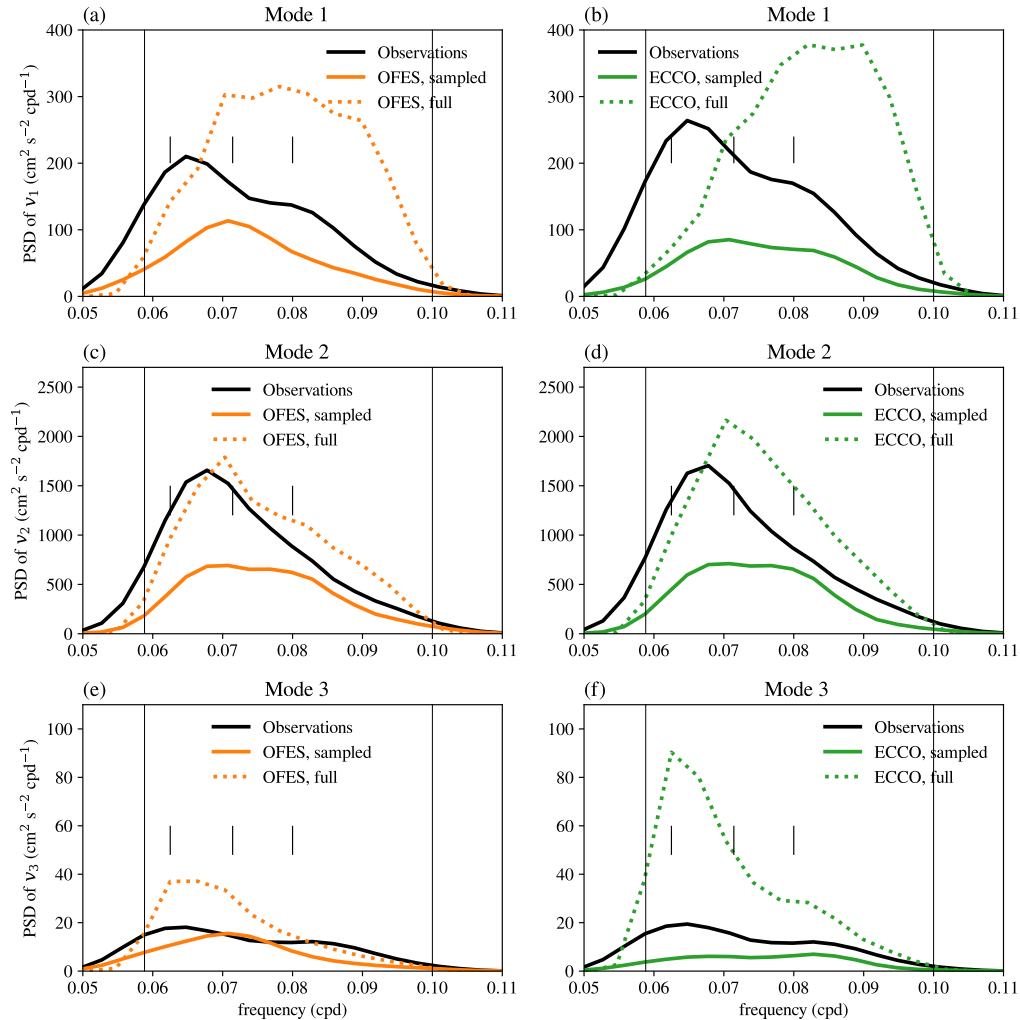
Figure 4.14: Spectra of meridional velocity coefficients for the first three baroclinic modes estimated from equatorial moorings and model output. Shown are the spectra estimated from observations using prior statistics from the respective model (black). For the models, two estimates are shown: the true modal spectrum (dotted) and the spectrum estimated from the model output sub-sampled at the moored instrument locations (solid). The estimation from all models and data use prior statistics from OFES. a). Long black vertical lines mark the period of 10 to 17 d. Short black vertical lines mark periods at 12.5, 14, and 16 d.

amplitudes are clearly reduced during some time intervals, and the phase can be slightly off. The sampled model spectra, calculated from m, substantially underestimate the corresponding full spectra, calculated from x (Fig. 4.14). This reduction is expected, given the sparsity of measurement depths, and must be taken into account when comparing the models to the data. It should also be noted that the estimation suppresses the variance unevenly across frequency, shifting the dominant peak for mode 1 from 12.5 to 14 days.

Given this imperfect estimation, we compare the estimates from observations with those from the sub-sampled models. The time series show a clear correspondence in amplitude and phase, although the amplitude tends to be higher in the observational estimates (Fig. 4.13). The differences between the estimates from the models and observations roughly follow a Gaussian distribution with a standard deviation close to the uncertainty of the estimate. Given that the two time series are highly correlated, consistency between the two signals would demand a much smaller standard deviation of the difference, coming from measurement and truncation errors. We conclude that the models' velocities are not statistically consistent with the observations.

This is also apparent in the comparison between frequency spectra estimated from the observations and the sub-sampled models, presuming the observational estimates suffer a similar suppression of variance. For all three modes, both OFES and ECCO underestimate the biweekly variance in the mooring data (Fig. 4.14). OFES shows closer agreement for mode 3, yet its biweekly variances in modes 1 and 2 are off by about 50%. ECCO generally shows about 50% reduction. The observation spectra also seem to show a longer-period peak than the model counterparts. Note that the slight amplitude difference between models for mode 1 spectra comes from the difference in stratification. This provides different $\mathbf{E}$ matrices, and the estimate with sparse samples is sensitive to the difference.

Overall, this comparison shows a similar degree of agreement between the models and mooring observations as we saw in the comparison between the models and the T wave observations. The models qualitatively capture the biweekly variability and show a remarkable fidelity in capturing its phase. Both models, however, appear to be off in the variance by a factor of two or so. We discuss reasons for this large reduction in variance in the models in Sec. 4.6.
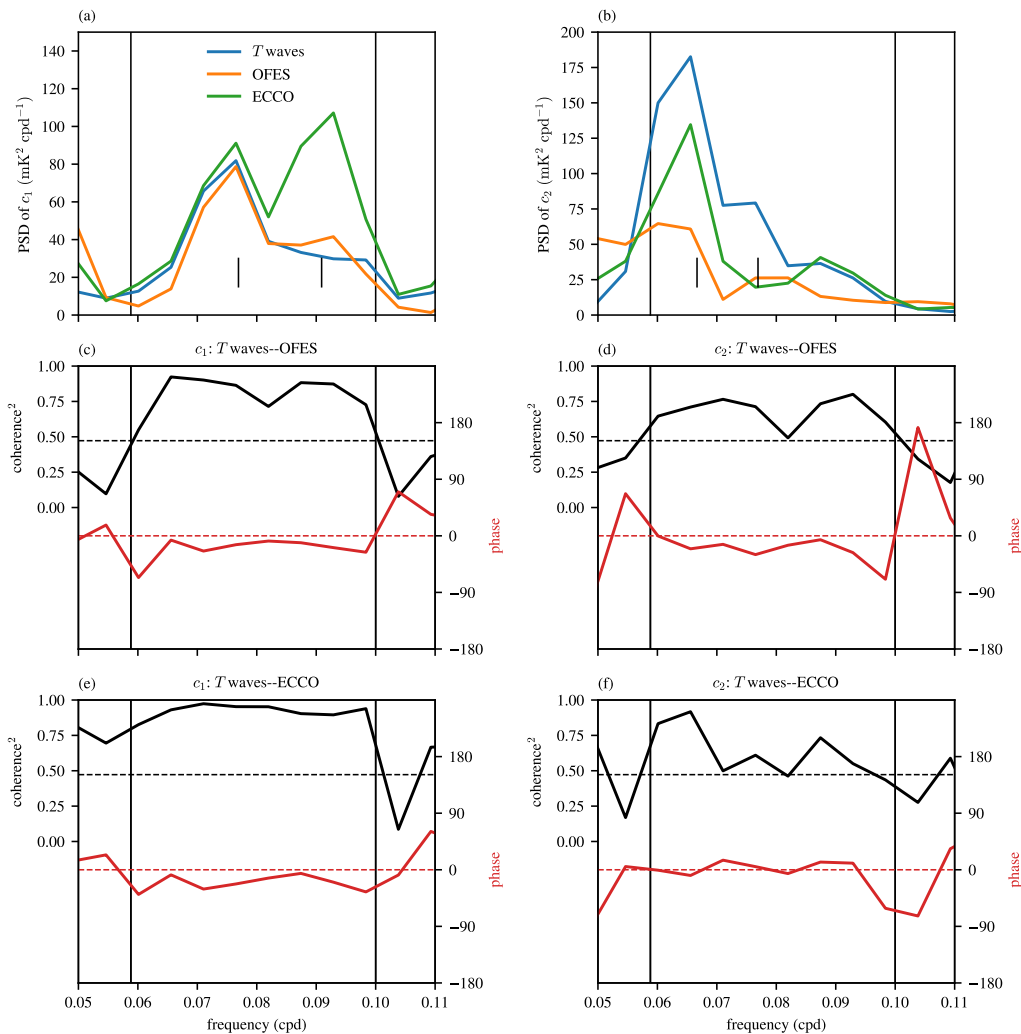
Figure 4.15: Spectra, coherence, and phase of the projection coefficients onto the first two singular vectors from T wave observations and models. Power spectra are shown for (a) a_1, corresponding to a weighted mean temperature anomaly, and (b) a_2, corresponding to a differential temperature anomaly between the deep and mid-depth ocean, for the zoomed in to the biweekly band. Coherence and phase are shown for (c,d) T waves vs. OFES, and (e,f): T waves vs. ECCO. The left column is for a_1, and the right column is for a_2. The black horizontal lines show the 95% confidence level for squared coherence, and the red horizontal line shows a phase of 0°. Long black vertical lines mark the period of 10 to 17 days. Short black vertical lines mark periods at 11 and 13 days in (a) and 13 and 15 days in (b).

Sensitivity of model–data comparison to kernel versions

If we use the (less realistic) sediment-free sensitivity kernel for the interpretation of the T wave data, the spectral and coherence analysis shows a similar degree of disagreement between the models and the data in the biweekly band (Fig. 4.15). For a_1, the spectral peak at 13 days now aligns well between the data and both models, whereas the peak at 11 days is still overestimated substantially by ECCO. For a_2, the models now underestimate the variance at both spectral peaks, with OFES suppressed by a factor of three or so. The biweekly coherence between the models and the data is still significant, and the phase remains close to zero. Taking the difference between the kernels with and without sediment as an estimate of the uncertainty in the kernel calculation, these results suggest that these uncertainties can have a substantial impact on model–data comparison. Given the disagreement between the two models and between the models and the mooring observations, however, these uncertainties in the kernels cannot be the sole cause for the disagreement with the data.

4.6   Discussion

T wave data takes a unique position in complementing the existing observation network in the Indian Ocean. Mooring buoys measure ocean parameters at high frequency, but most of their observations are usually confined to the upper 700 m (McPhaden et al., 2009). Current meters and ADCPs are deployed at mid-depth or below (Jain et al., 2021; Zeng et al., 2021), but the time series is fragmented and restricted to a few longitudes along the equator. Argo floats measure the upper 2000 m, but their sampling intervals are nominally 10 d owing to the limitation of the battery, and they do not resolve intraseasonal variability. Maintaining these observational arrays require cruises of research ships, which are costly. There is no guarantee that the current observational network will remain at the same level in the future. An example is the decline in the data acquisition rate during the COVID pandemic (Sprintall et al., 2024), which shows that these observations are susceptible to disruption from unexpected events. T wave data serves as a kind of "remote sensing" from land, which does not require expensive ship times, and obtains temperature measurements at high frequency. Therefore, we expect it to make critical contributions to the observing network of the Indian Ocean.

Mid-depth observations like this are important in understanding tropical wave dynamics. The relative magnitude of baroclinic modes is basic but poorly quantified information. We frequently use shallow-water equations or a 1.5-layer model to sim-

plify complicated problems, but these models require parameters of gravity wave phase speed or equivalent depth, which are usually estimated from observations. However, baroclinic modes are orthogonal functions occupying the whole water column, and reliable estimation requires data from the surface to the bottom. If we have observations only near the surface, the direct estimate of mode coefficients by projection does not work, because the baroclinic mode functions are not orthogonal in the upper ocean. Past studies estimated the dominant modes by computing the zonal phase speed of velocity from near-surface observations and comparing the results with baroclinic mode phase speeds (Pujiana and McPhaden, 2021; Arzeno et al., 2020) or using model output (Nagura and McPhaden, 2023). The first method is a guess, while the second method depends on models. It is best to observe ocean variables from the top to the bottom by in situ measurements, but it is costly and infeasible. Hopefully, high-frequency observations of mid-depth variations provided by T waves can help mitigate this problem, even though they are not strongly sensitive to changes near the surface and bottom.

That said, differences between the T wave data and the models can arise from errors in the data, their interpretation using sensitivity kernels and an inversion, the models, or a combination. We discuss potential causes of the mismatch to encourage future work in these areas.

The biweekly signals are dominantly equatorial Yanai waves resonantly excited by large-scale wind forcing. How strongly the forcing excites a given baroclinic mode depends on the realism of both the forcing and the mixed-layer turbulence, which redistributes momentum and dissipates energy. OFES uses a prescribed forcing from reanalysis, whereas ECCO allows for an adjustment to the forcing to better match observations. (The T wave data are not currently used in the ECCO estimate.) It is not clear whether uncertainties in the forcing are large enough to explain the differences with the data and whether adjustments consistent with these uncertainties could be made to eliminate much of the mismatch. To represent mixed-layer turbulence, OFES uses a model developed from the Mellow–Yamada closure (Noh and Jin Kim, 1999), whereas ECCO uses the GGL parameterization (Gaspar et al., 1990). Both come with uncertainties that translate into uncertainties in the projection of a given forcing onto the baroclinic modes.

Once the Yanai waves have been excited, they propagate from the surface to the deep ocean and can reflect off the bottom. They can also interact with other wave modes through reflection off the coasts. During their propagation, the wave modes

are damped by vertical mixing, which is poorly constrained by observations. Higher baroclinic modes should be damped more strongly and thus are more sensitive to the model representation of mixing. The interaction with the seafloor requires high resolution bathymetry—the reflection off the bottom is likely too efficient in ECCO. The regional domain of the OFES simulation may negatively affect its ability to capture the interaction of Yanai waves with other wave modes, such as coastal Kelvin waves and subtropical Rossby waves that can propagate out of the domain.

The inversion we use to convert estimate T wave travel time anomalies from arrival time changes between repeating events introduces uncertainties in the observational estimates. To minimize this effect, we analyze the year 2005, where the sampling was densest because of abundant aftershocks of the M 8.6 Nias–Simeulue earthquake. Still, the estimation from the imperfect sampling tends to smooth out anomalies and should suppress the biweekly variance. For the most part, accounting for this suppression would increase the mismatch with the models.

The inversion also imparts errors because it makes simplifying assumptions for the statistics. The significant deviation of the residual distributions from the thin confidence intervals (Fig. 4.7) indicates that our assumed signal and noise covariances do not fully capture the statistics of the real signals. This can be attributed in part to simplifications in the noise components, in which T- and P/S- waveform correlation errors are independent and identically Gaussian, location errors are isotropic, and kernel errors are ignored. In practice, T wave correlation error can be sensitive to frequency which affects coherency between repeating waveforms (Callies et al., 2023). If we consider correlation to be correlated with the error, higher frequencies give smaller correlation peaks and probably more errors. Errors of the same pair are also correlated among frequencies. Sensitivity profiles of different frequencies are highly correlated, and the ocean-induced errors would be quite similar. The P/S-wave correlation error varies across reference stations. The source and receiver location errors are generally anisotropic as a result of inhomogeneities in the solid Earth and ocean. The use of two versions of kernels changes the prior anomaly covariance with yet similar residual distributions, but further study is needed to confirm if the residual is sensitive to a prior noise covariance arising from uncertainty in the kernels.

Apart from the structure of the noise covariance, the choice of corresponding parameters also affects residuals, and estimates based on sub-sampled data can deviate substantially from those based on full data (Peng et al., 2024). Yet we have found

that tuning these parameters only alters the residual scale, while the non-Gaussian shape with fat tails and thin quartiles remains qualitatively unchanged. Therefore, future work should refine the noise covariance to improve the consistency of the residuals as well as the comparison with models.

Aside from the uncertainty in the sensitivity kernels arising from the prescription of a sediment layer and its properties, the underlying calculation approximates the propagation as two-dimensional. The excitation of T waves is known to be extended along the trench, such that a three-dimensional volume rather than a two-dimensional section is sampled. Three-dimensional sensitivity kernel calculations, while computationally demanding, would significantly improve our representation of the measured T wave arrival time changes. Its feasibility can be explored in future work.

4.7   Conclusions

Seismic T waves, generated at Nias Island and propagating towards Diego Garcia, sample the deep equatorial East Indian Ocean. The anomalies in their travel time capture biweekly temperature variability due to Yanai waves. Measurements at a few acoustic frequencies constrain the vertical structure of the Yanai waves as captured by a few baroclinic modes. The variability inferred from these observations is qualitatively consistent with the output of numerical models sampled in the same way, although quantitative differences are apparent. These differences can be used to improve the models, for example, by helping calibrate uncertain parameterizations like diffusivity. The quantitative mismatch also indicates that including the T wave observations in a state estimate like ECCO would provide improved constraints and improve the estimates. Since vertical propagation of Yanai waves contribute to important climate processes like equatorial heating and abyssal mixing (e.g., Nagura et al., 2014; Delorme and Thomas, 2019), these improvement would help models to be more reliable in simulating these transients under climate change.

Although previous works have used T waves to investigate long-term warming trends in the deep Indian ocean (Wu et al., 2020; Callies et al., 2023; Wu et al., 2023), transient dynamics like equatorial waves and semi-annual cycle in the tropical Indian Ocean provide opportunities to further calibrate and improve the method. Future work should continue to reduce uncertainties in the interpretation of T wave observations by better accounting for their three-dimensionality and by improving the representation of the sediment layer in the calculation of sensitivity kernels.

Improved observations, for example by a vertical hydrophone array, would further increase the amount of information that can be extracted from T wave data. The vertical propagation of Yanai waves could be captured with much more detail. And the framework that better resolve Yanai waves as well as agree with models can be applied more broadly to advance our understanding of more complex dynamics, like the mesoscale variability in the Kuroshio Extension region (Peng et al., 2024) and the deep water formation and warming in the Southern Ocean.

Chapter 5

CONCLUSIONS

This dissertation addresses several challenges in the pursuit of a global observing network of temperatures in the deep ocean using sound waves generated by natural earthquakes. Seismic thermometry is developed to complement in situ techniques. This method is applied to the Kuroshio Extension region to demonstrate its ability to sample temperature changes in subtropical oceans with intense intrinsic variabilities. A well-calibrated inversion can extract these temperature changes from the noisy data and quantify their uncertainties. Consistency between the seismic data and other independent ocean observations is presented first from a qualitative perspective. The agreement confirms that variations in ocean temperature dominate changes in travel time of repeating sound waves, so-called T waves.

To show statistical consistency between temperatures inferred from T waves and measurements from autonomous Argo floats, a comprehensive covariance structure is proposed. A corresponding inversion is introduced to confirm the quantitative consistency between T wave and Argo data. This updated inversion further permits basin-scale temperature estimates and uncertainty quantification, which highlights that the seismic data reduce uncertainties in basin-scale temperature changes when combined with the conventional data. The inferred temperature has a persistent warming after 2008, yet the trend is less significant than if it had started in 1997. It is suggested that the latter warming is dominated by changes in the Kuroshio Extension close to the coast of Japan, but more detailed analysis is required to clarify the mechanism.

A plausible approach is to investigate synthetic T wave signals in an ensemble of ocean models. The ensemble is expected to have realistic forcing and properly account for mesoscale dynamics. If the synthetic results show systematic warming among models, then this suggest consistent forced changes in the region. Even though the Kuroshio Extension has its own intrinsic variabilities, they would be less important in this case. On the other hand, stochastic change could be more critical if the ensemble expresses a wide range of behaviors. It would then be interesting to compare stochastic changes among the data and models to understand the relevant dynamics. The consistency between T wave data and synthetics could also be

helpful in improving the covariance structure used to infer real ocean temperatures.

The data-model comparison in the equatorial Indian Ocean provide such an example study. It focuses on the more classic linear wave dynamics and presents the potential of using T waves to understand specific ocean physics. However, this region still lacks systematic temperature measurements that combine T wave data with conventional data. The main challenge is perhaps the covariance structure that is unique to the equatorial region. Since large-scale waves dominate temperature variations, we expect ocean models to provide a more straightforward point-wise covariance. This could be similar to how we estimate the T wave covariance from ECCO, and the complication would be to obtain various covariances among conventional and seismic data. This analysis can study the consistency between the two data sources from a quantitative perspective and estimate the potential for reducing temperature uncertainty with the seismic data here. Broadly speaking, the use of ocean model covariance still assumes a Gaussian random field model for the inverse problem. Therefore, future studies can explore the potential of more sophisticated neural network architectures on emulating the realistic non-Gaussian mapping from ocean temperatures to seismic and conventional data.

How the ocean deforms T waves is also an open question. This is coupled to the complexity of the multipath propagation of T waves. If the waveform consists of multiple arrivals, a reasonable idea is to understand and separate various arrivals. Given enough resources, a reasonable approach is to infer arrival distribution at the excitation by having more hydrophone stations in the transverse direction. The first arrival come from the direct path and have the highest coherence among repeaters. With only the first arrival, it would be possible to improve the detection of T waves, especially in the Kuroshio Extension region. This could lead to the possibility of mapping the entire Pacific basin with a few hydrophones, and the first step might be to estimate the statistics of repeating T waves along the coast. The preparation would require understanding or assumptions of the seismicity, repeating frequency, an effect due to ocean dynamics and bathymetry, etc.

Regardless of promising studies on the source property and propagation of T waves, it is the receiver that anchors the spatiotemporal coverage and provides the data. The use of a single hydrophone or near-shore seismic station is discussed, and each type has its potential for improvement. Vertical array of hydrophones has been deployed to resolve vertical temperature structure with controlled sound sources, it is yet to be implemented for repeating T waves. A pioneer study can investigate the

feasibility of using a vertical hydrophone array to resolve various acoustic modes given an idealised sound speed profile in the ocean. This problem is more interesting than the controlled experiment, since it requires further separating different arrivals from differential measurements. For seismic T wave stations, they could make critical contributions to constraining historical ocean temperatures. Since earlier signals might have not been well documented and digitized, this would be a good practice of literature research. Further, tomography becomes plausible, once the spatial distribution of receivers permit intersecting sample paths that divide the basin into a well-mapped grid. We can also achieve this by sampling single T waves with hydrophones attached to Argo-like autonomous floats. Once the repeating requirement is released, the application of seismic thermometry/tomography to other basins with moderate seismicity, like the Atlantic and the Southern Oceans, also becomes more accessible.

BIBLIOGRAPHY

Abraham, J. P. et al. (2013). "A Review of Global Ocean Temperature Observations: Implications for Ocean Heat Content Estimates and Climate Change". In: *Reviews of Geophysics* 51.3, pp. 450–483. DOI: 10.1002/rog.20022.

Arzeno, I. B., S. N. Giddings, G. Pawlak, and R. Pinkel (2020). "Generation of Quasi-Biweekly Yanai Waves in the Equatorial Indian Ocean". In: *Geophysical Research Letters* 47.16, e2020GL088915. DOI: 10.1029/2020GL088915.

Baugh, S. and K. McKinnon (2022). "Hierarchical Bayesian Modeling of Ocean Heat Content and Its Uncertainty". In: *The Annals of Applied Statistics* 16.4, pp. 2603–2625. DOI: 10.1214/22-AOAS1605.

Boyer, T. P. et al. (2018). *World Ocean Database 2018*.

Callies, J. and W. Wu (2019). "Some Expectations for Submesoscale Sea Surface Height Variance Spectra". In: *Journal of Physical Oceanography* 49.9, pp. 2271–2289. DOI: 10.1175/JPO-D-18-0272.1.

Callies, J., W. Wu, S. Peng, and Z. Zhan (2023). "Vertical-Slice Ocean Tomography With Seismic Waves". In: *Geophysical Research Letters* 50.8, e2023GL102881. DOI: 10.1029/2023GL102881.

Cheng, L. et al. (2022). "Past and future ocean warming". In: *Nature Reviews Earth and Environment* 3.11, pp. 776–794. DOI: 10.1038/s43017-022-00345-1.

Dee, D. P. et al. (2011). "The ERA-Interim reanalysis: configuration and performance of the data assimilation system". In: *Quarterly Journal of the Royal Meteorological Society* 137.656, pp. 553–597. DOI: 10.1002/qj.828.

De Groot-Hedlin, C. and J. Orcutt (1999). "Synthesis of earthquake-generated T-waves". In: *Geophys. Res. Lett.* 26.9, pp. 1227–1230. DOI: 10.1029/1999GL900205.

Delorme, B. L. and L. N. Thomas (2019). "Abyssal Mixing through Critical Reflection of Equatorially Trapped Waves off Smooth Topography". In: *Journal of Physical Oceanography* 49.2, pp. 519–542. DOI: 10.1175/JPO-D-18-0197.1.

Desbruyères, D., E. L. McDonagh, B. A. King, and V. Thierry (2017). "Global and Full-Depth Ocean Temperature Trends during the Early Twenty-First Century from Argo and Repeat Hydrography". In: *Journal of Climate* 30.6, pp. 1985–1997. DOI: 10.1175/JCLI-D-16-0396.1.

Dushaw, B. D. et al. (1999). "Multimegameter-range acoustic data obtained by bottom-mounted hydrophone arrays for measurement of ocean temperature". In: *IEEE Journal of Oceanic Engineering* 24.2, pp. 202–214. DOI: 10.1109/48.757271.

Dushaw, B. D. et al. (2009). "A decade of acoustic thermometry in the North Pacific Ocean". In: *Journal of Geophysical Research (Oceans)* 114.C7, C07021, p. C07021. DOI: 10.1029/2008JC005124.

Dushaw, B. D. (2014). "Assessing the horizontal refraction of ocean acoustic tomography signals using high-resolution ocean state estimates". In: *Acoustical Society of America Journal* 136.1, pp. 122–129. DOI: 10.1121/1.4881928.

ECCO Consortium, I. Fukumori, O. Wang, I. Fenty, G. Forget, P. Heimbach, and R. M. Ponte (2021). *Synopsis of the ECCO Central Production Global Ocean and Sea-Ice State Estimate, Version 4 Release 4*. Version 4 Release 4. DOI: 10.5281/zenodo.4533349.

Forget, G., J.-M. Campin, P. Heimbach, C. N. Hill, R. M. Ponte, and C. Wunsch (2015). "ECCO version 4: an integrated framework for non-linear inverse modeling and global ocean state estimation". In: *Geosci. Model Dev.* 8, pp. 3071–3104. DOI: 10.5194/gmd-8-3071-2015.

Garcia, H. E. et al. (2019). *World Ocean Atlas: Product Documentation*.

Gaspar, P., Y. Grégoris, and J.-M. Lefevre (1990). "A simple eddy kinetic energy model for simulations of the oceanic vertical mixing: Tests at station Papa and long-term upper ocean study site". In: *Journal of Geophysical Research: Oceans* 95.C9, pp. 16179–16193. DOI: 10.1029/JC095iC09p16179.

Genz, A. and A. Malik (1980). "Remarks on algorithm 006: An adaptive algorithm for numerical integration over an N-dimensional rectangular region". In: *Journal of Computational and Applied Mathematics* 6.4, pp. 295–302. DOI: 10.1016/0771-050X(80)90039-X.

Gill, A. and P. Niller (1973). "The theory of the seasonal variability in the ocean". In: *Deep Sea Research and Oceanographic Abstracts* 20.2, pp. 141–177. DOI: 10.1016/0011-7471(73)90049-1.

Gill, A. E. (2006). *Atmosphere-ocean dynamics*. Nachdr. International geophysics series 30. San Diego: Acad. Press. 662 pp.

Hansen, J., G. Russell, A. Lacis, I. Fung, D. Rind, and P. Stone (1985). "Climate Response Times: Dependence on Climate Sensitivity and Ocean Mixing". In: *Science* 229.4716, pp. 857–859. DOI: 10.1126/science.229.4716.857.

Heaney, K. D. and R. L. Campbell (2016). "Three-dimensional parabolic equation modeling of mesoscale eddy deflection". In: *Acoustical Society of America Journal* 139.2, pp. 918–926. DOI: 10.1121/1.4942112.

Held, I. M., M. Winton, K. Takahashi, T. Delworth, F. Zeng, and G. K. Vallis (2010). "Probing the Fast and Slow Components of Global Warming by Returning Abruptly to Preindustrial Forcing". en. In: *Journal of Climate* 23.9, pp. 2418–2427. DOI: 10.1175/2009JCLI3466.1.

Huang, K. et al. (2018). "Vertical Propagation of Middepth Zonal Currents Associated With Surface Wind Forcing in the Equatorial Indian Ocean". In: *Journal of Geophysical Research: Oceans* 123.10, pp. 7290–7307. DOI: `10.1029/2018JC013977`.

Igarashi, T. (2020). "Catalog of small repeating earthquakes for the Japanese Islands". In: *Earth, Planets and Space* 72.1, p. 73. DOI: `10.1186/s40623-020-01205-2`.

Jain, V. et al. (2021). "Two decades of current observations in the equatorial Indian Ocean". In: *Journal of Earth System Science* 130.2, 75, p. 75. DOI: `10.1007/s12040-021-01568-4`.

Kaipio, J. and E. Somersalo (2005). *Statistical and Computational Inverse Problems*. Vol. 160. Springer New York, NY. DOI: `10.1007/b138659`.

Kawabe, M. (1995). "Variations of Current Path, Velocity, and Volume Transport of the Kuroshio in Relation with the Large Meander". In: *Journal of Physical Oceanography* 25.12, pp. 3103–3117. DOI: `10.1175/1520-0485(1995)025<3103:VOCPVA>2.0.CO;2`.

Kelly, S. M. (2016). "The Vertical Mode Decomposition of Surface and Internal Tides in the Presence of a Free Surface and Arbitrary Topography". In: *Journal of Physical Oceanography* 46.12. Publisher: American Meteorological Society Section: Journal of Physical Oceanography, pp. 3777–3788. DOI: `10.1175/JPO-D-16-0131.1`.

Kuusela, M. and M. L. Stein (2018). "Locally stationary spatio-temporal interpolation of Argo profiling float data". In: *Proceedings of the Royal Society of London Series A* 474.2220, p. 20180400. DOI: `10.1098/rspa.2018.0400`.

Lawrence, A. and J. Callies (2022). "Seasonality and Spatial Dependence of Mesoscale and Submesoscale Ocean Currents from Along-Track Satellite Altimetry". In: *Journal of Physical Oceanography* 52.9, pp. 2069–2089. DOI: `10.1175/JPO-D-22-0007.1`.

Lebedev, K. V., M. Yaremchuk, H. Mitsudera, I. Nakano, and G. Yuan (2003). "Monitoring the Kuroshio Extension with Dynamically Constrained Synthesis of the Acoustic Tomography, Satellite Altimeter and in situ Data". In: *Journal of Oceanography* 59.6, pp. 751–763. DOI: `10.1023/B:JOCE.0000009568.06949.c5`.

Levitus, S., J. I. Antonov, T. P. Boyer, and C. Stephens (2000). "Warming of the World Ocean". In: *Science* 287.5461, pp. 2225–2229. DOI: `10.1126/science.287.5461.2225`.

Li, Z., M. H. England, and S. Groeskamp (2023). "Recent Acceleration in Global Ocean Heat Accumulation by Mode and Intermediate Waters". In: *Nature Communications* 14.1, p. 6888. DOI: `10.1038/s41467-023-42468-z`.

Mantua, N. J., S. R. Hare, Y. Zhang, J. M. Wallace, and R. C. Francis (1997). "A Pacific Interdecadal Climate Oscillation with Impacts on Salmon Production*". In: *Bulletin of the American Meteorological Society* 78.6, pp. 1069–1080. DOI: `10.1175/1520-0477(1997)078<1069:APICOW>2.0.CO;2`.

Masumoto, Y., H. Hase, Y. Kuroda, H. Matsuura, and K. Takeuchi (2005). "Intraseasonal variability in the upper layer currents observed in the eastern equatorial Indian Ocean". In: *Geophysical Research Letters* 32.2. DOI: `10.1029/2004GL021896`.

Masumoto, Y. et al. (2004). "A Fifty-Year Eddy-Resolving Simulation of the World Ocean -Preliminary Outcomes of OFES (OGCM for the Earth Simulator)-". In: *Journal of the Earth Simulator* 1, pp. 35–56.

McDougall, T. J. and P. M. Barker (2011). *Getting Started with TEOS-10 and the Gibbs Seawater (GSW) Oceanographic Toolbox*.

McPhaden, M. J. et al. (2009). "RAMA: The Research Moored Array for African–Asian–Australian Monsoon Analysis and Prediction*". In: *Bulletin of the American Meteorological Society* 90.4, pp. 459–480. DOI: `10.1175/2008BAMS2608.1`.

Meyssignac, B. et al. (2019). "Measuring Global Ocean Heat Content to Estimate the Earth Energy Imbalance". In: *Frontiers in Marine Science* 6. DOI: `10.3389/fmars.2019.00432`.

Miyama, T., J. P. McCreary, D. Sengupta, and R. Senan (2006). "Dynamics of Biweekly Oscillations in the Equatorial Indian Ocean*". In: *Journal of Physical Oceanography* 36.5, pp. 827–846. DOI: `10.1175/JPO2897.1`.

Mizuno, K. and W. B. White (1983). "Annual and Interannual Variability in the Kuroshio Current System". In: *Journal of Physical Oceanography* 13.10, pp. 1847–1867. DOI: `10.1175/1520-0485(1983)013<1847:AAIVIT>2.0.CO;2`.

Munk, W., P. Worcester, and C. Wunsch (1995). *Ocean Acoustic Tomography*. Cambridge Monographs on Mechanics. Cambridge: Cambridge University Press. DOI: `10.1017/CBO9780511666926`.

Munk, W. H. (1980). "Horizontal Deflection of Acoustic Paths by Mesoscale Eddies". In: *Journal of Physical Oceanography* 10.4, pp. 596–604. DOI: `10.1175/1520-0485(1980)010<0596:HDOAPB>2.0.CO;2`.

Munk, W. H. and C. Wunsch (1979). "Ocean acoustic tomography: a scheme for large scale monitoring". In: *Deep Sea Research A* 26.2, pp. 123–161. DOI: `10.1016/0198-0149(79)90073-6`.

Na, H., D. R. Watts, J.-H. Park, C. Jeon, H. J. Lee, M. Nonaka, and A. D. Greene (2016). "Bottom pressure variability in the Kuroshio Extension driven by the atmosphere and ocean instabilities". In: *Journal of Geophysical Research (Oceans)* 121.8, pp. 6507–6519. DOI: `10.1002/2016JC012097`.

Nagura, M., Y. Masumoto, and T. Horii (2014). "Meridional Heat Advection due to Mixed Rossby Gravity Waves in the Equatorial Indian Ocean". In: *Journal of Physical Oceanography* 44.1, pp. 343–358. DOI: 10.1175/JPO-D-13-0141.1.

Nagura, M. and M. J. McPhaden (2023). "Dual-Frequency Wind-Driven Mixed Rossby–Gravity Waves in the Equatorial Indian Ocean". In: *Journal of Physical Oceanography* 53.6. Publisher: American Meteorological Society Section: Journal of Physical Oceanography, pp. 1535–1553. DOI: 10.1175/JPO-D-22-0222.1.

Nichols, S. M. and D. L. Bradley (2017). "In Situ Shape Estimation of Triangular Moored Hydrophone Arrays Using Ambient Signals". In: *IEEE Journal of Oceanic Engineering* 42.4, pp. 923–935. DOI: 10.1109/JOE.2016.2625378.

Nocedal, J. and S. Wright (2006). *Numerical Optimization, Second Edition*. Springer Series in Operations Research and Financial Engineering. Springer, pp. 1–664. DOI: 10.1007/978-0-387-40065-5.

Noh, Y. and H. Jin Kim (1999). "Simulations of temperature and turbulence structure of the oceanic boundary layer with the improved near-surface process". In: *Journal of Geophysical Research: Oceans* 104.C7, pp. 15621–15634. DOI: 10.1029/1999JC900068.

Nonaka, M., H. Nakamura, Y. Tanimoto, T. Kagimoto, and H. Sasaki (2006). "Decadal Variability in the Kuroshio Oyashio Extension Simulated in an Eddy-Resolving OGCM". In: *Journal of Climate* 19.10, p. 1970. DOI: 10.1175/JCLI3793.1.

Ogata, T., M. Nagura, and Y. Masumoto (2017). "Mean Subsurface Upwelling Induced by Intraseasonal Variability over the Equatorial Indian Ocean". In: *Journal of Physical Oceanography* 47.6. Publisher: American Meteorological Society Section: Journal of Physical Oceanography, pp. 1347–1365. DOI: 10.1175/JPO-D-16-0257.1.

Ogata, T., H. Sasaki, V. S. N. Murty, M. S. S. Sarma, and Y. Masumoto (2008). "Intraseasonal meridional current variability in the eastern equatorial Indian Ocean". In: *Journal of Geophysical Research: Oceans* 113 (C7). DOI: 10.1029/2007JC004331.

Okal, E. A. (2008). "The generation of T waves by earthquakes". In: *Advances in Geophysics* 49, pp. 1–65. DOI: 10.1016/S0065-2687(07)49001-X.

Palmer, M. D., D. J. McNeall, and N. J. Dunstone (2011). "Importance of the deep ocean for estimating decadal changes in Earth's radiation balance". In: *GRL* 38.13, p. L13707. DOI: 10.1029/2011GL047835.

Peng, S., J. Callies, W. Wu, and Z. Zhan (2024). "Seismic Ocean Thermometry of the Kuroshio Extension Region". In: *Journal of Geophysical Research: Oceans* 129.2, e2023JC020636. DOI: 10.1029/2023JC020636.

Pujiana, K. and M. J. McPhaden (2021). "Biweekly Mixed Rossby-Gravity Waves in the Equatorial Indian Ocean". In: *Journal of Geophysical Research: Oceans* 126.5, e2020JC016840. DOI: `10.1029/2020JC016840`.

Purkey, S. G. and G. C. Johnson (2010). "Warming of Global Abyssal and Deep Southern Ocean Waters between the 1990s and 2000s: Contributions to Global Heat and Sea Level Rise Budgets". In: *Journal of Climate* 23.23, pp. 6336–6351. DOI: `10.1175/2010JCLI3682.1`.

Qiu, B. and S. Chen (2005). "Variability of the Kuroshio Extension Jet, Recirculation Gyre, and Mesoscale Eddies on Decadal Time Scales". In: *Journal of Physical Oceanography* 35.11, p. 2090. DOI: `10.1175/JPO2807.1`.

Qiu, B. and S. Chen (2021). "Revisit of the Occurrence of the Kuroshio Large Meander South of Japan". In: *Journal of Physical Oceanography* 51.12, pp. 3679–3694. DOI: `10.1175/JPO-D-21-0167.1`.

Qiu, B., S. Chen, and E. Oka (2023). "Why Did the 2017 Kuroshio Large Meander Event Become the Longest in the Past 70 Years?" In: *GRL* 50.10, e2023GL103548. DOI: `10.1029/2023GL103548`.

Qiu, B., S. Chen, N. Schneider, E. Oka, and S. Sugimoto (2020). "On the Reset of the Wind-Forced Decadal Kuroshio Extension Variability in Late 2017". In: *Journal of Climate* 33.24, pp. 10813–10828. DOI: `10.1175/JCLI-D-20-0237.1`.

Reppin, J., F. A. Schott, J. Fischer, and D. Quadfasel (1999). "Equatorial currents and transports in the upper central Indian Ocean: Annual cycle and interannual variability". In: *Journal of Geophysical Research: Oceans* 104 (C7), pp. 15495–15514. DOI: `10.1029/1999JC900093`.

Riser, S. C. et al. (2016). "Fifteen years of ocean observations with the global Argo array". In: *Nature Clim. Change* 6, 145–153. DOI: `10.1038/NCLIMATE2872`.

Roemmich, D. and J. Gilson (2009). "The 2004-2008 mean and annual cycle of temperature, salinity, and steric height in the global ocean from the Argo Program". In: *Prog. Oceanogr.* 82, 81–100. DOI: `10.1016/j.pocean.2009.03.004`.

Roman-Stork, H. L., B. Subrahmanyam, and C. B. Trott (2020). "Monitoring Intraseasonal Oscillations in the Indian Ocean Using Satellite Observations". In: *Journal of Geophysical Research: Oceans* 125.2, e2019JC015891. DOI: `10.1029/2019JC015891`.

Rossby, T., C. N. Flagg, K. Donohue, S. Fontana, R. Curry, M. Andres, and J. Forsyth (2019). "Oleander is More than a Flower: Twenty-Five Years of Oceanography Aboard a Merchant Vessel". In: *Oceanography* 32.3, pp. 126–137. DOI: `10.5670/oceanog.2019.319`.

Saba, V. S. et al. (2016). "Enhanced warming of the Northwest Atlantic Ocean under climate change". In: *Journal of Geophysical Research (Oceans)* 121.1, pp. 118–132. DOI: `10.1002/2015JC011346`.

Sanz-Alonso, D., A. M. Stuart, and A. Taeb (2018). "Inverse Problems and Data Assimilation". In: *arXiv e-prints*, arXiv:1810.06191, arXiv:1810.06191. DOI: `10.48550/arXiv.1810.06191`.

Sasaki, H. et al. (2020). "A global eddying hindcast ocean simulation with OFES2". In: *Geoscientific Model Development* 13.7. Publisher: Copernicus GmbH, pp. 3319–3336. DOI: `10.5194/gmd-13-3319-2020`.

Sengupta, D. (2004). "A biweekly mode in the equatorial Indian Ocean". In: *Journal of Geophysical Research* 109 (C10), p. C10003. DOI: `10.1029/2004JC002329`.

Simons, R. A. and C. John (2022). *ERDDAP*. NOAA/NMFS/SWFSC/ERD.

Sprintall, J. et al. (2024). "COVID Impacts Cause Critical Gaps in the Indian Ocean Observing System". In: *Bulletin of the American Meteorological Society* 105.3, E725–E741. DOI: `10.1175/BAMS-D-22-0270.1`.

Straume, E. O., C. Gaina, S. Medvedev, K. Hochmuth, K. Gohl, J. M. Whittaker, R. Abdul Fattah, J. C. Doornenbal, and J. R. Hopper (2019). "GlobSed: Updated total sediment thickness in the world's oceans". In: *Geochemistry, Geophysics, Geosystems* 20.4, pp. 1756–1772.

Subrahmanyam, B., C. B. Trott, and V. S. N. Murty (2018). "Detection of Intraseasonal Oscillations in SMAP Salinity in the Bay of Bengal". In: *Geophysical Research Letters* 45.14, pp. 7057–7065. DOI: `10.1029/2018GL078662`.

Sugimoto, S., K. Hanawa, T. Watanabe, T. Suga, and S.-P. Xie (2017). "Enhanced warming of the subtropical mode water in the North Pacific and North Atlantic". In: *Nature Climate Change* 7.9, pp. 656–658. DOI: `10.1038/nclimate3371`.

Talley, L. D. et al. (2016). "Changes in Ocean Heat, Carbon Content, and Ventilation: A Review of the First Decade of GO-SHIP Global Repeat Hydrography". In: *Annual Review of Marine Science* 8, pp. 185–215. DOI: `10.1146/annurev-marine-052915-100829`.

The ATOC Consortium (1998). "Ocean Climate Change: Comparison of Acoustic Tomography, Satellite Altimetry, and Modeling". In: *Science* 281.5381, pp. 1327–1332. DOI: `10.1126/science.281.5381.1327`.

Trenberth, K. E., J. T. Fasullo, and M. A. Balmaseda (2014). "Earth's Energy Imbalance". In: *Journal of Climate* 27.9, pp. 3129–3144. DOI: `10.1175/JCLI-D-13-00294.1`.

Tsujino, H. et al. (2018). "JRA-55 based surface dataset for driving ocean–sea-ice models (JRA55-do)". In: *Ocean Modelling* 130, pp. 79–139. DOI: `10.1016/j.ocemod.2018.07.002`.

Uchida, N. and R. Bürgmann (2019). "Repeating Earthquakes". In: *Annual Review of Earth and Planetary Sciences* 47.1, pp. 305–332. DOI: `10.1146/annurev-earth-053018-060119`.

Von Schuckmann, K. et al. (2016). "An imperative to monitor Earth's energy imbalance". In: *Nature Climate Change* 6, pp. 138–144. DOI: `10.1038/nclimate2876`.

Wang, G., L. Cheng, J. Abraham, and C. Li (2018). "Consensuses and Discrepancies of Basin-Scale Ocean Heat Content Changes in Different Ocean Analyses". In: *Climate Dynamics* 50.7, pp. 2471–2487. DOI: `10.1007/s00382-017-3751-5`.

Wu, B., X. Lin, and L. Yu (2021). "Poleward Shift of the Kuroshio Extension Front and Its Impact on the North Pacific Subtropical Mode Water in the Recent Decades". In: *Journal of Physical Oceanography* 51.2, pp. 457–474. DOI: `10.1175/JPO-D-20-0088.1`.

Wu, L. et al. (2012). "Enhanced warming over the global subtropical western boundary currents". In: *Nature Climate Change* 2.3, pp. 161–166. DOI: `10.1038/nclimate1353`.

Wu, W., Z. Shen, S. Peng, Z. Zhan, and J. Callies (2023). "Seismic Ocean Thermometry Using CTBTO Hydrophones". In: *Journal of Geophysical Research (Solid Earth)* 128.9, e2023JB026687. DOI: `10.1029/2023JB026687`.

Wu, W., Z. Zhan, S. Peng, S. Ni, and J. Callies (2020). "Seismic ocean thermometry". In: *Science* 369.6510, pp. 1510–1515. DOI: `10.1126/science.abb9519`.

Wunsch, C. (1997). "The Vertical Partition of Oceanic Horizontal Kinetic Energy". In: *Journal of Physical Oceanography* 27.8. Publisher: American Meteorological Society Section: Journal of Physical Oceanography, pp. 1770–1794. DOI: `10.1175/1520-0485(1997)027<1770:TVPOOH>2.0.CO;2`.

Wunsch, C. (2006). *Discrete Inverse and State Estimation Problems: With Geophysical Fluid Applications*. Cambridge University Press. DOI: `10.1017/CBO9780511535949`.

Wunsch, C. (2016). "Global Ocean Integrals and Means, with Trend Implications". In: *Annual Review of Marine Science* 8.1, pp. 1–33. DOI: `10.1146/annurev-marine-122414-034040`.

Wunsch, C. and P. Heimbach (2013). "Dynamically and Kinematically Consistent Global Ocean Circulation and Ice State Estimates". In: *Ocean Circulation and Climate*. Ed. by G. Siedler, S. M. Griffies, J. Gould, and J. A. Church. Vol. 103. International Geophysics. Academic Press, pp. 553–579. DOI: `10.1016/B978-0-12-391851-2.00021-0`.

Wunsch, C., P. Heimbach, R. M. Ponte, I. Fukumori, and The ECCO-GODAE Consortium Members (2009). "The Global General Circulation of the Ocean Estimated by the ECCO-Consortium". In: *Oceanography* 22.2. DOI: `10.5670/oceanog.2009.41`.

Wunsch, C. and D. Stammer (1998). "SATELLITE ALTIMETRY, THE MARINE GEOID, AND THE OCEANIC GENERAL CIRCULATION". In: *Annual Review of Earth and Planetary Sciences* 26.1, pp. 219–253. DOI: `10.1146/annurev.earth.26.1.219`.

Yarger, D., S. Stoev, and T. Hsing (2022). "A Functional-Data Approach to the Argo Data". In: *The Annals of Applied Statistics* 16.1, pp. 216–246. DOI: `10.1214/21-AOAS1477`.

Yasuda, I., K. Okuda, and M. Hirai (1992). "Evolution of a Kuroshio warm-core ring—variability of the hydrographic structure". In: *Deep Sea Research Part A. Oceanographic Research Papers* 39, S131–S161. DOI: `10.1016/S0198-0149(11)80009-9`.

Zeng, L. et al. (2021). "A Decade of Eastern Tropical Indian Ocean Observation Network (TIOON)". In: *Bulletin of the American Meteorological Society* 102.10, E2034–E2052. DOI: `10.1175/BAMS-D-19-0234.1`.